Investigating the interior of West Antarctica with light, radar, and electrical conductance

Tyler Jeffrey Fudge

A dissertation

submitted in partial fulfillment of the

requirements for the degree of

Doctor of Philosophy

University of Washington

2013

Reading Committee:

Edwin Waddington, Chair

Eric Steig

Benjamin Smith

Program Authorized to Offer Degree:

Earth and Space Sciences

University of Washington

Abstract

Investigating the interior of West Antarctica with light, radar, and electrical conductance

by Tyler Jeffrey Fudge

Chair of Supervisory Committee:
Professor Edwin D. Waddington
Earth and Space Sciences

Ice sheets play an important role in both the modern climate and in past variations of Earth's history.

Our understanding of ice sheets has been limited by few observations until recent advances in

technology, notably air planes and satellites, which have allowed increasingly more detailed

investigations. Here I focus on using the internal structure of ice sheets to place modern observations in

context. This is done with a variety of tools. First, I investigated the ability of borehole camera

measurements to recover information about the physical properties of firn. I found that a measurement

with a single wavelength of light was not capable of differentiating between brightness variations due to

changes in grain size and changes in density. An additional measurement in the near infrared, which is

sensitive to grain size variations, was identified as a way to differentiate density variations from grain

size variations. I also use the internal structure of the ice sheet imaged using ice penetrating radar to

examine the past flow structure of a major outlet glacier of West Antarctica. The flow directions were

found to have not changed significantly in the past few hundred years and the analysis also revealed

that the satellite-derived velocities had uncertainties larger than reported.

The internal structure of an ice sheet can also be investigated by drilling an ice core. By obtaining

samples of ancient ice, many detailed measurements are possible to look at past variations in climate

and ice sheet behavior. I measured the electrical properties of the WAIS Divide ice core and was able to

identify an annual signal to a depth of 2800. I then developed the first annually resolved timescale from

the Southern Hemisphere that spanned into the last glacial period, 30 ka. The annual timescale allowed identification of accumulation-rate changes not resolvable in other Antarctic ice cores. The timescale and accumulation-rate history were combined with the water stable isotopes, sea-salt sodium, and climate modeling to show that the onset of deglacial warming in West Antarctica occurred before a trigger from the Northern Hemisphere with a likely cause increasing local insolation. The annual timescale was also used to assess the timescales from other coastal Antarctic ice cores. The timescales of these 3 cores were based on linear interpolation, which causes significant problems: large age uncertainty between tie points, large changes in the duration of climate events at the tie points, and a consistent bias to older ages. Two inverse techniques were developed to improve timescale interpolation.

Table of Contents

Chapter 1: *Introduction*

At my general exam in February of 2012, my advisor asked the question: when you have completed the proposed work, what will you be an expert in? Simple questions are often the most important to answer. The following three paragraphs are a direct answer to this question and are supported by the four scientific papers that comprise the majority of this dissertation.

I am an expert in ice-core timescales and becoming an expert in managing an ice core project. With Ken Taylor's guidance, I developed the first annually resolved timescale through the glacial-interglacial transition in the Southern Hemisphere. Using this timescale, I derived an empirical measure for the interpolation uncertainty of ice cores dated using tie points as well as developed a widely applicable inverse technique to generate glaciologically realistic timescales. This technique was applied to 3 coastal Antarctic ice cores to illustrate the importance of interpolation on the interpretation of the climate records. I have also used the technique for the deep timescale from WAIS Divide. While I consider myself an expert in ice core timescales, I do not consider myself "the" expert because a wide range of expertise is needed. One area that I am not an expert is firn densification, although my work with borehole optical stratigraphy did explore the physical properties of firn. I feel it is more productive to let someone else be an expert in that aspect and instead focus my efforts on ice-flow related constraints. I are currently developing methods that respect both firn and ice-flow constraints that will yield the most precise record of Northern and Southern phasing of abrupt climate change yet obtained.

I am also developing an expertise in managing an ice core project. I was introduced to ice coring at the WAIS Divide field site. I made measurements during core processing at the National Ice Core Lab in Denver, CO. I then used those electrical measurements to develop a timescale. This gave me the opportunity to collaborate with many people on the WAIS Divide project and lead the first community paper from the US Ice Core Community. My work with WAIS Divide also gave me the opportunity to participate in the site selection process for the intermediate-depth ice core at South Pole, the next major US ice coring project. I will work with Eric Steig and others as a post doc on this project to develop knowledge of the new intermediate-depth drill and learn how to run an ice-coring project. At the completion of the post doc, I will have experience in all aspects of ice coring – planning, choosing a site, drilling, handling, cutting, making measurements, analyzing, publishing, and organizing large numbers of independent-minding researchers.

Becoming an expert in something specific is a critical part of the PhD process, but so is developing the breadth to tackle a wide range of scientific problems. The investigations of the optical properties of firn in Chapter 2 and the analysis of radar-detected internal layers in Chapter 3 may not have made me an expert in either firn or radioglaciology, but they did give me an understanding of the important questions in these fields and how measurements of those features can be used in my work. I also spent considerable time during my PhD on topics not detailed in this thesis: developing ice-particle temperature histories for temperature-sensitive trace gases; making mass balance measurements on Blue Glacier; and advising the drill location for the Roosevelt Island ice core project. These topics have introduced me to a broad range of collaborators and promise to yield many future collaborative research projects.

Motivations and Goals

Ice sheets are far removed from most people's lives. Of the 6 billion people on Earth, less than 1 in 10,000 are likely to ever come any closer to an ice sheet than flying 40,000 feet overhead. So why do we study ice sheets? For two primary reasons: 1) they store unparalleled records of past climate variations that allow us to better understand our climate system, and 2) changes in the size of the ice sheets directly affect our coastlines by changing sea level. The work described in this dissertation is motivated by both of these questions. While the collection of papers presented here tackles a wide range of topics, all seek to advance our understanding of the physical processes of ice sheets so that we can predict how modern climate change will impact our lives and that of our children and grand children. This dissertation integrates many different measurement techniques, observations, and models to address questions on timescales from years to tens of thousands of years.

Four prominent themes run throughout this thesis. The first is the variety of methods used to investigate the internal structure of the ice sheet. Specific frequencies of electromagnetic radiation are used for different purposes. For investigating firn, I used visible light (~10^{15} Hz) and also discuss possible improvements in the method using near-infrared. For investigating the internal structure of the ice sheet at large spatial scales (kilometers and greater), radar (1-100 MHz) can image internal layers of the ice sheet which are isochrones (layers of the same age). To measure annual variations on the WAIS Divide ice core, I measured the electrical current at 50kHz (AC-ECM) and 0Hz (DC) with electrodes in contact with the ice. The frequencies used in these investigations are chosen based on the physical properties of ice and the impurities stored in the ice. Ice has a near zero absorption at the blue end of the visible spectrum which is why differences between density and grain size in firn cannot be distinguished with a visible light source alone – an additional measurement in the near-infrared, which is sensitive to grain size variations because the absorption is more than two orders of magnitude greater, would allow the cause of the brightness variation to be determined. Radar is an effective means of investigating the interior of the ice sheet because there is little absorption and the waves are able to reflect off of small electrical contrasts and be received at the surface allowing internal layers to be imaged. The AC and DC ECM methods primarily measure the acidity of the ice – the H^+ ions that can move through the ice lattice; however, the AC method is also able to measure charged ions, e.g. Ca^{2+}, which cannot move through the ice lattice, but are able to conduct AC electricity by rotating. The different techniques in this thesis all use basic properties of ice to guide the measurement strategy.

A second theme is annual cycles in the firn and ice. Identification of annual cycles allows accurate and precise dating of ice cores and ice sheets necessary for detailed investigations of past climate and ice sheet behavior. All chapters in the thesis make use of annual cycles at least indirectly. Annual layering causes brightness variations recorded by borehole camera logs in firn and influences the densification of firn. Annual layers were recognized with electrical conductivity measurements on the WAIS Divide ice core. The Thwaites work also made use of annual layers, though much more indirectly; the accumulation rate in the catchment was determined from airborne radar that imaged annual internal layers. The interpolation of Antarctic timescales uses the annual timescale for WAIS Divide to evaluate the different interpolation methods. Understanding and identifying the annual cycles is a critical aspect of work on ice sheets and allows dating precision that is rare in other paleoclimate records.

A third theme of this dissertation is assessing and characterizing uncertainty. This is a theme common to much scientific work because understanding the uncertainty of a measurement is equally, if not more, important than the value of the measurement itself. The Thwaites work addresses uncertainty in two ways. First, I determine the uncertainty of the flux balance measurements. But in the process of doing this, I recognized that the stated uncertainties of the satellite-derived velocities were too low and excluded important sources of uncertainty. A similar result was found in the Antarctic timescale

interpolation paper where the "interpolation" uncertainty, which is often excluded in ice core analyses, can be a major contributor to the total age uncertainty of the timescale. Uncertainty was also a major aspect of the development of the WAIS Divide annual timescale. The uncertainty of the timescale was assessed two ways: 1) by qualitatively rating the strength of the annual signal and defining an accumulating rate of uncertainty as some percentage of the total years identified; and 2) by comparing with other accurate timescales using climate features recognized in both timescales. The estimated uncertainty in method 1 was found to be much greater than the age differences with other timescales, suggesting the timescale is more accurate than implied by the estimated uncertainty. This emphasis on uncertainty is critical to robust records and also illustrates that uncertainties stated elsewhere should be verified because important sources of uncertainty are often excluded from analyses.

A fourth theme running throughout this dissertation is the importance of past variations in ice flow. The Thwaites work looks specifically at whether the ice flow directions have changed in recent decades. The WAIS Divide analyses discuss the effect of past ice flow in two ways. First, the past ice flow must be incorporated to determine past accumulation rates from measured annual layer thicknesses. The climate records, specifically stable isotopes of oxygen, also need to be interpreted with respect to ice flow because the effects of advection from a location upstream must be separated from climate changes through time. The interpolation paper also discusses past ice flow, but makes the point that interpolation methods are not sensitive to past ice flow, allowing accurate timescales even if the past ice-flow histories are not well known.

Background

Ice sheets are formed when more snow falls during a year than is melted away. In Antarctica, there little surface melt, except on the Peninsula, and the ice that accumulates in the center of the ice sheet flows out to ocean where it is removed by melting and iceberg calving. This leads to a pattern of ice flow where the velocities are slow in the interior and become more rapid closer to the coast. The ice-sheet/ocean interactions influence the ice flow from the interior of the ice sheet to the ocean and therefore affect global sea level. Recent observations have shown large changes in ice flow in parts of West Antarctica. Placing these recent accelerations in context is difficult because of the short period of observations. Fortunately, ice sheets also preserve exceptional records of past climate and ice-flow variability. Because each year's snow fall is preserved in the ice sheet, we can obtain records of both ice and air from the past. Evidence of past flow is also preserved in the internal structure of the ice sheets which can be imaged using radar. The ability of ice sheets to preserve information of past climate and ice-flow variations allows recent variations to be put in a historical context. This dissertation focuses of methods and observations of past variations to improve our understanding of future changes from human-caused climate change.

Firn

The top layer of an ice sheet is composed of snow that is slowly densifying to ice. This layer of the ice sheet is termed "firn" and is typically about 100 m deep. Understanding firn processes is important for a variety of reasons:
1) Calculations of an ice sheet's contribution to sea level rise often use surface elevations to calculate the mass change, which requires an estimate of the density profile of the firn
2) Accumulation rates are inferred by counting annual layers from polar firn cores and are used to calibrate atmospheric circulation models

3) The timescales for paleoclimate records require an estimate of the age difference between the air trapped in bubbles and the ice enclosing them, which is a function of the time it takes for the firn to transform to ice

4) The chemistry of the air trapped in the bubbles may also be affected by the structure of the firn

Modeling firn remains of significant challenge and no accurate models exist that calculate densification from first principles. The difficulty of obtaining detailed measurements of firn processes contributes to challenge and Chapter 2 addresses techniques to rapidly obtain the physical properties of firn.

West Antarctic Ice Sheet (WAIS) Divide
WAIS Divide refers to the ice-flow divide between the Ross Sea and Amundsen Sea sectors. Three of the primary objectives for drilling a deep core at WAIS Divide were:
1) Obtain climate records with the precision and dating accuracy to assess the phasing of abrupt climate change with Northern Hemisphere records
2) Obtain the most detailed carbon dioxide record for the past glacial period and the glacial-interglacial transition to understand climate forcing by greenhouse gases
3) Understand the stability of WAIS and the potential for rapid sea level rise

The ice core was drilled to 3405 m, about 50 m above the bed so that a basal water system would not be interested. The oldest ice in the core was younger than anticipated, about 70,000 years old because of a high basal melt rate. The high melt rate did not allow ice from the previous interglacial period to be recovered, but it reduced the amount of strain thinning the ice has experienced leaving thick layers of ice for detailed analyses. The scientific return from drilling the WAIS Divide ice core is just beginning and the next decade will see many ground-breaking results from this ice core.

Organization

This thesis is organized into 7 chapters, beginning with this introduction and ending with an outlook for future research opportunities. The middle five chapters are scientific papers. There is also an appendix that describes details of the electrical conductivity measurements made on the WAIS Divide ice core. These papers have contributions from 49 co-authors which is a tribute to the collaborative nature of both the University of Washington glaciology group and the WAIS Divide ice core community. A synopsis of each paper is presented on the first page of the chapter as well as a short description of my contribution to the work.

Chapter 2: *Light propagation in firn: application to borehole video*

Originally published in the Journal of Glaciology

The first paper is directed at understanding the optical properties of firn. It was published in the Journal of Glaciology with Ben Smith as a co-author, significant contributions from Ed Waddington, and a thorough and constructive review from Elizabeth Morris which has served as a template for my own reviews of papers.

We assess a tool, Borehole Optical Stratigraphy (BOS), which uses a light source and a video camera to record how the amount of reflected light varies with depth. BOS has been used to identify annual layers and to measure firn compaction in repeat profiles. We wanted to determine if it could also be used to measure the physical properties of firn – specifically density and grain size. Traditional methods of measuring grain size and density at cm-scale resolution are time consuming and require either detailed analysis in the field or transporting the core back to a lab. Unfortunately, BOS is not an effective instrument for determining the physical properties of firn. The amount of light that returns to the camera depends on both density and grain size and they cannot be distinguished by brightness alone. The returned brightness in the visible light is affected by the spreading distance, a function of both grain size and density, whereas the near infrared is much more strongly affected by the grain size. Therefore, a device that measures two wavelengths has the potential to distinguish between density and grain size variations. The paper does not include our efforts at actually building the device because it proved to be challenging. While there was some promise, the nickname of DOG (Density Or Grain size), was not just from the acronym.

I wrote the manuscript and performed the modeling. The Monte-Carlo model was developed by Ben and then modified by me. Ben identified POV-Ray has an effective program for modeling the multiple reflections off the borehole wall and I developed and performed the model runs used in the paper.

Instruments and Methods

Light propagation in firn: application to borehole video

T.J. FUDGE,[1] Benjamin E. SMITH[2]

[1]Department of Earth and Space Sciences, University of Washington, Box 351310, Seattle, Washington 98195-1310, USA
E-mail: tjfudge@u.washington.edu
[2]Applied Physics Laboratory, University of Washington, 1013 NE 40th Street, Box 355640, Seattle,
Washington 98105-6698, USA

ABSTRACT. Borehole optical stratigraphy (BOS) is a borehole video system and processing routine for investigating polar firn. BOS records brightness variations in the firn and is effective at identifying stratigraphic markers. BOS brightness logs have been used to count annual layers and measure vertical strain, even though a specific cause of the brightness variations has not been determined. Here we combine two models of light transport to examine potential errors with BOS and identify improvements which will allow the system to estimate optical grain size. We use a Monte Carlo radiative transfer model to estimate the influence of firn microstructure variations on borehole reflectance. We then use a ray-tracing algorithm to model the multiple reflections within the borehole that cause measured brightness variations. Multiple reflections cause the brightness measured at a point on the borehole wall to not necessarily be equal to the local wall reflectance. The ray tracing further shows that wall imperfections or variations in the camera position can produce brightness variations that are unrelated to changes in firn properties. Smooth walls and good stabilization of the camera help ensure that brightness variations result from variations in firn properties, and thus are a measure of firn stratigraphy, rather than artifacts.

1. INTRODUCTION

Firn processes are critical to a variety of glaciological problems. Calculations of an ice sheet's contribution to sea-level rise often use surface elevations to calculate the mass change, which requires an estimate of the density profile of the firn (e.g. Cuffey, 2008; Helsen and others, 2008; Pritchard and others, 2009). Accumulation rates are inferred by counting annual layers from polar firn cores (e.g. Kaspari and others, 2004) and are used to calibrate atmospheric circulation models (e.g. Van den Broeke and others, 2006). The timescales for paleoclimate records require an estimate of the age difference between the air trapped in bubbles and the ice enclosing it, which is a function of the time it takes for the firn to transform to ice (e.g. Schwander and others, 1997). The chemistry of the air trapped in the bubbles may also be affected by the structure of the firn (e.g. Dominé and Shepson, 2002). One factor limiting our understanding of firn processes is the difficulty in obtaining firn cores for detailed measurements. Borehole logging can help fill this information gap because it retains some of the detail of measurements made on cores but requires less labor as the core need not be recovered and transported.

Hawley and others (2003) used borehole video and a processing routine called borehole optical stratigraphy (BOS) to count annual layers and determine a depth–age scale that agreed well with optical and electrical techniques used on the recovered core. The wind-slab/depth-hoar couplet (Alley and others, 1997) is thought to cause the brightness variations, although the effect of variations in grain size or density is not well understood. Hawley and Morris (2006) measured density with a neutron density probe (Morris and Cooper, 2003) in the same borehole where BOS measurements were made. They found that brightness was strongly correlated with density at shallow depths (upper 15 m), but that the correlation decreased with depth and became negative below 30 m. They interpreted the variation in correlation to be caused by a change in the densification regime at 15 m depth, but did not give a quantitative assessment of the importance of grain-size variations for the brightness signal.

Much theoretical work has been done on the interaction of electromagnetic radiation and snow grains (e.g. Warren, 1982), but research has focused on near-surface snow measured at flat air–snow surfaces, rather than on denser firn measured at curved borehole walls. Radiative transfer in boreholes requires more complicated modeling because borehole walls are curved and because photons may reflect off the borehole wall multiple times before they are detected at the camera. Modeling light transport in firn is also complicated by a lack of measurements to compare with theory. In this paper, we investigate how variations in firn properties produce measurable brightness variations with a pair of simplified models. We also examine how imperfections in the borehole wall and variations in the camera position may produce changes in wall brightness unrelated to changes in intrinsic firn properties.

2. MODELING

The path that light takes between the source and camera of a borehole video system can include multiple reflections from the borehole wall, and each reflection from the borehole wall can include multiple reflections from individual snow grains within the firn. Although it is possible to model both the multiple reflections from the wall and the multiple reflections from individual snow grains in one model, it is computationally expensive; the model would have to track millions of photons each time the camera and light source

were moved relative to features in the borehole. Instead, we divide the modeling into two parts: (1) propagation of photons through the firn and (2) multiple reflections of light from the borehole walls. We use a Monte Carlo, radiative transfer model to investigate how photons travel through the firn and to find the wall reflectance as a function of grain size and density. We use a ray-tracing algorithm to model the multiple reflections off the borehole wall and to investigate the effects of layering, wall imperfections and camera position on the brightness signal.

The goal of our modeling is to gain insight into the cause of brightness variations in borehole video logs. We simplify the modeling to focus only on changes in grain (or bubble) size and density. We do not attempt an exact solution of the radiative transfer equations. Assessing the effect of variations in grain shape on the brightness signal is difficult because relatively few observations of firn microstructure (e.g. Freitag and others, 2004; Baker and others, 2007; Hörhold and others, 2009) have been made at the level of detail required, and none have been linked with measurements of optical properties. Our simplified treatment allows a qualitative analysis of the cause of BOS brightness variations and potential errors associated with BOS logs. A full treatment of light propagation in firn is beyond the scope of this work.

2.1. Radiative transfer model of light transport in firn

2.1.1. Description of firn

Snow and firn have complex structures of interlocking grains of a variety of shapes and sizes (e.g. LaChapelle, 1992). At low densities ($<\sim$550 kg m^{-3}), the firn can be considered a collection of snow grains in a matrix of air (e.g. Wiscombe and Warren, 1980; Warren and others, 2006), while at high densities ($>\sim$800 kg m^{-3}) the firn is more like a collection of air bubbles in a matrix of ice (e.g. Mullen and Warren, 1988). In between is a transition region, where the difference between grains and bubbles becomes indistinct. The density and specific surface area (SSA), the area of the ice/air interface per unit volume, are two useful parameters for describing the complex structure of firn (e.g. Freitag and others, 2004). For modeling the optical properties of firn, we follow the widely applied assumption that the scattering and absorption properties of firn can be accurately represented by a collection of spheres with the same SSA and density (e.g. Wiscombe and Warren, 1980; Dozier and others, 1981; Mullen and Warren, 1988; Grenfell and Warren, 1999). The density and SSA uniquely determine an effective grain size and effective bubble size. Note that while the density and SSA are matched, the number of spheres is unlikely to equal either the number of snow grains or bubbles.

Dust, ash, soot and chemical impurities (e.g. sea salt) are also present in firn (e.g. Bertler and others, 2005). The dust and ash particles absorb visible light much more readily than ice and will cause a decrease in returned brightness in the firn (Warren and Wiscombe, 1980; Bay and others, 2001). In typical polar firn, the effects of dust, ash and impurities are small and the optical properties are dominated by scattering of light from ice/air boundaries (e.g. Bramall and others, 2005). Large concentrations of soot or other contaminants (e.g. a dense ash layer from a volcanic eruption) could dominate the microstructure-based effects we discuss here, but as these features are rarely found in firn in most parts of Greenland and Antarctica, we do not consider their effect.

2.1.2. Firn reflectance

We investigate the variations in firn reflectance for different combinations of density and either grain or bubble size with a Monte Carlo radiative transfer model. This model is better suited to our purposes than the adding-doubling (e.g. Hansen, 1971) and multi-stream methods (e.g. Bohren, 1987) used in other studies of ice surface albedo, because it allows treatment of a curved boundary and a point-like light source. The model determines the wall reflectance as a function of grain size, density and borehole radius. This model was adapted from a simple Monte Carlo code designed for analysis of radiation propagation in human tissue (Prahl, 1988); the code will be available at: http://gcmd.nasa.gov/getdif.htm?waddington_0335330.

Our model tracks packets of photons that enter optically thick firn at a single location, simulating a collimated-beam light source. We assume no Fresnel reflection on the borehole wall. At each scattering event, a new direction for the packet is chosen from a Henyey–Greenstein (H-G) phase function (Henyey and Greenstein, 1941). The H-G phase function requires specification of the asymmetry parameter, g, the mean cosine of the phase angle of scattered photons. After several scattering events, the H-G phase function accurately approximates true phase functions with the same asymmetry parameter and allows high computational efficiency compared to calculations that use more detailed approximations of the phase function (e.g. Petty, 2006). A value of $g = 0$ yields isotropic scattering, while $g = 1$ yields pure forward scattering. Snow grains that are large compared to the wavelength of light are strongly forward-scattering, with g equal to $\sim$0.89 (Wiscombe and Warren, 1980); spherical air bubbles have g values between 0.85 and 0.86 (Mullen and Warren, 1988).

At the exit location, the contribution of each packet to the exit intensity is determined using an attenuation factor chosen depending on whether the modeled firn is most similar to a collection of ice grains in air or to a collection of air bubbles in ice:

$$dI(x, y, \theta, \omega, N) = \frac{I_0}{N_{photons}} \begin{cases} \omega^{N_{scat}} & \text{ice grains in air} \\ \exp\left(-k_{ice}L\frac{\rho_{firn}}{\rho_{ice}}\right) & \text{air bubbles in ice.} \end{cases}$$

(1)

Here x and y are Cartesian coordinates on the surface of the slab of firn, θ is the angle at which the light exits the surface relative to the vertical axis, z, I_0 is the initial intensity and $N_{photons}$ is the number of packets tracked. For ice grains in air, the absorption is determined by ω, the single-scatter albedo for ice grains, and the number of scattering events, N_{scat}. For air bubbles in ice, the single-scattering albedo of the air bubbles is treated as unity, and the factor

$$\exp(-k_{ice}L(\rho_{firn}/\rho_{ice}))$$

accounts for absorption as a photon travels through the ice. Here k_{ice} is the absorption coefficient for ice (Warren and Brandt, 2008), ρ_{firn} and ρ_{ice} are the densities of the firn and ice, and L is the distance the photon traveled. The total absorption is assumed to be proportional to the volumetric ice concentration (Mullen and Warren, 1988). This process is repeated for $\sim$10^7 photons.

The outgoing intensity is in units of energy steradian^{-1} L_{scat}^{-2}. The scattering length, L_{scat}, is the e-folding distance for extinction of a photon along a

particular direction by scattering, and is found by

$$\frac{1}{L_{scat}} = \sigma_{scat} = n(r)\pi r^2 Q_{scat}, \qquad (2)$$

where σ_{scat} is the scattering coefficient, $n(r)$ is the density of scatterers per unit volume, r is the mean radius of the scattering particle and Q_{scat} is the scattering efficiency. The scattering efficiency gives the total scattering cross section for the particle per unit cross-sectional area; it depends on the wavelength of the radiation and the size and material properties of the particle. It is usually ~ 2 because the path of a photon traveling near a snow grain or bubble can be deflected by diffraction.

The density of scatterers, $n(r)$, can be equated to mass density of the firn for grains in air,

$$\rho_{firn} = n(r_g)\frac{4}{3}\pi r_g^3 \rho_{ice}, \qquad (3)$$

where r_g is the radius of the ice grains. For bubbles in ice,

$$\rho_{firn} = \rho_{ice}\left(1 - n(r_b)\frac{4}{3}\pi r_b^3\right), \qquad (4)$$

where r_b is the radius of the bubbles. An equation for the scattering length as a function of grain size and density results from combining Equations (2) and (3) for grains in air:

$$L_{scat} = \frac{4}{3}\frac{\rho_{ice} r_g}{Q_{scat}\rho_{firn}}. \qquad (5)$$

Combining Equations (2) and (4) for bubbles in ice,

$$L_{scat} = \frac{4}{3}\frac{\rho_{ice} r_b}{Q_{scat}(\rho_{ice} - \rho_{firn})}. \qquad (6)$$

The model was designed to use units of the number of scattering lengths, so that the results from a single run can produce reflectances for different combinations of grain or bubble size and density. The only parameter of the firn that is specified in the Monte Carlo code is g. The output can be scaled to length units for any combination of grain or bubble size, density and scattering efficiency (appropriate values discussed below).

2.1.3. Applicability to wide density range

In our modeling results, we use parameters appropriate to scattering of light by large particles. The scattering efficiency is ~ 2 for both ice grains in air (e.g. Warren and others, 2006) and air bubbles in ice (Fu and Sun, 2001). The single-scatter albedo for ice grains was calculated using

$$(1 - \omega) \approx 0.85 k_{ice} r_g \qquad (7)$$

following Warren and others (2006). For air bubbles in ice, we assume there is no significant absorption during the scattering events ($\omega = 1$) and account for absorption with the ice-path length factor in Equation (1). At transition densities, neither approximation is clearly more accurate than the other. For the large ice grains considered here, combining Equations (1), (5) and (7) gives the average absorption per scattering event as approximately $1.28 k_{ice}\rho_{firn}/\rho_{ice}$. By contrast, Equation (1) for bubbles in ice gives the average absorption per scattering event as $\sim k_{ice}\rho_{firn}/\rho_{ice}$, or about 30% less. The difference arises primarily because during a scattering event from an ice grain in air, photons take a complicated path that reflects multiple times off the air–ice interface, increasing the path length in the ice grain. Over the course of a particle's path through the firn, the larger asymmetry parameter for ice grains also tends to lead to

greater path lengths than those calculated for bubbles, leading again to more absorption.

The grains-in-air approximation has been validated against field measurements (e.g. Hudson and others, 2006) for densities smaller than the close-packed density. Theoretical arguments suggest this formulation should give reasonably accurate results for close-packed grains (Wiscombe and Warren, 1980). The bubbles-in-ice approximation matches measured reflectances for $\rho_{firn} > 800\,kg\,m^{-3}$ (Mullen and Warren, 1988), but has not been tested at lower densities. We could transition smoothly between the two approximations by weighting each according to the density in the transition region. However, such an approach has two main problems: (1) we are aware of no measurements that indicate how the transition between the two approximations occurs, and (2) creating a smooth transition does not add insight into the processes causing variations in BOS brightness measurements. In the remainder of the paper, we show results from the grains-in-air approximation for all densities, and we present the results of the bubbles-in-ice approximation for $\rho_{firn} > 550\,kg\,m^{-3}$ for comparison. Hereafter, we discuss the variations in firn microstructure in terms of density and grain size rather than bubble size.

2.1.4. Tracking the return of photons to boreholes

The cylindrical geometry of the borehole reduces the effective albedo of the wall; as the borehole radius decreases, photons become less likely to re-encounter the borehole during their random walk through the firn. To derive reflectances for a curved borehole wall, the Monte Carlo process is modified to give reflectances as a function of a scaled borehole radius, Γ, equal to the borehole radius divided by L_{scat}. In this model, the borehole axis runs parallel to the z-axis. The photons enter the borehole wall (at the origin of the coordinate system), traveling in the $-x$ direction, and re-enter the borehole when $(x-\Gamma)^2 + y^2 < \Gamma^2$. The same photon may be tracked from a single starting position through several boreholes of different radius as long as the position, angle, distance traveled and number of scattering events is recorded the first time each photon re-enters a borehole of given diameter. The calculation is terminated when the photon re-enters the borehole with the smallest Γ, corresponding to the largest scattering length.

2.2. Ray-tracing model for multiple reflections in boreholes

2.2.1. Persistence of Vision ray-tracing algorithm

We use a ray-tracing algorithm to investigate how multiple reflections within the borehole produce variations in measured brightness. The ray-tracing package is the Persistence of Vision Raytracer (POV-Ray, http://www.povray.org). This has been used in a variety of research projects, including modeling radiant fluxes between building surfaces in urban environments (Lagouarde and others, 2010) and modeling light reflections in forest canopies (Casa and Jones, 2005). It tracks light rays from a source, through multiple reflections from objects with specified reflective properties, back to a camera. The light reaching the camera is calculated as a function of angle to produce an image. The modeled camera and light source were based on the GeoVision Jr™ borehole video camera used by Hawley and others (2003). The light source is a set of eight white light-emitting diodes (LEDs) forming a ring of 1.6 cm radius around the camera and angled out from the camera's optical axis by $\sim 20°$. We verified that
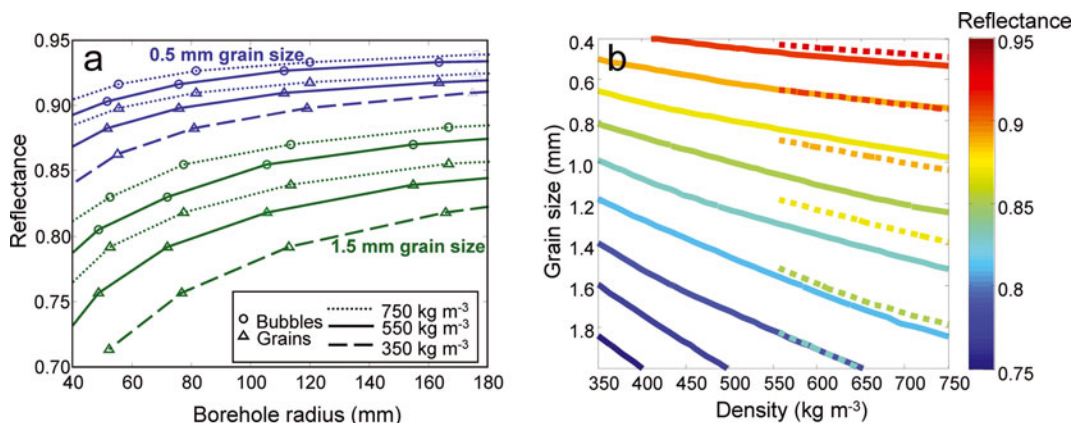
Fig. 1. The borehole wall reflectance depends on the grain size, density and borehole diameter. (a) Reflectance as a function of borehole radius for three different densities. For the two larger densities, the reflectance is calculated with the grains-in-air approximation (triangles) and the bubbles-in-ice approximation (circles). Grain sizes shown are 0.5 mm (blue) and 1.5 mm (green). (b) Reflectance for a 100 mm diameter borehole. The grains-in-air approximation is solid; bubbles-in-ice approximation is dashed. In both (a) and (b), the bubble size varies but matches the SSA and scattering length of the grain size and density combination.

the ray tracing reproduced the proper light emission, by simulating the illumination pattern of the model camera onto a diffuse, white surface and comparing the resulting images with the illumination pattern of the GeoVision Jr™ on a sheet of white paper. The borehole was modeled as a 10 cm diameter open cylinder, with the camera and light source at the center looking down the cylinder.

POV-Ray allows the user to specify both the fraction of light reflected and how that light is reflected from an object. Our choices for the fraction of light reflected from the borehole wall were guided by the radiative transfer results discussed below. We used a Lambertian reflectance model to describe the bidirectional reflectance function of the borehole wall. A Lambertian surface scatters light such that an observer perceives the same brightness from any viewing angle, and approximates our modeled surface well (see section 3.1.2). To model Lambertian reflectance, POV-Ray uses the Radiosity algorithm (Goral and others, 1984), in which surfaces are discretized into facets with Lambertian reflectance and the radiative transfer equation is solved to determine the radiant flux from each facet to each other facet.

3. RESULTS

3.1. Radiative transfer model of light propagation in firn

3.1.1. Borehole wall reflectance
Borehole wall reflectances are plotted as a function of grain size or bubble size for a series of borehole sizes in Figure 1a for three firn densities. The calculations were performed with an absorption coefficient of $0.12\,\mathrm{m^{-1}}$, appropriate for light of 600 nm wavelength (Warren and Brandt, 2008). Decreasing the borehole radius decreases the reflectance because fewer photons find their way back into the borehole. This effect is shown schematically for ice grains in Figure 2a. The borehole reflectance is significantly greater for the bubbles-in-ice than the grains-in-air approximation. As discussed above, this is caused both by the lesser absorption per scattering event and by the shorter path lengths that result from the lower asymmetry parameter for bubbles, $g = 0.85$, versus grains, $g = 0.89$. The pattern of reflectance variation with borehole size is similar for the two approximations, but the difference

in magnitude between the two is greater than that caused by a shift in density of $200\,\mathrm{kg\,m^{-3}}$. This suggests that the grain shape plays an important role in the brightness variations, which we have not modeled.

In Figure 1b, the reflectance is also seen to depend on the density and the grain size, both of which determine the
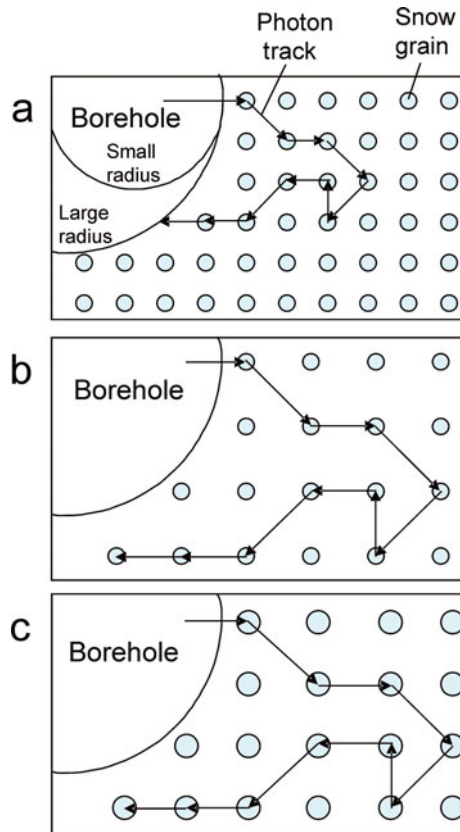
Fig. 2. Schematic showing the effects of varying the borehole radius (a), density (b) and grain size (c) on the likelihood of a photon returning to the borehole. Light-blue filled circles are snow grains. Arrows show photon paths. The photon scatters in the same direction at corresponding scattering events in each scenario. In (b) and (c) the photon does not return to the borehole because the scattering length has increased.
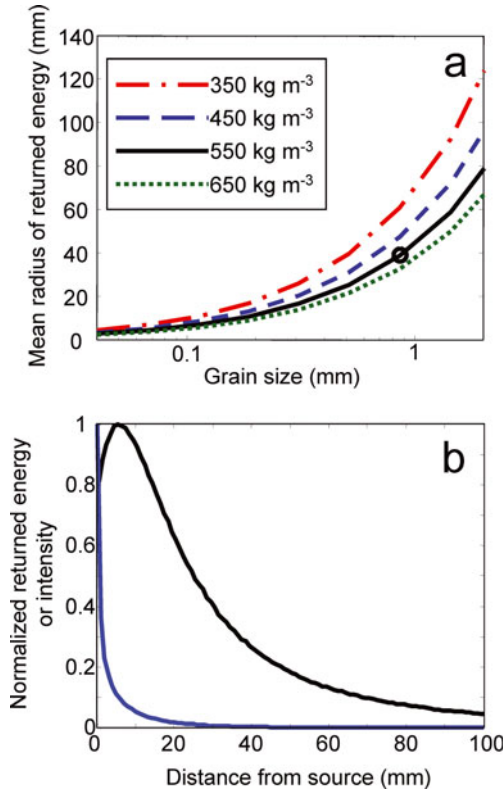
Fig. 3. (a) For a flat surface, the mean radius of returned energy can be calculated as the radius of the circle inside which half the energy exits the firn. It is defined in Equation (7). The circle marks the properties used in (b). (b) The fall-off of returned energy (black) and intensity (blue) with distance from the source for a flat wall and firn with a 1 mm scattering length. The returned energy is greater at 5 mm than at smaller radii because the percentage increase in area to which a photon returns increases faster than the fall-off in returned photons.

scattering length of the firn; fewer photons will return to the borehole for firn with a greater scattering length. Figure 2 shows how a photon that scatters in the same direction at each scattering event may not return to the borehole because of either an increase in grain size or a decrease in density. The decrease in reflectance from a decrease in density is due entirely to the change in scattering length, but an increase in grain size has a dual effect: a larger grain size both increases the scattering length and decreases the single-scatter albedo. Though variations in grain size change the borehole wall reflectance more than do variations in density, variations in either parameter can cause reflectance variations of the magnitude observed with BOS.

3.1.2. Distribution of light returned to the borehole
The radiative transfer model also determines the spatial displacement between the location at which photons enter the borehole wall in a single collimated beam and the location where they return. For high scattering lengths and/ or high single-scatter albedos, the displacement can complicate small-field-of-view measurements of firn albedo and blur reflected-light imagery within boreholes. A simple way to describe the extent of spreading is the mean radius of returned energy,

$$\langle R \rangle = \frac{\int R I(R)\, dA}{\int I(R)\, dA}, \tag{8}$$
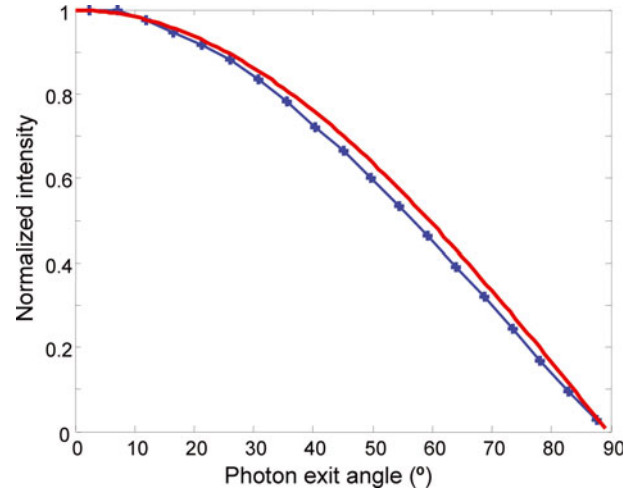
Fig. 4. Comparison of the intensity by exit angle for the radiative transfer model (blue with crosses) and the expected intensity for a Lambertian surface (red). A Lambertian surface has the same brightness from all viewing angles described by $I(\theta) = I(0)\cos(\theta)$, where I is intensity and θ is the exit angle.

where R is the distance between the point where the photon enters and exits the firn. The mean radius of returned energy depends upon the grain size, density and asymmetry parameter. Figure 3a shows the displacement for different densities and grain sizes and an asymmetry parameter of 0.89. The returned energy in each increment of radius [R, $R + dR$] and the intensity for each increment of radius are shown as a function of radius (Fig. 3b). The intensity falls off more quickly than the returned energy because the area increases with increasing radius. The returned energy is greater at 5 mm than at smaller radii because the fractional area that a photon can return to increases rapidly at small radii and has a greater effect than the fall-off in returned photons with radius.

The intensity of the photons leaving the borehole wall as a function of angle relative to the wall normal, θ, is shown in Figure 4. The normalized intensity curve matches the normalized curve for a Lambertian surface, for which $I(\theta) = I(0)\cos(\theta)$. The agreement is typically within a few percent, with a maximum difference of 15% at exit angles of ~75°. The close agreement shows that it is appropriate to represent the borehole wall in the ray-tracing model as a Lambertian surface.

3.2. Ray-tracing model results of multiple reflections in boreholes
3.2.1. Simulations
We conducted two types of simulations: variations in the borehole wall and variations in the camera position or orientation. For variations in the borehole wall, we added a feature to the borehole: either a dark band for a change in firn properties, or an imperfection, a ridge or gouge, as might be produced during drilling. For each feature type, we simulated a BOS log by generating a series of frames in which the camera position varied from 1 m above to 1 m below the feature.

We reduced each of these frames to a single brightness value following the technique of Hawley and others (2003), averaging the pixels in a narrow annulus around the borehole for each frame to give the brightness for
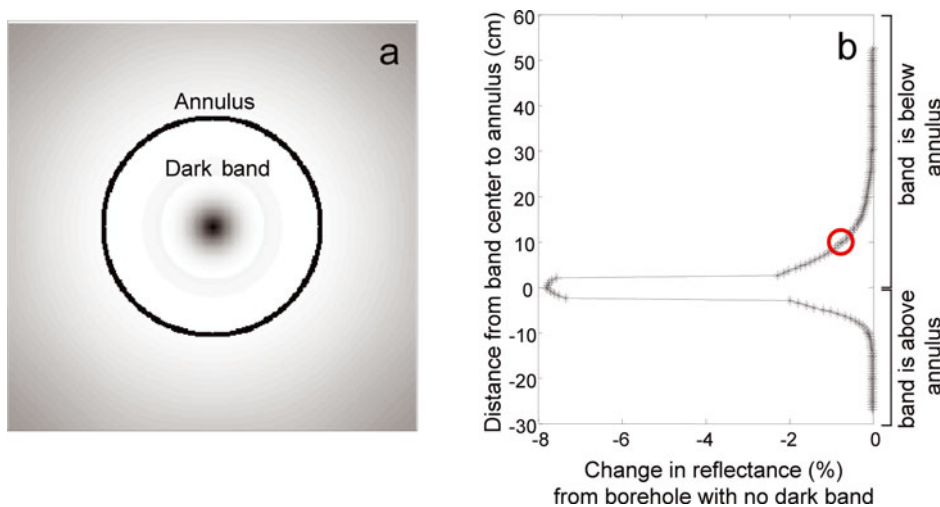
Fig. 5. (a) A borehole video frame created with the Persistence of Vision ray-tracing program. The annulus marks the pixels whose brightness values are averaged to create one brightness measurement. A band of lower reflectance is shown below the annulus. Wall reflectance is 80%, band reflectance is 5.26% less. (b) The percentage difference in brightness compared to a borehole with no dark band. Lowering the camera down a borehole is simulated by making a series of images (like (a)) as the feature is moved up the borehole relative to the camera. The red circle shows the brightness value from the image in (a).

~1 vertical cm of the borehole wall. The annulus is located 10 cm below the camera (Fig. 5). All brightness logs are presented as the percentage change from the brightness in a borehole with the same wall reflectance but no feature. The y-axis has been re-centered such that 0 indicates when the center of the annulus is located on the center of a feature (Fig. 5b). This permits the change in recorded brightness with distance from the feature to be easily seen.

We also produced series of images that simulate the variations in the camera orientation and position that will occur if the stabilizers for the camera lose contact with the borehole wall. The camera can either point away from the borehole axis or move from the center of the borehole. In the first series of images, we varied the pointing angle of the camera from 0 to 2.5° from the borehole axis. In the second series of images, we moved the camera from the center of the borehole to 3 cm off-center. In both series, the borehole wall had a consistent reflectance for the entire depth.

3.2.2. Accounting for the spreading of light in firn
In the ray-tracing algorithm, the light rays reflect off the borehole wall at the location of impact; they do not spread through the firn. Even though some features (e.g. the ridges and gouges) are likely covered in drill dust (small snow grains produced by drilling) that makes the scattering length lower than that of the surrounding firn, the spreading of light will still be significant (Fig. 3a). To approximate the spreading of light, we convolved the brightness logs for the dark-band and ridge-and-gouge simulations with a 5 cm wide kernel based on the pattern of intensity found with the radiative transfer model for firn with a 1 mm scattering length (Fig. 3b). We performed a second convolution with a 5 cm Gaussian kernel to approximate the filtering done in post-processing (e.g. Hawley and others, 2003).
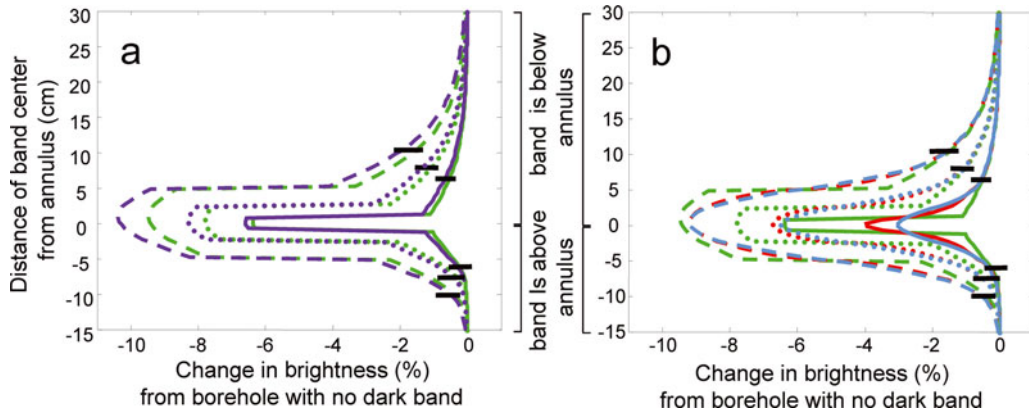
3.2.3. Band of lower reflectance
A layer in the firn with a different density and/or grain size than the local background norm was represented by a band of different reflectance. Dark bands of 5.26% less reflectance than the wall reflectance were modeled. The 5.26%

drop maintained consistency with the 95% background-reflectance case when the dark band was 90% reflective (5.26% is 0.05/0.95). The magnitude of the reflectance drop was based on reflectance changes of 1.5% and 3%, which we calculated from measurements of porosity and SSA for firn of depths 15 and 51 m from North Greenland (Freitag and others, 2004). The larger 5.26% drop helps reduce the numerical noise in the ray-tracing calculations. Simulations were run for three layer thicknesses, 2, 5 and 10 cm, and for two background borehole wall reflectances, 80% and 95%. The 95% simulations most closely resemble upper firn conditions of small grains and low scattering lengths. The 80% simulations are similar to deeper firn conditions, with larger grains and longer scattering lengths.

In all simulations, the drop in brightness measured at the band was greater than the 5.26% drop in reflectance of the band. Figure 6a shows the brightness variations for the three different bandwidths at 80% and 95% reflectance. The greater the borehole wall reflectance, the greater the fractional change in brightness at the center of the band. Futhermore, the decrease in brightness increased with the thickness of the band. The dark band also reduced the brightness beyond its edges: areas adjacent to the band, but above or below it, appeared darker, an effect that is more pronounced down-borehole from the dark band. The darkening occurs because the dark band absorbs some of the energy that is multiply reflected around the borehole. Having the dark band near the light source decreases the energy available to illuminate the borehole wall, and the brightness recorded at the annulus decreases, even if the annulus is not on the dark band.

The effects of light spreading through the firn and post-processing smoothing are shown in Figure 6b. The spreading of light decreases the magnitude of the brightness drop and smooths the measured signal at the band edge. The brightness change is reduced more for the thinner bands. The Gaussian smoothing has a similar effect, though the magnitude of the brightness drop at the center of the dark band is reduced more, particularly for the 2 cm thick bands.

11

Fig. 6. Percentage decrease in brightness due to borehole-wall multiple reflection effects. Dark bands have widths of 10 cm (dashed), 5 cm (dotted) and 2 cm (solid) and 5.26% lower reflectance than the borehole wall. Horizontal lines indicate one borehole radius (5 cm) away from the edge of a dark band. (a) 80% (green) and 95% (purple) wall reflectance. (b) 80% wall reflectance in green is same as in (a). To approximate the spreading of light in firn, we convolve the brightness log with a 5 cm kernel based on the intensity fall-off from the radiative transfer modeling (red). To simulate post-processing smoothing, we convolve the brightness log with a 5 cm Gaussian kernel (light blue).

3.2.4. Ridges and gouges

Imperfections in the borehole wall are often formed when the drill is stopped to extend the drill stem length or to recover a core section. To simulate these imperfections, we generated a set of images, where either a ridge or a gouge was added to the borehole circumference (Fig. 7a and b). In a cross section along the length of the borehole, the ridge is a semicircular projection of radius 1 mm into the borehole; the gouge is a depression. The brightness log for a borehole with a ridge at 80% wall reflectance is shown in Figure 7c. The ridge causes a ring of high brightness and a smaller shadowed area below. The brightness is affected more below the ridge than above it; no effect of the ridge is noticeable one borehole radius (5 cm) away from the ridge in either direction. Simulations with a wall reflectance of 95% were similar, though the magnitude of the brightness variation was less because of the large amount of light already reaching the camera.

The simulation of a BOS measurement with a 1 mm gouge is shown in Figure 7d. As in the ridge case, both a ring of high brightness and a smaller shadowed area are created, but in this case the shadowed area is higher in the borehole. The brightness increase when the annulus is centered on the gouge is similar to that of the ridge. The brightness immediately above and below the gouge is decreased, but no effect is noticeable at distances of one borehole radius away.

The effect of light spreading in the firn and of smoothing in post-processing on these logs is shown in Figure 7e and f. The brightness peak of the ridge or gouge is substantially muted, but the brightness increase is spread over a larger vertical distance. The sharp drop in brightness is no longer observed. The brightness record becomes more similar to the brightness variations caused by variations in firn properties (Fig. 6b). Convolving the brightness logs with the Gaussian kernel has a similar effect. The magnitude of the brightness signal is reduced but at the expense of making the signal from the wall imperfections visually more similar to a signal that might result from annual-scale layering.

3.2.5. Camera position and orientation

The effects of the camera pointing off the borehole axis and the camera pointing straight down but being offset from the

center of the borehole are shown in Figures 8 and 9. The brightness was calculated in two ways: (1) uncorrected – where, as above, the brightness was the average over an annulus of pixels 10 cm below the camera, centered on the middle of the image; and (2) corrected – where the annulus is re-centered on the darkest pixel in the image, which is a best guess of the bottom of the borehole. The brightness was also calculated for a half-annulus on each side of the borehole. The camera points (or is offset) toward the + side, and points (or is offset) away from the − side. For all images, the borehole wall reflectance was 80%.

As the camera tilt increases to 2.5°, the uncorrected half-annulus averages vary relative to the untilted image by up to 1.5% (Fig. 8). Correcting the averaging process by re-centering the annulus reduced this effect by about half. The uncorrected brightness variations of the two sides partly cancel each other for the full-annulus averages, but variations up to 0.5% can persist. Re-centering the annulus on the bottom of the borehole reduced the brightness variations to <0.2%. Simulations with boreholes of 20% and 98% wall reflectance showed similar improvements.

The effect of the camera being offset from the center of the borehole is shown in Figure 9. The variations in brightness are significantly larger than in the tilted-camera case, with a drop in brightness for an offset of 3 cm as large as 35% for the whole annulus, and as large as 55% for the + side. Re-centering the annulus does little to reduce the change in brightness because the center of the borehole does not move significantly due to the camera displacement. A different correction is required for these errors. The smooth shape of the brightness-change vs offset curve allows us to calculate a correction as a function of two values that can be determined for any annulus on any video frame: the mean brightness for the annulus, B_0, and the difference between the maximum and minimum brightness on the annulus, δB. The corrected brightness, $\hat{B}$, can be found by

$$\hat{B} = B_0(1 + f(\delta B, B_0)). \tag{9}$$

If the correction were perfect, the corrected brightness would equal the brightness of the same annulus when the camera is centered in the borehole. We used a
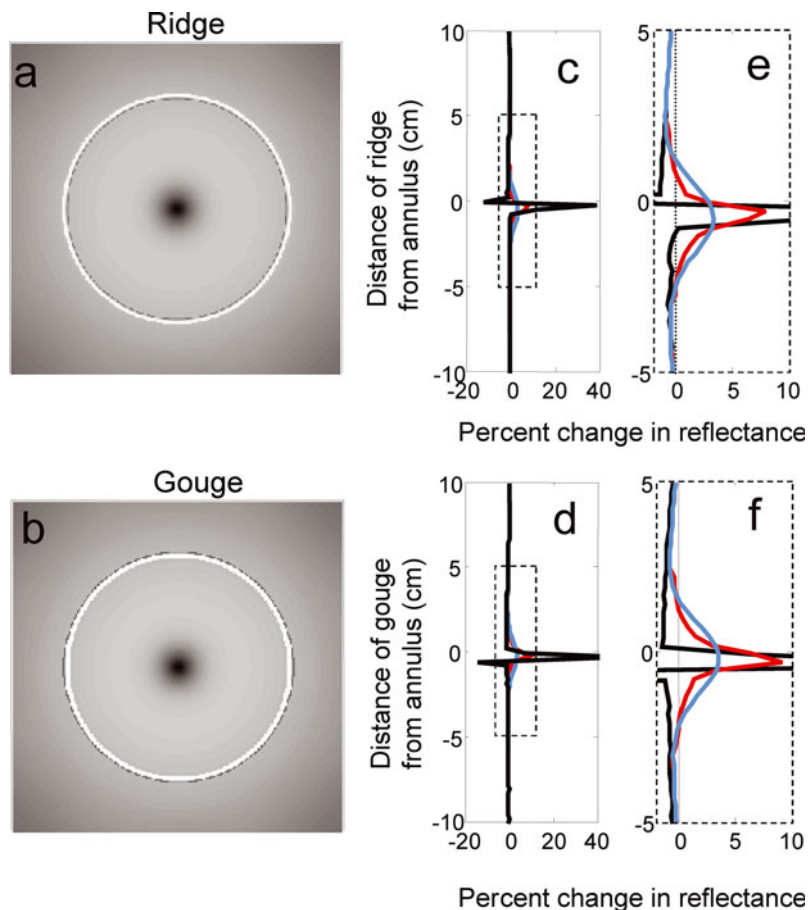
Fig. 7. Wall reflectance is 80%. (a) Ray-tracing image of borehole with a 1 mm ridge 10 cm below camera. Annulus is not shown. (b) Image of borehole with a 1 mm gouge 10 cm below camera. (c–f) Thick black curves show brightness change as camera is lowered past feature. The large (~40%) reflectance changes using ray tracing only are unrealistic because spreading of light in firn is not incorporated in the ray-tracing model. To approximate the spreading of light, we convolve the brightness log with a 5 cm kernel based on the intensity fall-off from the radiative transfer modeling (red). To simulate post-processing smoothing, we convolve the brightness log with a 5 cm Gaussian kernel (light blue). Dashed boxes in (c) and (d) show area enlarged in (e) and (f).

second-degree polynomial for *f*,

$$f(\delta B, B_0) = a\frac{\delta B}{B_0} + b\left(\frac{\delta B}{B_0}\right)^2, \qquad (10)$$

and found the values for *a* and *b* that minimized the misfit between $\hat{B}$ and the zero-offset brightness. A third-degree polynomial did not produce a noticeably better correction. For 80% wall reflectance and offsets less than 3 cm, the optimal coefficients were $a = 0.51$, $b = 0.3$. This corrected the brightness to within 2.5% of the centered camera case. These same coefficients produced similar improvements for a wall reflectance of 98%. For a wall reflectance of 20%, the corrected brightness still varied from the camera-centered brightness by ~6%.

4. DISCUSSION

BOS is an effective tool for identifying stratigraphic features in the firn. The features from one log can be used to count annual layers (Hawley and others, 2003), or repeat measurements (typically monthly or seasonally) in the same borehole can be used to measure vertical strain (R. Hawley and E. Waddington, unpublished information). The vertical strain measurements do not require a specific determination of the cause of the brightness features as long as the same

features can be identified in subsequent logs. However, the accuracy of the annual-layer count depends upon properly interpreting the brightness variations as seasonal changes in firn properties.

The two models described provide a framework for interpreting the brightness variations and understanding the limitations of borehole video. We focus our discussion on the accuracy of the annual-layer counts from BOS. We also include a short discussion of the limitations of borehole video on determining firn properties and suggest improvements for future devices.

4.1. Effect on annual-layer counts

Accurate annual-layer counting with BOS requires that the brightness variations observed are caused by seasonal changes in the firn properties (e.g. grain size and density) and are not a result of either wall imperfections or variations in camera position. The ray-tracing calculations when corrected for spreading of light in the firn (Fig. 7) show that the brightness variations from wall imperfections are similar to variations caused by intrinsic firn properties. The brightness variations caused by wall imperfections could be incorrectly interpreted as annual layers. At Siple Dome, Antarctica, Hawley and others (2003) counted more layers in the upper 70 m than the visual and electrical methods used on the core. Some of the extra layers measured
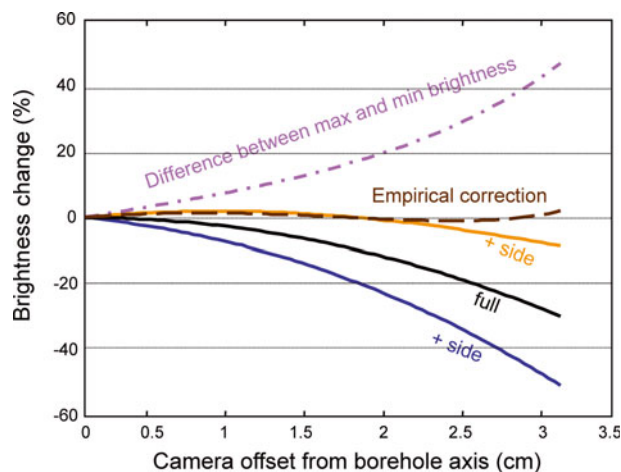
13
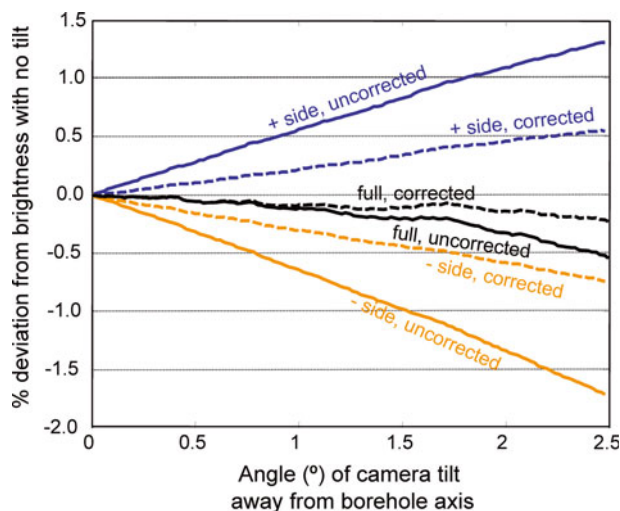
Fig. 8. Reflectance difference for the camera pointing off the borehole axis. Wall reflectance is 80%. Full annulus (black). The camera is pointing toward the + side (blue) and away from the – side (orange). Solid curves have no correction to the processing. Dashed curves improve the processing by re-centering on the darkest point in the image which is interpreted as the borehole center.

Fig. 9. Brightness change between a camera offset in the borehole and one centered. The camera is offset toward the + side (blue) and away from the – side (orange). The empirical correction (brown dashed) uses the full annulus brightness and the difference between the maximum and minimum brightness (purple dash dot) of the annulus to find the best estimate of what the brightness would be if the camera were centered in the borehole. See text and Equations (9) and (10) for description of empirical correction.

optically may have resulted from wall imperfections; the effects of wall imperfections are likely to be largest in the smaller-grained firn near the surface where volume scattering will be smallest. The best way to minimize the impact of wall imperfections on BOS logs is to use well-stabilized drills that leave the borehole with smooth walls. At Siple Dome, the borehole was drilled with a mechanically stabilized Eclipse drill, which produced relatively smooth walls, leading to a clean brightness log. When a hand-stabilized drill, a SideWinder, was used at the West Antarctic Ice Sheet Divide core site, the BOS brightness logs were difficult to interpret, likely due to scarring on the borehole wall (unpublished results).

Camera stabilization is also important for high-quality BOS logs. Variations in the camera angle and position can produce features that could be identified as part of the annual signal. These features can be identified and corrected if they come from angular misalignment between the camera and the borehole. However, it is difficult to identify and correct the log if the camera moves from the center of the borehole. A partial correction is possible based on the maximum, minimum and mean brightness for the annulus. However, this relationship is most accurate for a wall reflectance of 80%, and can over- or under-correct if the reflectance is significantly less.

Hawley and others (2003) calculated the brightness for each quarter of the borehole and found the same pattern of brightness variations for all quarters. They interpreted this to indicate they were seeing near-horizontal layers. This test is also important for checking the stabilization of the camera. Camera-position errors will result in non-synchronous brightness variations on different parts of the borehole wall. The absence of brightness variations between sections of the borehole supports the interpretation that the brightness variations are caused by firn properties.

The good agreement of the annual-layer counts from BOS, optical stratigraphy and electrical stratigraphy (Hawley and others, 2003) suggests that wall imperfections and

camera-pointing errors were not a major source of uncertainty at Siple Dome. Our modeling shows that BOS observations are most accurate when the borehole was drilled with a mechanically stabilized drill that limits wall imperfections and has a constant diameter that allows good stabilization of the camera.

4.2. Limitations of BOS and suggestions for future devices

An objective of borehole measurements is the quantitative determination of physical properties of the firn. While BOS is effective at identifying stratigraphic markers in the firn, it is ill-suited for recovering firn properties. Since BOS makes only one measurement of brightness integrated over the visible spectrum, it is not surprising that it cannot distinguish between grain-size and density variations as the cause of the brightness variations. There are additional limitations as well. The ray-tracing results demonstrate that BOS does not measure the local wall reflectance but rather some nonlinear average of the wall reflectances near the point of measurement. The complex viewing geometry that comes from a downward-looking camera is unnecessary; a device with a single light source (e.g. an LED) and a detector (e.g. a photodiode) can measure the local wall reflectance because the influence of multiple reflections will largely be eliminated.

Another limitation of the current BOS configuration for inferring firn properties is that it operates in the visible spectrum. The brightness variations are sensitive to changes in both grain size and density as shown with the radiative transfer modeling (Fig. 1). Even if the BOS measurements are paired with a log of density, such as from a neutron density probe (Morris and Cooper, 2003), it is unlikely that BOS can provide much information about the grain size or SSA of the firn. In the radiative transfer results, the difference in reflectance depending on whether the firn is treated as ice grains in air or air bubbles in ice also shows that the reflectance is sensitive to grain shape. Because ice

14

is weakly absorbing in the visible spectrum, photons can scatter many times without being absorbed and the energy returned to the borehole is sensitive to the degree of forward scattering. In the near infrared, ice is much more strongly absorbing, and the absorption predominantly determines the energy returned to the borehole. A device using a near-infrared wavelength may be more effective at quantitatively estimating the grain size or SSA of the firn (e.g. Matzl and Schneebeli, 2006).

5. CONCLUSION

Two models were used to examine how light emitted from a borehole video camera interacts with firn. A radiative transfer model, treating the firn as a collection of ice grains in air, showed that changes in borehole reflectance could be caused by variations in either density or grain size; photons are less likely to return when the scattering length (a function of both grain size and density) is large. Multiple combinations of grain size and density can produce the same wall reflectance, so BOS, making only a single measure of brightness in the visible spectrum, cannot distinguish between variations in firn density and grain size.

Ray-tracing modeling showed the importance of the multiple reflections from the borehole wall before photons return to the camera. Those multiple reflections cause the observed brightness to be a nonlinear average of the borehole-wall reflectance approximately one borehole diameter above and below the point of measurement. Imperfections on the borehole wall and non-centered camera positions can produce brightness variations that are unrelated to changes in firn properties. Smooth borehole walls and a well-stabilized camera improve the BOS brightness logs, yielding accurate annual-layer counts.

ACKNOWLEDGEMENTS

REFERENCES

Alley, R.B. *and 11 others*. 1997. Visual-stratigraphic dating of the GISP2 ice core: basis, reproducibility, and application. *J. Geophys. Res.,* **102**(C12), 26,367–26,382.

Baker, I., R. Obbard, D. Iliescu and D. Meese. 2007. Microstructural characterization of firn. *Hydrol. Process.,* **21**(12), 1624–1629.

Bay, R., P. Price, G. Clow and A. Gow. 2001. Climate logging with a new rapid optical technique at Siple Dome. *Geophys. Res. Lett.,* **28**(24), 4635–4638.

Bertler, N.A.N. *and 53 others*. 2005. Snow chemistry across Antarctica. *Ann. Glaciol.,* **41**, 167–179.

Bohren, C.F. 1987. Multiple scattering of light and some of its observable consequences. *Am. J. Phys.,* **55**(6), 524–533.

Bramall, N.E., R.C. Bay, K. Woschnagg, R.A. Rohde and P.B. Price. 2005. A deep high-resolution optical log of dust, ash, and stratigraphy in South Pole glacial ice. *Geophys. Res. Lett.,* **32**(21), L21815. (10.1029/2005GL024236.)

Casa, R. and H.G. Jones. 2005. LAI retrieval from multiangular image classification and inversion of a ray tracing model. *Remote Sens. Environ.,* **98**(4), 414–428.

Cuffey, K.M. 2008. Climate change: a matter of firn. *Science,* **320**(5883), 1596–1597.

Dominé, F. and P.B. Shepson. 2002. Air–snow interactions and atmospheric chemistry. *Science,* **297**(5586), 1506–1510.

Dozier, J., S.R. Schneider and D.F. McGinnis, Jr. 1981. Effect of grain size and snowpack water equivalence on visible and near-infrared satellite observations of snow. *Water Resour. Res.,* **17**(4), 1213–1221.

Freitag, J., F. Wilhelms and S. Kipfstuhl. 2004. Microstructure-dependent densification of polar firn derived from X-ray microtomography. *J. Glaciol.,* **50**(169), 243–250.

Fu, Q. and W. Sun. 2001. Mie theory for light scattering by a spherical particle in an absorbing medium. *Appl. Opt.,* **40**(9), 1354–1361.

Goral, C.M., K.E. Torrance, D.P. Greenberg and B. Battaile. 1984. Modeling the interaction of light between diffuse surfaces. *Comput. Graph.,* **18**(3), 213–222.

Grenfell, T.C. and S.G. Warren. 1999. Representation of a nonspherical ice particle by a collection of independent spheres for scattering and absorption of radiation. *J. Geophys. Res.,* **104**(D24), 31,697–31,709.

Hansen, J.E. 1971. Multiple scattering of polarized light in planetary atmospheres. Part I. The doubling method. *J. Atmos. Sci.,* **28**(1), 120–125.

Hawley, R.L. and E.M. Morris. 2006. Borehole optical stratigraphy and neutron-scattering density measurements at Summit, Greenland. *J. Glaciol.,* **52**(179), 491–496.

Hawley, R.L., E.D. Waddington, R.A. Alley and K.C. Taylor. 2003. Annual layers in polar firn detected by borehole optical stratigraphy. *Geophys. Res. Lett.,* **30**(15), 1788. (10.1029/2003GL017675.)

Hawley, R.L., E.M. Morris and J.R. McConnell. 2008. Rapid techniques for determining annual accumulation applied at Summit, Greenland. *J. Glaciol.,* **54**(188), 839–845. (10.3189/002214308787779951.)

Helsen, M.M. *and 7 others*. 2008. Elevation changes in Antarctica mainly determined by accumulation variability. *Science,* **320**(5883), 1626–1629.

Henyey, L.C. and J.L. Greenstein. 1941. Diffuse radiation in the galaxy. *J. Astrophys.,* **93**, 70–83.

Hörhold, M.W., M.R. Albert and J. Freitag. 2009. The impact of accumulation rate on anisotropy and air permeability of polar firn at a high-accumulation site. *J. Glaciol.,* **55**(192), 625–630.

Hudson, S.R., S.G. Warren, R.E. Brandt, T.C. Grenfell and D. Six. 2006. Spectral bidirectional reflectance of Antarctic snow: measurements and parameterization. *J. Geophys. Res.,* **111**(D18), D18106. (10.1029/2006JD007290.)

Kaspari, S. *and 6 others*. 2004. Climate variability in West Antarctica derived from annual accumulation-rate records from ITASE firn/ice cores. *Ann. Glaciol.,* **39**, 585–594.

LaChapelle, E.R. 1992. *Field guide to snow crystals.* Cambridge, International Glaciological Society.

Lagouarde, J.-P. *and 6 others*. 2010. Modelling daytime thermal infrared directional anisotropy over Toulouse city centre. *Remote Sens. Environ.,* **114**(1), 87–105.

Matzl, M. and M. Schneebeli. 2006. Measuring specific surface area of snow by near-infrared photography. *J. Glaciol.,* **52**(179), 558–564.

Morris, E.M. and J.D. Cooper. 2003. Density measurements in ice boreholes using neutron scattering. *J. Glaciol.,* **49**(167), 599–604.

Mullen, P.E. and S.G. Warren. 1988. Theory of the optical properties of lake ice. *J. Geophys. Res.,* **93**(D7), 8403–8414.

Petty, G.W. 2006. *A first course in atmospheric physics. Second edition.* Madison, WI, Sundog Publishing.

Prahl, S.A. 1988. Light transport in tissue. (PhD thesis, University of Texas, Austin.)

Pritchard, H.D., R.J. Arthern, D.G. Vaughan and L.A. Edwards. 2009. Extensive dynamic thinning on the margins of the Greenland and Antarctic ice sheets. *Nature,* **461**(7266), 971–975.

Schwander, J., T. Sowers, J.M. Barnola, T. Blunier, A. Fuchs and B. Malaizé. 1997. Age scale of the air in the Summit ice: implication for glacial–interglacial temperature change. *J. Geophys. Res.,* **102**(D16), 19,483–19,493.

Van den Broeke, M., W.J. van de Berg and E. van Meijgaard. 2006. Snowfall in coastal West Antarctica much greater than previously assumed. *Geophys. Res. Lett.,* **33**(2), L02505. (10.1029/2005GL025239.)

Warren, S.G. 1982. Optical properties of snow. *Rev. Geophys.,* **20**(1), 67–89.

Warren, S.G. and R.E. Brandt. 2008. Optical constants of ice from the ultraviolet to the microwave: a revised compilation. *J. Geophys. Res.,* **113**(D14), D14220. (10.1029/2007JD009744.)

Warren and W.J. Wiscombe. 1980. A model for the spectral albedo of snow. II. Snow containing atmospheric aerosols. *J. Atmos. Sci.,* **37**(12), 2734–2745.

Warren, S.G., R.E. Brandt and T.C. Grenfell. 2006. Visible and near-ultraviolet absorption spectrum of ice from transmission of solar radiation into snow. *Appl. Opt.,* **45**(21), 5320–5334.

Wiscombe, W.J. and S.G. Warren. 1980. A model for the spectral albedo of snow. I. Pure snow. *J. Atmos. Sci.,* **37**(12), 2712–2733.

Chapter 3: *Identifying flow lines and limitations of flux analyses in the interior of Thwaites Glacier*

The objective is to place modern outlet glacier variations in a historical context. The largest source of ice loss in Antarctica is in the Amundsen Sea region, particularly Thwaites and Pine Island glaciers. These glaciers have doubled their rate of ice loss in recent decades. Unfortunately, observations of ice flow in this region extend back only to the late 1970s with the first satellite observations. This makes it difficult to put the modern changes in context. We use internal layers imaged by radar to assess the past flow directions of Thwaites Glacier. These are found to agree closely with the modern flow. This not surprising for most of Thwaites Glacier because of deep bedrock troughs steering the flow but is also true from the Eastern Margin which is not strongly controlled by topography. The comparison of past and modern flow directions also revealed limitations of the satellite-derived velocity maps. Interferometric synthetic aperture radar (InSAR) methods did not resolve the ice-flow directions accurately. In addition, the differences between the InSAR velocities and very accurate GPS velocities often exceeded the stated uncertainty of the InSAR velocities. This illustrated that important sources of uncertainty in the InSAR methodology are being excluded from the stated uncertainties. We also used the radar-detected flow lines to define flowbands and performed a flux balance analysis in the middle tributary of Thwaites Glacier. We found a thinning rate of 0.49 m a^{-1}, but the uncertainty was 0.34 m a^{-1}. The main source of uncertainty was from the velocity estimate, which itself was underestimated. Therefore, flux balance analysis cannot resolve thickness change to a similar level of precision as altimetry measurements without a spatial array of GPS velocity measurements (or other measurements of similar precision).

I wrote the manuscript, defined the flow lines, and performed the flux analyses. The radar data was collected and the radar layers were tracked by colleagues at the Unviersity of Texas. InSAR and GPS velocities were also provided by collaborators.

1 Identifying flow lines and limitations of flux analyses in the
2 interior of Thwaites Glacier
3

4 T.J. Fudge[1], H. Conway[1], G. Catania[2], D. D. Blankenship[2], K. Christianson[3],
5 I. Joughin[4], B. Smith[4], S. D. Kempf[2], D. A. Young[2] & S. Anandakrishnan[5]
6 [1] Department of Earth and Space Sciences, Univ. of Washington
7 [2] Institute of Geophysics, University of Texas at Austin
8 [3] St. Olaf College
9 [4] Applied Physics Lab, Univ. of Washington
10 [5] Department of Geosciences, Penn State University
11
12

13 **ABSTRACT**
14 Patterns in radar-detected internal layers in glaciers and ice streams can be tracked
15 hundreds of kilometers downstream. We use distinctive patterns to delineate flow bands
16 of Thwaites Glacier in the Amundsen Sea sector of West Antarctica. Flow bands contain
17 information for the past century to millennium – the approximate time for ice to flow
18 through the study region. GPS-detected flow directions (acquired in 2007-08) agree
19 within uncertainty (~2°) with the radar -detected flow lines, indicating that the flow
20 direction has not changed significantly in recent centuries. In contrast, InSAR-detected
21 directions (from 1996) differ from the radar- and GPS-detected flow lines in all but the
22 middle tributary, indicating caution is needed when using InSAR velocities to define flow
23 directions. There is agreement between all three data sets in the middle tributary. We use
24 two radar-detected flow lines to define a 95-km long flow band and perform a flux
25 balance analysis using InSAR-derived velocities, radar-detected ice thickness, and
26 estimates of the accumulation rate. Inferred thinning of 0.49 ± 0.34 m yr^{-1} is consistent
27 with satellite altimetry measurements, but has higher uncertainty due mainly to the
28 velocity uncertainty. The uncertainty is underestimated because InSAR velocities often
29 differ from GPS velocities by more than the stated uncertainties.
30
31

32 INTRODUCTION
33 Thwaites Glacier in the Amundsen Sea Sector of West Antarctica has area of ~182,000
34 km^2, and much of it is grounded well below sea level with an inward sloping bed (Holt et
35 al. 2006). The catchment consists of tributaries that merge into the main trunk (Figure 1).
36 The glacier is currently losing mass at a rate of about 20 Gt/yr (Rignot et al. 2008);
37 thinning is 4 ± 0.07 m yr^{-1} in fast-moving regions near the grounding line, decreasing to
38 0.15 ± 0.07 m yr^{-1} in slower-moving (<100 m yr^{-1}) farther inland (Pritchard et al. 2012).
39 Recent changes over the past three decades include acceleration (Rignot et al., 2002),
40 increased thinning (Pritchard et al. 2009; Shepherd et al. 2012), loss of ice-shelf
41 buttressing (MacGregor et al. 2012) and increased ocean warming (Pritchard et al., 2012).
42 Accumulation in the catchment has changed little over past decades (Medley et al., 2013).
43
44 Over the past two decades, Thwaites Glacier has not accelerated as dramatically as Pine
45 Island Glacier, but has increased its rate of mass loss due to widening of the fast-flow

46   region, particularly on the eastern margin (Rignot, 2008). The Eastern margin is not well
47   constrained by topography or basal properties and may be susceptible to migration
48   (MacGregor et al., in press). Inferring changes in flow pattern are difficult because
49   observations in the interior of Thwaites only span a few decades; other indicators used for
50   inferring past flow directions, such as flow stripes (Fahnestock et al., 2000) or crevassing
51   at shear margins (Shabtaie et al., 1988) are not visible on Thwaites Glacier. Radar-
52   detected internal layers can be used to extract information about past ice flow over
53   century time scales; here we adapt methods developed by Ng and Conway (2004). The
54   radar-detected layers in fast-flowing ice often show trough-and-crest sequences that are
55   inherited from flow disturbances farther upstream. Although the origin of the layer
56   patterns may not be known, the patterns can be used to define the geometry of past flow
57   bands by tracking sequences between radar profiles perpendicular to the ice flow.
58
59   Quantifying the amount of thinning in the interior of Thwaites Glacier helps constrain the
60   rate that perturbations at the grounding line propagate inland (Payne et al., 2004; Joughin
61   et al., 2010a). For the fast-flowing region approximately 100 to 200 km inland of the
62   grounding line, satellite radar altimetry indicates thinning of ~0.10 m a^{-1} for 1992-2003
63   (e.g. Zwally et al., 2005; Helsen et al., 2008). Satellite laser altimetry suggests slightly
64   greater thinning of ~0.15 m a^{-1} (Pritchard et al., 2009) for 2003-2009. Altimetry
65   measurements are sensitive to inter-annual variations in accumulation rate and changes in
66   firn compaction. Flux analysis of flow bands is a potential complimentary method for
67   determining inland thinning rates because it is not sensitive to inter-annual accumulation
68   variability. Shabatie et al. (1988) used flux analyses to assess the mass balance of Mercer,
69   Whillans, and Kamb ice streams on the Siple Coast. They found a similar spatial pattern
70   of thinning and thickening as newer methods using satellite observations (Joughin et al.,
71   2002; Pritchard et al., 2009)
72
73
74   **DATA SOURCES and METHODS**
75   **Radar-detected ice thickness and internal layers**
76   Airborne geophysical surveys of the Amundsen Sea Embayment by the University of
77   Texas Institute of Geophysics (UTIG) and the British Antarctic Survey provide
78   measurements of ice thickness (Holt et al., 2006; Vaughan et al., 2006; Blankensip et al.,
79   2011) and internal layering. We use radar data collected by UTIG with a 60MHz, phase
80   coherent (HICARS) system (Peters et al., 2005). Ice thickness was mapped along radar
81   profiles that were collected on 15.6 km grids over Thwaites Glacier (Figure 1). Radar-
82   detected internal layers were picked and mapped using a seismic package (Geoframe)
83   with strong cross over control. The conversion of radar travels times to depth assumed a
84   constant wave velocity of 168.374 μs m^{-1} and did not incorporate a firn layer (Holt et al.,
85   2006).
86
87   **Radar-detected flow lines**
88   We mapped past flow lines through the study region by tracking positions of
89   recognizable features (crest and trough sequences) between successive pairs of radar
90   cross profiles (Figure 2). Positions of recognizable features were picked independently;
91   that is, when picking features between cross-profiles L2 and L3, the positions of picks

92   between cross profiles L1 and L2 were not considered. A total of 191 flow lines were
93   tracked (Figure 3; Conway et al., 2010); most were located in the eastern and middle
94   tributaries. Fewer flow lines could be tracked in the western tributaries because the radar
95   profiles often crossed the flow direction at angles >30°. Four flow lines in the middle
96   tributary could be tracked 110 km through eight cross-profiles.
97
98   The uncertainty in the flow lines was estimated from the differences between picks of a
99   feature at each radar line. Features were on average identified within 140 m with a
100   maximum difference of 380 m. This results in a ~3° uncertainty in the direction of a flow
101   line. The radar-detected layers provide information on time scales related to the advection
102   of ice between upstream and downstream cross profiles (Ng and Conway, 2004). The
103   velocities range from 75 to 400 m yr^{-1} in the study area so the time for flow through the
104   study area ranges from ~50 years for a feature identified in one pair of radar profiles
105   (~15.6 km) to ~600 years for features tracked through 8 radar profiles (~110 km).
106

Satellite-derived velocity field

107
108   We use a map of 1996 surface velocities derived using interferometric synthetic aperture
109   radar (InSAR) and speckle-tracking methods (Joughin et al., 2009). In areas of crossing
110   satellite orbits where the phase could be successfully unwrapped, formal uncertainty in
111   the horizontal velocity components is 3-5 m yr^{-1}. In addition to the formal uncertainties,
112   an additional ~3% uncertainty is introduced in the process of removing vertical
113   displacements (Joughin et al., 2009). A third uncertainty component comes from
114   systematic errors in the SAR baseline estimate used to convert image displacements and
115   phase differences into velocity values. While every effort has been made to minimize
116   these errors, for velocity estimates derived from image pairs with short temporal
117   intervals, these errors can be on the order of 50 m/yr, and are correlated over several tens
118   to hundreds of kilometers (Joughin et al., 2010b). The uncertainties of the InSAR
119   velocities presented in the Results section are the sum of the formal uncertainty and 3%
120   uncertainty from removing vertical displacements.
121
122   An InSAR velocity map is also available from Rignot et al. (2011). This velocity map
123   uses the same 1996 data as Joughin et al. (2009) but also incorporates data from 2007 and
124   2008 that covers portions of Thwaites Glacier. We primarily use the map of Joughin et al.
125   (2009) because it was developed for detailed investigations of Thwaites Glacier. We
126   discuss differences between the Rignot et al. (2011) and the Joughin et al. (2009)
127   velocities in a following section.
128

GPS Measurements

129
130   Dual –frequency GPS units (Trimble 5700, R7, NetRS receivers with Trimble Zephyr
131   geodetic antnnas) were installed for approximately 4-week durations during the Antarctic
132   summers of 2007-08 and 2008-09 along the 2 main trunks of Thwaites Glacier and on the
133   surrounding slow-moving, flanking ice. GPS antennas were mounted on rigid metal poles
134   that extended ~1-2 m across the ice surface. Our processing strategy generally follows
135   that outlined by King (2004) for glaciological applications. GPS stations on streaming ice
136   were processed kinematically relative to a local base station using differential carrier
137   phase positioning, with epoch-by-epoch zenith tropospheric delay estimation as

138   implemented in the Track software (Chen, 1998) with very loose constraints on rover site
139   motion. Daily solutions for the local base station on slow-moving ice near Mt. Takehe
140   were calculated using differential carrier phase positioning as implemented in
141   GAMIT/GLOBK. Antenna heights were updated daily assuming a linear trend between
142   measured antenna heights at the beginning and end of the field season. Horizontal
143   velocities were extracted from linear fits for the entire field seasons using iteratively
144   reweighted least squares with bisquare weighting after data were transformed into a polar
145   stereographic projection (central meridian is 0° and latitude of true scale is -71°S).
146   Although formal uncertainties (defined as two standard deviations from the best fit) were
147   very small (~0.001 m/a), we conservatively estimate horizontal velocity uncertainties at
148   ~0.2 m a^{-1} based on value of residuals from the best fit line to account for errors
149   associated with antenna height uncertainty, firn compaction, and advection.
150
151   **Accumulation rate**
152   Measurements of accumulation in the interior of Thwaites Glacier are sparse. Kaspari et
153   al. (2004) report measurements from eight firn/ice cores in central West Antarctica. The
154   one core in the Thwaites Glacier catchment indicated average accumulation of 0.48 m yr^{-1}
155   (reported accumulation rates are in ice equivalent) over the period 1922-1991 Several
156   studies have used these data to help constrain regional climate models (e.g. Arthern et al.,
157   2006; Monaghan et al. 2006; van de Berg et al., 2006); estimates of accumulation in the
158   Thwaites catchment range from 0.4 to 0.65 m yr^{-1}. Recent work using a combination of
159   radar-detected shallow layers and firn cores found an average accumulation rate of
160   0.46±0.07 m yr^{-1} for the entire Thwaites catchment (Medley et al., 2013). For our study
161   area, the accumulation rate for each segment was calculated from the Medley et al.
162   (2013) accumulation map and had an average of 0.54 m yr^{-1}. The study area was well
163   covered by radar lines, reducing the uncertainty in the accumulation rate for each
164   segment to an estimated 0.05 m yr^{-1}.
165
166
167   **RESULTS**
168   **Ice-flow Direction**
169   The ice flow directions defined by radar-detected features and by InSAR differed by an
170   average of 2.5˚ in the middle tributary but substantially more in the other tributaries.
171   Figure 3 shows the average direction difference for each tributary. The InSAR directions
172   are rotated eastward (towards the top) by an average of 8.3 degrees in the eastern
173   tributary relative to the radar-defined directions. The disagreement is even larger for the
174   two western tributaries although the number of measurements of radar-defined flow lines
175   is smaller. The InSAR directions are rotated westward by an average of 12.9˚ in the
176   southwestern tributary and 22.4˚ in the western tributary.
177
178   Differences in ice flow direction could indicate a change in flow pattern over the past few
179   centuries; however, the difference might also be due to inaccuracies of one of the
180   methods. To examine potential inaccuracies, we compare the flow directions to those
181   measured at 5 GPS stations. Stations A, B and C are located in the eastern tributary and D
182   and E are in the middle tributary. No GPS units were deployed in the southwestern and
183   western tributaries where differences are largest. The radar-detected and GPS directions

184   differed by up to 3.4˚ , which is within the combined uncertainty; the differences are not
185   biased in one direction (Table 1). The maximum difference between InSAR and GPS
186   directions is 12.7˚. The agreement is good in the middle tributary, but consistently rotated
187   eastward in the eastern tributary.
188
189   The agreement of radar-detected and GPS directions in the eastern tributary indicate that
190   the InSAR directions are incorrect. The large differences in the western and southwestern
191   tributaries are also likely caused by incorrect InSAR directions. Close inspection of the
192   western tributary shows that radar-detected directions follow the bedrock trough and the
193   direction of increasing ice velocity. In contrast, InSAR velocity vectors are oriented such
194   that an ice particle that starts in the center of tributary travels across the margin into
195   slower moving ice.
196
197   **Flux Imbalance and Uncertainty**
198   Flow bands can be tracked between six to eight radar lines in both the eastern and middle
199   tributaries. This is a distance of 80 to 110 km and presents the opportunity to determine
200   thinning rates from mass conservation. The large differences between the ice-flow
201   directions determined by InSAR and those determined by radar and by GPS for the
202   eastern tributary prevent a reliable flow band analysis. However, the agreement of all
203   three data sets in the middle tributary suggest the InSAR velocities may be sufficiently
204   accurate to allow the thinning rate to be determined.
205
206   Four flow lines were tracked through at least eight radar lines in the middle tributary. We
207   focus on the large flow band defined by the outer two flow lines (Figure 3) and calculate
208   the flux gate area at the top and bottom of each flow band segment. The flux gate area is
209   the cross-sectional area between two flow lines (Figure 2). Assuming no ice flow across
210   the sides of a flow band, from continuity the flux through the upstream gate equals the
211   flux out the downstream gate plus any mass changes within the flow band:
212
213   $$A_{dn} \times u_{dn} = A_{up} \times u_{up} + (\dot{b} - \dot{h} - \dot{m})SA \qquad\qquad (1)$$
214
215   where A is the flux gate areas, u is the average velocity at the flux gate, $_{dn}$ indicates the
216   downstream gate, $_{up}$ indicates upstream gate, $\dot{b}$ is the ice-equivalent accumulation rate,
217   $\dot{h}$ is the rate of change in ice thickness (positive for thickening), $\dot{m}$ is the rate of basal
218   melting, and SA is the surface area of the flow band. Basal melting through this area is
219   more than an order of magnitude less than $\dot{b}$ (Joughin et al., 2009), and is ignored.
220
221   The flow band width does not accumulate uncertainty because the radar-detected features
222   are identified independently at each radar profile. The uncertainty in the flux gate width
223   is then the uncertainty in defining the features at each end, which we estimate to be a total
224   of 600 m in width. The radar lines are not always perpendicular to the ice flow, so we
225   convert the measured width to the width perpendicular to the ice flow by multiplying by
226   the cosine of the difference between the direction of the radar line and the direction of the
227   ice flow. Up to 11% of bed returns for a flux gate cannot be distinguished; the maximum
228   distance between bed returns is 1 km. Depths vary by up to 50 m over 1-km distances,

but typically variations are less. We interpolate linearly between measured bed returns and estimate that the lack of returns results in less than 5 m depth uncertainty. Uncertainty of the radar wave speed in ice largely cancels at the upstream and downstream gates and we therefore ignore this contribution.

The velocity at the flux gate is determined from the InSAR velocity map. The surface velocity is considered equal to the depth-averaged velocity, i.e. the ice is moving entirely by sliding. Calculations of the international deformation show a maximum of 5 m yr^{-1} of surface motion. This yields less than 1 m yr^{-1} of uncertainty of the depth-averaged velocity, which is an order of magnitude less than the InSAR uncertainty and is not included here.

The net flux, average depth, width, and velocity at each gate are shown in Table 2 as well as the associated uncertainties. The total flux uncertainty is calculated assuming standard propagation of independent errors. The uncertainty for each flux gate is 5% to 10% of the total flux and is dominated by the velocity.

The net flux imbalance as well as the equivalent change in ice thickness averaged of the surface area is shown in Table 3 for each segment. A positive value indicates more mass is entering the segment, which results in thickening; a negative value indicates thinning. The uncertainty for any segment is often an order of magnitude larger than the calculated thickness change. This arises because for short segments (15.6 km), the flux difference is small and the velocity uncertainties at both flux gates dominate the estimate.

The full 110 km flow band allows a more robust estimate of average thinning and is also shown in Table 2. The average thinning rate is -0.47±0.42 m yr^{-1}. L1 has a large velocity uncertainty, so calculating the thinning from L2-L8 finds nearly the same thinning rate of -0.49 m yr^{-1} but reduces the uncertainty to 0.34 m yr^{-1}.

Additional Velocity Uncertainty
The uncertainty in the flux analysis is dominated by the velocity uncertainty. Thus far, we have assumed that the formal and slope-dependent uncertainties sufficiently characterized the velocity uncertainty, as in the Ross Drainage where the InSAR velocities were compared with ground-based measurements (Joughin et al., 2002). However, Thwaites glacier is a difficult area for InSAR measurements. High accumulation rates and low radar reflectivity lead to poor coherence and rapid temporal decorrelation between images. As a result, in many parts of the glacier, only a few short-repeat image pairs from ERS are available. These estimates have larger errors and biases than those based on the 23-or 38-day pairs available elsewhere.

The InSAR and GPS velocities are compared in Table 2. In the eastern tributary, where the flow directions do not agree, the InSAR velocities exceed the GPS velocities by 16% at site A and 13% at site B, which is more than the formal and slope-dependent uncertainty and indicates that there is additional uncertainty from the short repeat interval. In the middle tributary, the InSAR velocity is 5% greater at site D and slightly outside of the uncertainty; at site E, they agree within the uncertainty. The comparison

23

275 suggests that uncertainty in the velocity magnitude is reasonable in places where the
276 direction is accurate, and inaccurate directions are an indication that the magnitude may
277 be off as well.
278
279 At four of the five GPS locations, the InSAR velocity is greater than the GPS velocity. It
280 is unlikely that the difference is caused by the different times at which the velocities were
281 measured; InSAR velocities are from 1996 and GPS velocities are from 2007-08 summer
282 season. Thwaites Glacier is most likely accelerating in response to recent terminus
283 changes, so the GPS velocities would be expected to be greater than the InSAR
284 velocities.
285
286 We also compared the GPS velocities with the velocity map of Rignot et al. (2011).
287 Rignot et al. use a combination of the 1996 ERS 1 and 2 satellite passes (from which the
288 Joughin et al., 2009 velocities were calculated) as well as the 2007-2008 PALSAR data,
289 which does not cover the entire region. The Rignot et al. InSAR velocity directions agree
290 well with the GPS directions in the eastern tributary and do not differ by more than $2°.5$
291 (Table 1); however, the directions differ by 9.5 and $5.3°$ in th e middle tributary. This is
292 the opposite of the Joughin et al. velocities, which agree well in the middle tributary but
293 not the eastern tributary. There are gaps in the Rignot et al. velocity map preventing
294 comparison with the radar-detected directions in the western and southwestern tributaries.
295
296 The Rignot et al. velocities are less than the GPS velocities at 4 of the five GPS locations,
297 and the differences exceed the stated velocity uncertainties at 3 of the 5 sites. The
298 velocity differences often exceed the stated uncertainties by more than an order of
299 magnitude. At site D, Rignot et al. (2011) give a 1 m yr^{-1} velocity uncertainty yet the GPS
300 velocity is 28 m yr^{-1} (12%) greater; at site E, the GPS velocity is 15 m yr^{-1} (14%) greater
301 although the stated uncertainty is 1 m yr^{-1}. Rignot et al. (2011) velocities in the eastern
302 tributary agree better with the GPS velocities with the difference exceeding the
303 uncertainty at only one of the three sites. This suggests that the velocity magnitudes are
304 more accurate where the directions agree, as observed with the Joughin et al. velocities.
305
306 The large differences between the GPS and both InSAR velocities (and even larger
307 differences between the two InSAR maps) suggest that the InSAR uncertainties that
308 accompanied the data are too small and need to include uncertainty associated with short
309 repeat intervals. This increases the uncertainty of the flux analysis presented above and
310 reduces the confidence in the thinning estimates. The large velocity uncertainties
311 dominate the total uncertainty of the flux analyses; velocity uncertainty of less than a
312 meter per year is necessary to achieve similar precision as satellite altimetry methods.
313
314 GPS velocities provide the necessary precision, but lack spatial coverage. If the velocities
315 at the L2 and L8 gates (from Joughin et al. 2009) are scaled to the GPS velocities, the
316 inferred thinning is reduced to 0.36 m yr^{-1}, closer in agreement with the altimetry
317 methods. The uncertainty is difficult to estimate because while the GPS velocities have
318 an uncertainty of 0.2 m yr^{-1}, a constant scaling of all velocities along the flux gate is
319 likely too simplistic. If only the GPS velocity uncertainty is used, the total uncertainty is
320 0.08 m yr^{-1}, which is similar to the precision of the laser altimetry techniques and the

321 uncertainty in accumulation dominates the estimate; however, multiple GPS
322 measurements at the flux gates would be necessary to reduce the velocity.
323
324
325 **CONCLUSIONS**
326 Flow lines can be effectively determined using radar-detected features in the interior of
327 Thwaites Glacier where other means of identifying flow directions, such as flow stripes
328 and crevasses at shear margins, are not possible. Comparisons of GPS and radar-detected
329 flow directions with InSAR directions indicate that InSAR velocities alone are not
330 sufficient to define flow lines and flow bands.
331
332 A flux analysis in the middle tributary where the InSAR velocity directions agree well
333 with the GPS and radar-detected directions indicates thinning of -0.49 m yr^{-1}, but with a
334 large uncertainty of 0.34 m yr^{-1}. Further, InSAR velocities often differ from the GPS
335 velocities by more than InSAR uncertainties, indicating that the flux analysis uncertainty
336 is too low. InSAR velocities provide a good overview of the velocity structure of
337 Thwaites Glacier and are sufficient for many glaciological investigates (Joughin et al.,
338 2009; Rignot et al., 2011) but are not accurate enough to be used in a flux analyses in the
339 interior portions of the glacier.
340
345
346

References

Arthern, R.J., D.P. Winebrenner and D.G. Vaughan, 2006. Antarctic snow accumulation mapped using polarization of 4.3-cm wavelength microwave emission. *J. Geophys. Re*s. **111**(D6).

Blankenship, D. D., and D. A. Young, 2012, AGASEA ice thickness profile data from the Amundsen Sea Embayment, Antarctica, Digital media, National Snow and Ice Data Center, Boulder, Colorado USA, doi:10.7265/N5W95730.

Chen, G. 1998. GPS kinematics positioning for airborne laser altimetry at Long Valley, California. Ph.D. Thesis, Massachusetts Institute of Technology, Cambridge, Massachusetts, USA.

Conway, H., G. A. Catania, and T. Fudge (2010), Ice flow history of the Thwaites Glacier, West Antarctica, Digital media, National Snow and Ice Data Center, Boulder, Colorado USA, doi:10.7265/N5RR1W6X.

de Berg, W.J.V., M.R. van den Broeke, C.H. Reijmer and E. van Meijgaard 2006. Reassessment of the Antarctic surface mass balance using calibrated output of a regional atmospheric climate model. *J. Geophys. Res.***111**(D11).

Fahnestock, M.A., T.A. Scambos, R.S. Bindschadler, and G. Kvaran, 2000. A millennium of variable ice flow recorded by the Ross Ice Shelf, Antarctica, *J. Glac.*, **46**(155), 652-655.

Helsen, M.M., M.R. van den Broeke, R.S.W. van de Wal, W.J. van de Berg, E. van Meijgaard, C.H. Davis, Y.H. Li and I. Goodwin, 2008. Elevation changes in Antarctica mainly determined by accumulation variability. *Science*, **320**(5883), 1626-1629.

Holt, J.W., D.D. Blankenship, D.L. Morse, D.A. Young, M.E. Peters, S.D. Kempf, T.G. Richter, D.G. Vaughan and H.F.J. Corr, 2006. New boundary conditions for the West Antarctic Ice Sheet: Subglacial topography of the Thwaites and Smith glacier catchments. *Geophys Res. Letts.* **33**(9).

Joughin, I., S. Tulaczyk, R. Bindschadler, and S.F. Price, 2002. Changes in west Antarctic ice stream velocities,: Observations and analysis, *J. Geophys. Res.*, **107**(B11), 2289.

Joughin, I., S. Tulaczyk, J.L. Bamber, D. Blankenship, J.W. Holt, T. Scambos and D.G. Vaughan, 2009. Basal conditions for Pine Island and Thwaites Glaciers, West Antarctica, determined using satellite and airborne data. *J. Glaciol.* **55**(190): 245-257.

Joughin, I., B.E. Smith and D.M. Holland, 2010a. Sensitivity of 21st century sea level to ocean-induced thinning of Pine Island Glacier, Antarctica. Geophys. Res. Letts, 37, L20502, doi:10.1029/2010GL044819.

Joughin, I., B.E. Smith, I.M. Howat, T. Scambos, and T. Moon, 2010b. Greenland flow variability from ice-sheet-wide velocity mapping, *J. Glaciol.*, **56**(197), 415-430.

Kaspari, S., P.A. Mayewski, D.A. Dixon, V.B. Spikes, S.B. Sneed, M.J. Handley and G.S. Hamilton, 2004. Climate variability in West Antarctica derived from annual accumulation-rate records from ITASE firn/ice cores. *Annals Glaciol*, 585-594.

King, M. 2004. Rigorous GPS data-processing strategies for glaciological applications. *J. Glaciol.*, **50**(171), 601-608.

MacGregor, J.A., G.A. Catania, M.S. Markowski, and A.G. Andrews, Widespread rifting and retreat of ice-shelf margins in the eastern Amundsen Sea Embayment between 1972 and 2011. *J. Glac.*, **58**(209), 458-466.

MacGregor, J.A. and 7 others, in press. Weak bed control of the eastern shear margin of Thwaites Glacier, *J. Glac.*

Medley, B, and 13 others, in press. Airborne-radar and ice-core observations of annual snow accumulation over Thwaires Glacier, West Antarctica confirm the spatio-temporal variability of global and regional atmospheric models, *Geophys. Res. Lett.*

Monaghan, A.J., D.H. Bromwich and S.H. Wang, 2006b. Recent trends in Antarctic snow accumulation from Polar MM5 simulations. *Philosophical Transactions of the Royal Society a-Mathematical Physical and Engineering Sciences*, **364**(1844): 1683-1708.

Ng, F. and H. Conway 2004. Fast-flow signature in the stagnated Kamb Ice Stream, West

398   Antarctica. *Geology*, **32**(6), 481-484.

399   Payne, A.J., A. Vieli, A.P. Shepherd, D.J. Wingham and E. Rignot, 2004. Recent dramatic
400   thinning of largest West Antarctic ice stream triggered by oceans. *Geophys. Res. Letts.* **31**(23).

401   Peters, M.E., D.D. Blankenship and D.L. Morse 2005. Analysis techniques for coherent airborne
402   radar sounding: Application to West Antarctic ice streams. *J. Geophys. Res.* **110**(B6).

403   Pritchard, H.D., R.J. Arthern, D.G. Vaughan and L.A. Edwards 2009. Extensive dynamic
404   thinning on the margins of the Greenland and Antarctic ice sheets. *Nature*, **461**(7266), 971-975.

405   Pritchard, H.D., S.R.M. Ligtenberg, H.A. Fricker, D.G. Vaughn, M.R. van den Broeke, and L.
406   Padman, 2012. Antarctic ice-sheet loss driven by basal melting of ice shelves. *Nature*,
407   **484**(7395), 502-505.

408   Rignot, E. 2008. Changes in West Antarctic ice stream dynamics observed with ALOS PALSAR
409   data. *Geophys. Res. Letts*. **35**(12), 5.

410   Rignot, E., D.G. Vaughan, M. Schmeltz, T. Dupont and D. MacAyeal, 2002. Acceleration of Pine
411   Island and Thwaites Glaciers, West Antarctica. *Annals Glaciol.* **34**, 189-194.

412   Rignot, E., J.L. Bamber, M.R. Van Den Broeke, C. Davis, Y.H. Li, W.J. Van De Berg and E. Van
413   Meijgaard 2008a. Recent Antarctic ice mass loss from radar interferometry and regional
414   climate modelling. *Nature Geosci.* **1**(2), 106-110.

415   Rignot, E., J. Mouginot, and B. Scheuchl, 2011. Ice Flow of the Antarctic Ice Sheet. *Science* **333,**
416   1427-1430.

417   Shabtaie, S., C.R. Bentley, R.A. Bindschadler, and D.R. MacAyeal, 1988. Mass-balance studies
418   of Ice Streams A, B, and C, West Antarctica, and posible surging behavior of Ice Stream B,
419   *Ann. Glac.*, **11**, 137-150.

420   Shepherd, A. and 47 others, 2012. A Reconciled Estimate of Ice-Sheet Mass Balance, *Science*
421   **338**(6111), 1183-1189.

422   van den Broeke, M., W.J. van de Berg and E. van Meijgaard 2006. Snowfall in coastal West
423   Antarctica much greater than previously assumed. *Geophys. Res. Letts*. **33**(2).

424   Zwally, H.J., M.B. Giovinetto, J. Li, H.G. Cornejo, M.A. Beckley, A.C. Brenner, J.L. Saba and
425   D.H. Yi, 2005. Mass changes of the Greenland and Antarctic ice sheets and shelves and
426   contributions to sea-level rise: 1992-2002. *J. Glaciol.* **51**(175): 509-527.

Table 1: Comparison of Ice-flow Directions

Tributary	Station	GPS Direction	Radar-detected Direction	InSAR Direction		GPS minus Radar-Detected	GPS minus InSAR
Eastern	A	236.2	233.0	239.6		3.2	-3.4
Eastern	B	231.6	229.8	244.2		1.7	-12.7
Eastern	C	210.1	213.5	220.1		-3.4	-10.0
Middle	D	269.2	270.3	266.9		-1.1	2.4
Middle	E	267.4	264.0	266.7		3.4	0.7

Table 2: Values at Flux Gates

Radar Line	Flux (km^3)	Depth (m)	Width (m)	Velocity (m yr^{-1})	Depth Flux Uncertainty (km^3)	Width Flux Uncertainty (km^3)	Velocity Flux Uncertainty (km^3)
L1	**30.0 ±2.4**	2313 ±5	42263 ±600	304 ±25	0.1	0.4	2.4
L2	**29.4 ±1.3**	2409 ±5	47993 ±600	250 ±11	0.1	0.4	1.3
L3	**29.9 ±1.4**	2470 ±5	54884 ±600	215 ±10	0.1	0.3	1.3
L4	**28.7 ±1.5**	2523 ±5	63620 ±600	174 ±10	0.1	0.3	1.5
L5	**26.9 ±1.7**	2434 ±5	72582 ±600	150 ±10	0.1	0.2	1.7
L6	**25.4 ±1.9**	2528 ±5	74870 ±600	134 ±10	0.0	0.2	1.9
L7	**23.6 ±1.7**	2735 ±5	76886 ±600	112 ±8	0.0	0.2	1.7
L8	**22.8 ±1.7**	2774 ±5	83688 ±600	96 ±7	0.0	0.2	1.7

Table 3: Flowband Ice Thickness Change and Uncertainty

Flowband	Surface Area (km^2)	Accumulation (m a^{-1})	Surface Flux (km^3)	Net Flux (km^3)	Thickness Change (m a^{-1})	Thickness Change Uncertainty from Depth (m a^{-1})	Thickness Change Uncertainty from Width (m a^{-1})	Thickness Change Uncertainty from Velocity (m a^{-1})	Thickness Change Uncertainty from Accumulation (m a^{-1})	Total Thickness Change Uncertainty (m a^{-1})
L1-L2	704	0.59	0.39	-0.3 ±4.0	-0.37	0.12	0.79	3.87	0.05	3.95
L2-L3	806	0.57	0.44	0.9 ±2.4	1.16	0.10	0.60	2.27	0.05	2.35
L3-L4	923	0.55	0.51	-0.7 ±2.2	-0.73	0.09	0.45	2.18	0.05	2.23
L4-L5	1064	0.53	0.59	-1.2 ±2.2	-1.09	0.07	0.32	2.14	0.05	2.17
L5-L6	1154	0.53	0.63	-0.9 ±2.2	-0.82	0.06	0.26	2.20	0.05	2.22
L6-L7	1185	0.54	0.65	-1.1 ±2.1	-0.93	0.06	0.23	2.13	0.05	2.15
L7-L8	1257	0.53	0.69	-0.1 ±1.9	-0.09	0.05	0.19	1.87	0.05	1.88
L1-L8	7093	0.54	3.90	-3.3	-0.47	0.01	0.06	0.41	0.05	0.42
L2-L8	6389	0.54	3.51	-3.1	**-0.49**	0.01	0.06	0.33	0.05	**0.34**
L2-L8 GPS	6389	0.54	3.51	-2.2	-0.36	0.01	0.06	*0.01**	0.05	*0.08**

* The velocitiy uncertainty is from the GPS uncertainty only and does not include uncertainty due to spatial variation

Table 4: Velocity Comparison

Tributary	Station	GPS Velocity (m yr^{-1})	Joughin InSAR Velocity (m yr^{-1})	Rignot InSAR Velocity (m yr^{-1})		GPS - Joughin InSAR (m yr^{-1})	Joughin InSAR uncertainty (m yr^{-1})	GPS-Rignot InSAR (m yr^{-1})	Rignot InSAR Uncertainty (m yr^{-1})
Eastern	A	140.6	164.4	128.8		**23.8**	7.7	**-11.8**	3.0
Eastern	B	111.0	125.5	108.9		**14.5**	7.8	-2.1	3.2
Eastern	C	108.1	99.8	108.4		-8.3	15.9	0.3	3.0
Middle	D	249.3	263.5	221.1		**14.2**	12.0	**-28.2**	1.0
Middle	E	113.2	116.4	97.8		3.2	7.9	**-15.4**	1.0
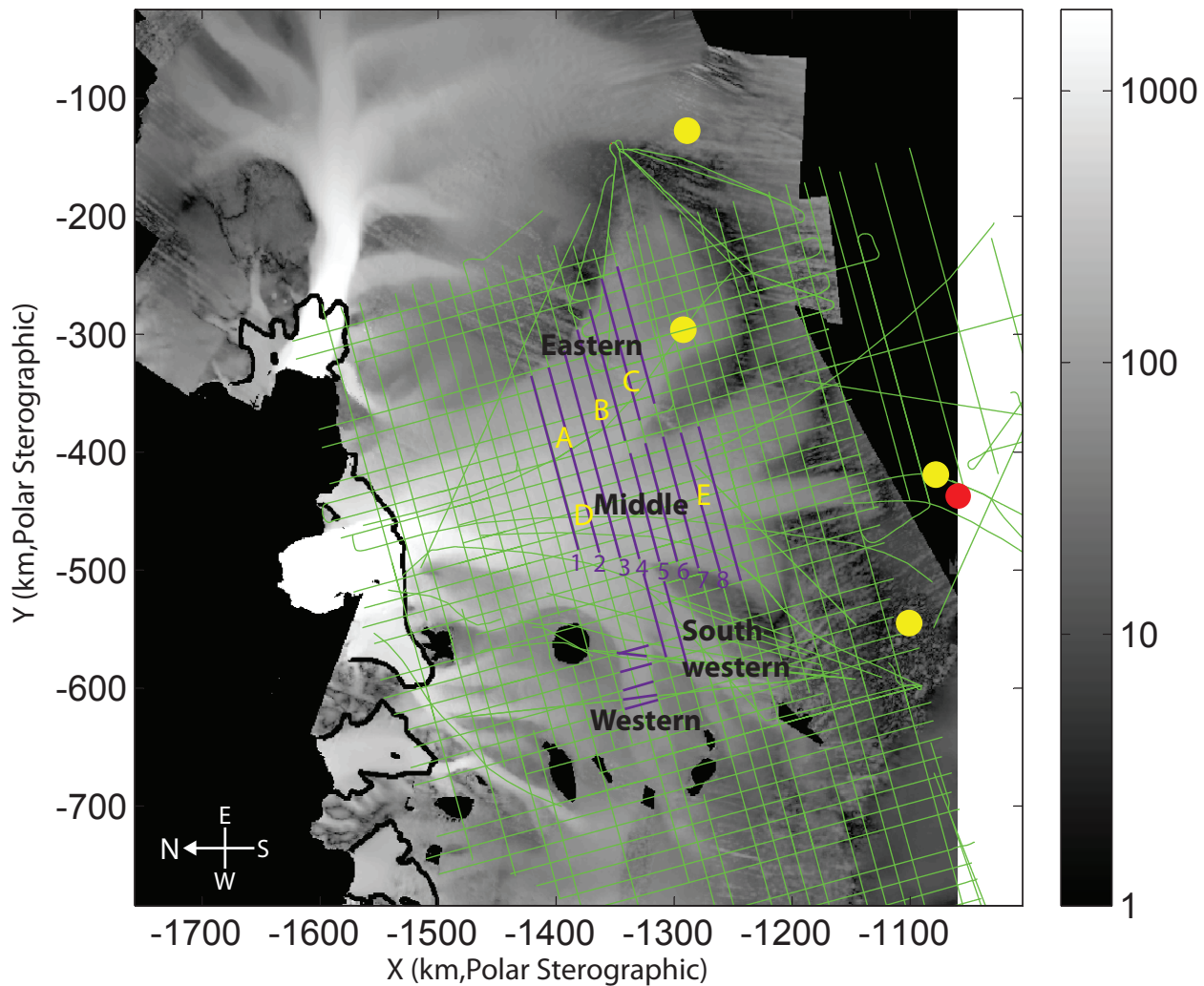
Figure 1: InSAR velocity map (Joughin et al., 2009) overlain by radar lines (Holt et al., 2006). Purple lines indicate areas where radar-detected features were tracked. Yellow circles are shallow core locations from US-ITASE. Red circle is WAIS DIVIDE ice core site. Letters A-E are GPS locations.

Figure Flowlines Radio-echogram
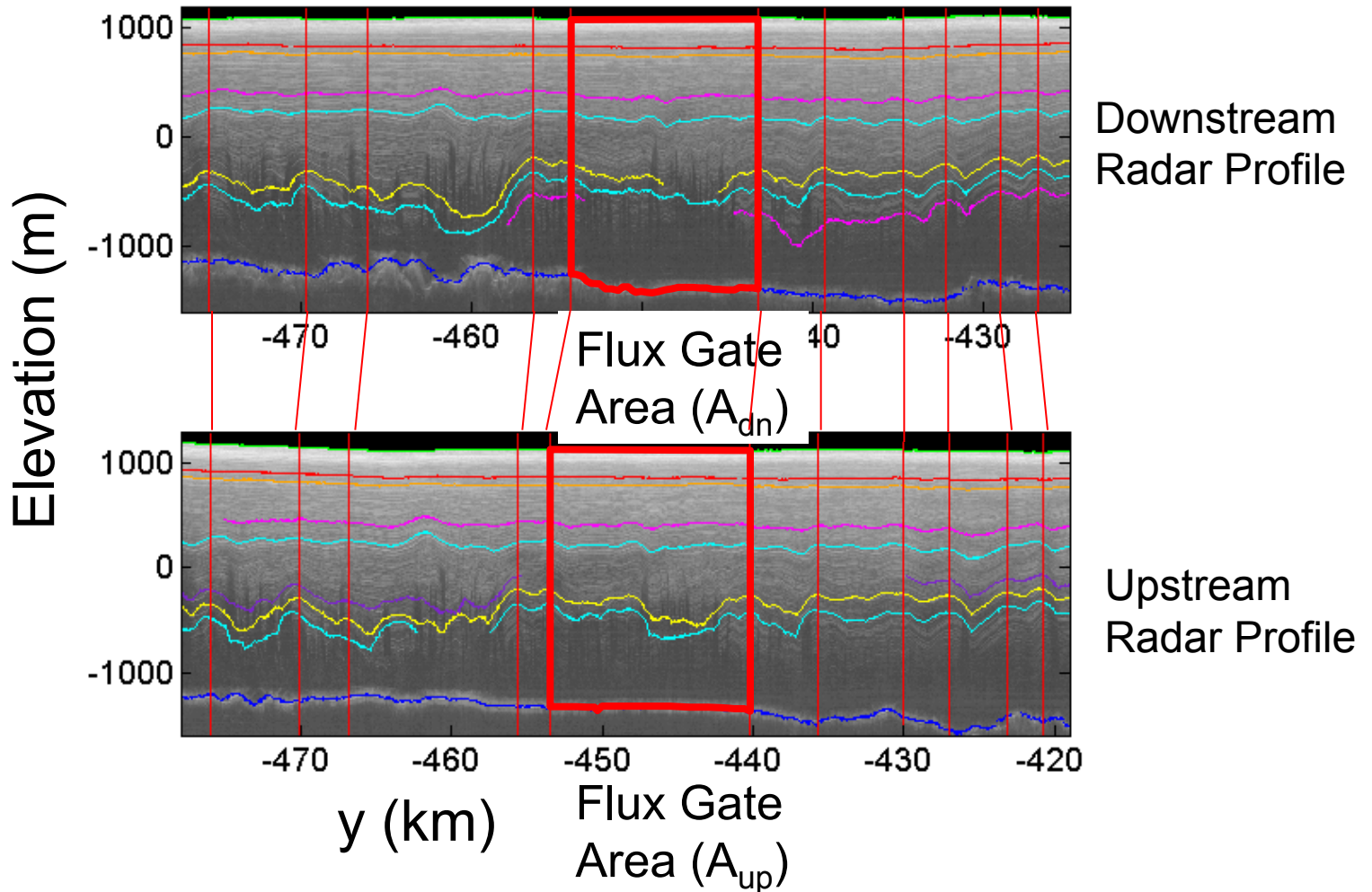
Figure 2: Two radio-echograms with internal layers traced in different colors. Flow-lines from matching distinct layer patterns between radio-echograms are shown by thin red lines. An example flux-gate area defined by two flowlines is outlined in thick red.
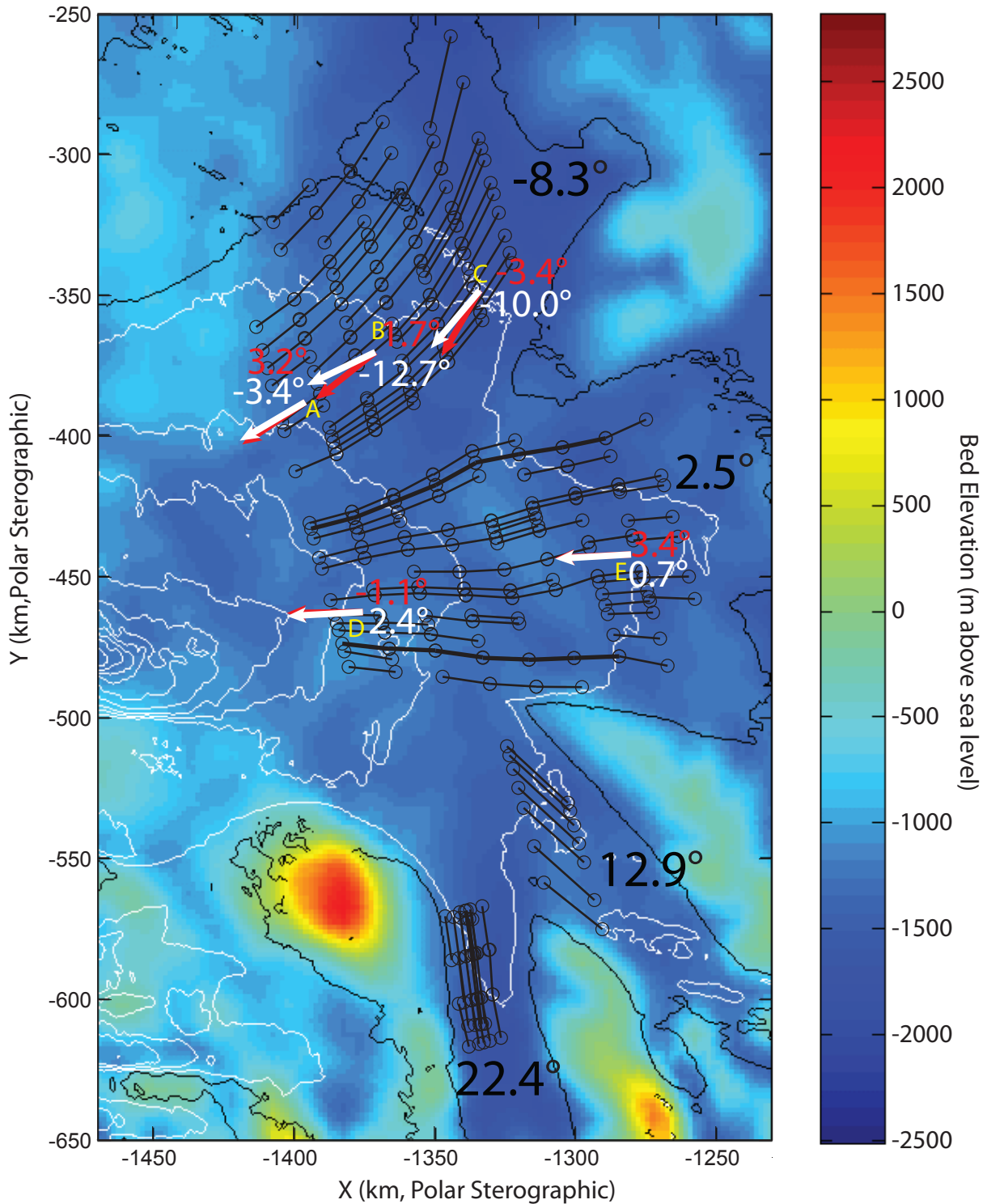
Figure 3: Radar-detected flow lines shown with black circles connected by thin black lines. GPS velocities are black arrows. InSAR velocities at GPS locations are red arrows. Large black numbers are average direction difference (°) between radar-detected and InSAR ice flow directions. Small white numbers are direction difference between InSAR and GPS. Small red numbers are direction difference between radar-detected and GPS. Background color is bedrock elevation.

Chapter 4: *Onset of deglacial warming in central West Antarctica driven by local orbital forcing*

Originally published in Nature

The lead author was WAIS Divide Project Members to acknowledge the contributions of the many, many people it took to recover the core and obtain the fantastic records. It is the first community paper from a US-led ice core project. I was the lead corresponding author. The main text is in Chapter 4 and the supplementary material in Chapter 5. In addition, Appendix A contains additional information about the electrical measurements that formed the basis of the timescale. This paper developed the first annually resolved timescale from the Southern Hemisphere that extends to the last glacial period. The timescale was used to infer the timing of accumulation rate changes and was combined with the water stable-isotope record to determine the surface temperature history. We found that West Antarctic warming was ongoing prior to a Northern Hemisphere trigger and was likely caused by increasing local insolation. Using climate modeling we showed that West Antarctic is sensitive to sea-ice changes while interior East Antarctica is largely isolated from sea-ice changes in coastal Antarctic waters.

This paper required the efforts of many people. A description of author contributions is at the end of the paper. I developed the timescale, the accumulation rate history, and led the climate interpretation which was largely based on the stable isotope record from Eric Steig's lab. I also interpreted the sea-salt sodium record from Joe McConnell's lab and was the primary author of the manuscript.

LETTER

Onset of deglacial warming in West Antarctica driven by local orbital forcing

WAIS Divide Project Members*

The cause of warming in the Southern Hemisphere during the most recent deglaciation remains a matter of debate[1,2]. Hypotheses for a Northern Hemisphere trigger, through oceanic redistributions of heat, are based in part on the abrupt onset of warming seen in East Antarctic ice cores and dated to 18,000 years ago, which is several thousand years after high-latitude Northern Hemisphere summer insolation intensity began increasing from its minimum, approximately 24,000 years ago[3,4]. An alternative explanation is that local solar insolation changes cause the Southern Hemisphere to warm independently[2,5]. Here we present results from a new, annually resolved ice-core record from West Antarctica that reconciles these two views. The records show that 18,000 years ago snow accumulation in West Antarctica began increasing, coincident with increasing carbon dioxide concentrations, warming in East Antarctica and cooling in the Northern Hemisphere[6] associated with an abrupt decrease in Atlantic meridional overturning circulation[7]. However, significant warming in West Antarctica began at least 2,000 years earlier. Circum-Antarctic sea-ice decline, driven by increasing local insolation, is the likely cause of this warming. The marine-influenced West Antarctic records suggest a more active role for the Southern Ocean in the onset of deglaciation than is inferred from ice cores in the East Antarctic interior, which are largely isolated from sea-ice changes.

Exceptional records of Southern Hemisphere climate change come from Antarctic ice cores[2,6,7]. Most of these records are from high-altitude sites on the East Antarctic plateau. Questions about the reliability of the two previous deep West Antarctic ice-core records result in those records often being excluded from reconstructions of Antarctic climate[4,8]. Because the climate of West Antarctica is distinct from that of interior East Antarctica, the exclusion of West Antarctic records may result in an incomplete picture of past Antarctic and Southern Ocean climate change. Interior West Antarctica is lower in elevation and more subject to the influence of marine air masses than interior East Antarctica, which is surrounded by a steep topographic slope[9,10]. Marine-influenced locations are important because they more directly reflect atmospheric conditions resulting from changes in ocean circulation and sea ice. However, ice-core records from coastal sites are often difficult to interpret because of complicated ice-flow and elevation histories. The West Antarctic Ice Sheet (WAIS) Divide ice core (WDC), in central West Antarctica, is unique in coming from a location that has experienced minimal elevation change[11], is strongly influenced by marine conditions[9] and has a relatively high snow-accumulation rate, making it possible to obtain an accurately dated record with high temporal resolution.

Drilling of WDC was completed in December 2011 to a depth of 3,405 m. Drilling was halted ~50 m above the bedrock to avoid contaminating the basal water system. WDC is situated 24 km west of the Ross–Amundsen ice-flow divide and 160 km east of the Byrd ice-core site (Supplementary Fig. 1). The elevation is 1,766 m; the present-day snow accumulation rate is 22 cm yr^{-1} (ice equivalent) and the average temperature is approximately $-30\,^\circ$C. The age of the oldest recovered ice is ~68 kyr. The WDC06A-7 timescale is based on the identification of annual layers to 29.6 kyr ago using primarily electrical measurements

(Methods). To validate WDC06A-7, we compare times of abrupt changes in atmospheric methane concentration (Supplementary Information) with the Greenland Ice Core Chronology 2005[12] (GICC05). We also compare the methane variations in WDC with abrupt changes in a speleothem δ^{18}O record from Hulu Cave, China. The difference in age between the ice and gas at a given depth is calculated using a steady-state firn-densification model and is always less than 500 yr. The age differences between WDC06A-7 and GICC05 and between WDC06A-7 and the Hulu Cave timescale are much less than the independent timescale uncertainties (Supplementary Fig. 6).

We interpret δ^{18}O of ice (Methods) as annual-mean surface air temperature, as supported by independent estimates of temperature from borehole thermometry[13]. WDC has many similarities with other records (Fig. 1) and resolves Antarctic Isotope Maximum (AIM) events clearly. The late Holocene WDC record shows cooling, suggesting that the increase in δ^{18}O at Byrd over the past few thousand years resulted from ice advection and thinning[11]. The abrupt increase in δ^{18}O ~22 kyr ago at Siple Dome is not observed at WDC. The AIM1 peak and the subsequent Antarctic Cold Reversal (ACR; 14.5–12.9 kyr ago) are more pronounced in WDC than at Byrd and Siple Dome, possibly owing to discontinuous sampling of the Byrd core and thinning of Siple Dome.

The most rapid warming at WDC occurred after the ACR and culminated at AIM0. The timing of AIM0 is difficult to define because it is composed of two peaks, one 11.95 kyr ago and the other 11.6 kyr ago. The ice accumulation rate at WDC increased abruptly by 37% in the 400 yr between 12.0 and 11.6 kyr ago (Supplementary Fig. 2). The increase in ice accumulation with little change in δ^{18}O shows that the accumulation rate is not controlled strictly by temperature. Abrupt changes in accumulation cannot be recognized in most other Antarctic ice cores because their timescales lack sufficient resolution; it is thus unknown whether this event is specific to WDC or whether accumulation increased abruptly over a larger portion of Antarctica.

The coldest period at WDC was between 28 and 22 kyr ago and was interrupted by AIM2, a 1,000-yr warm period between 24 and 23 kyr ago. AIM2 is also prominent in the EPICA Dronning Maud Land (EDML) ice core[7] but is muted or nearly absent in other East Antarctic records[14] (Fig. 1). Other West Antarctic cores also record AIM2, although the low resolution of the Byrd core and the abrupt δ^{18}O increase 22 kyr ago in the Siple Dome core have made this feature difficult to discern. AIM2 illustrates the spatial heterogeneity of Antarctic climate variability during the coldest part of the glacial period.

To investigate deglacial warming across the Antarctic continent, we use a sliding Wilcoxon rank-sum test (Fig. 2) to identify times of significant change in the δ^{18}O records of WDC, EDML and the EPICA Dome C ice core[6] (EDC); we convert the EDC δD record to δ^{18}O using δ^{18}O = $(\delta$D $- 10)/8$. The WDC and EDC timescales can be aligned at a ~150-yr-long acid deposition event[15,16], which eliminates the relative age uncertainty at 18 kyr ago. The rank sum test reveals three important features: gradual deglacial warming at WDC was punctuated by periods of more rapid change; the most abrupt warming
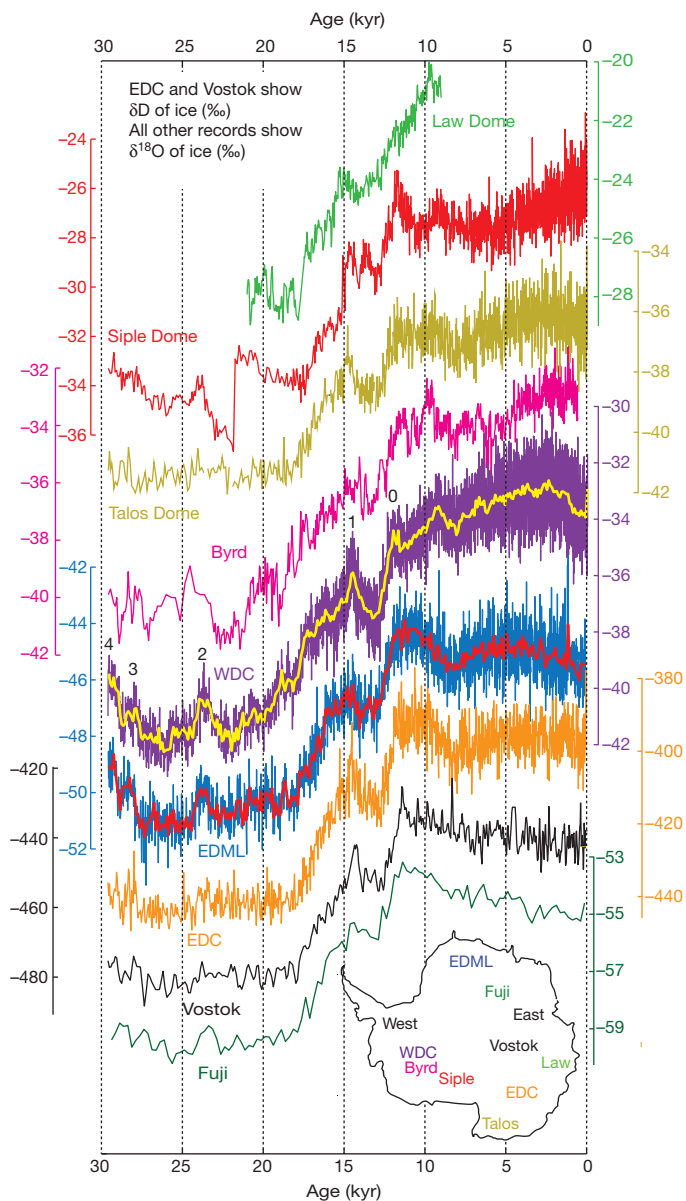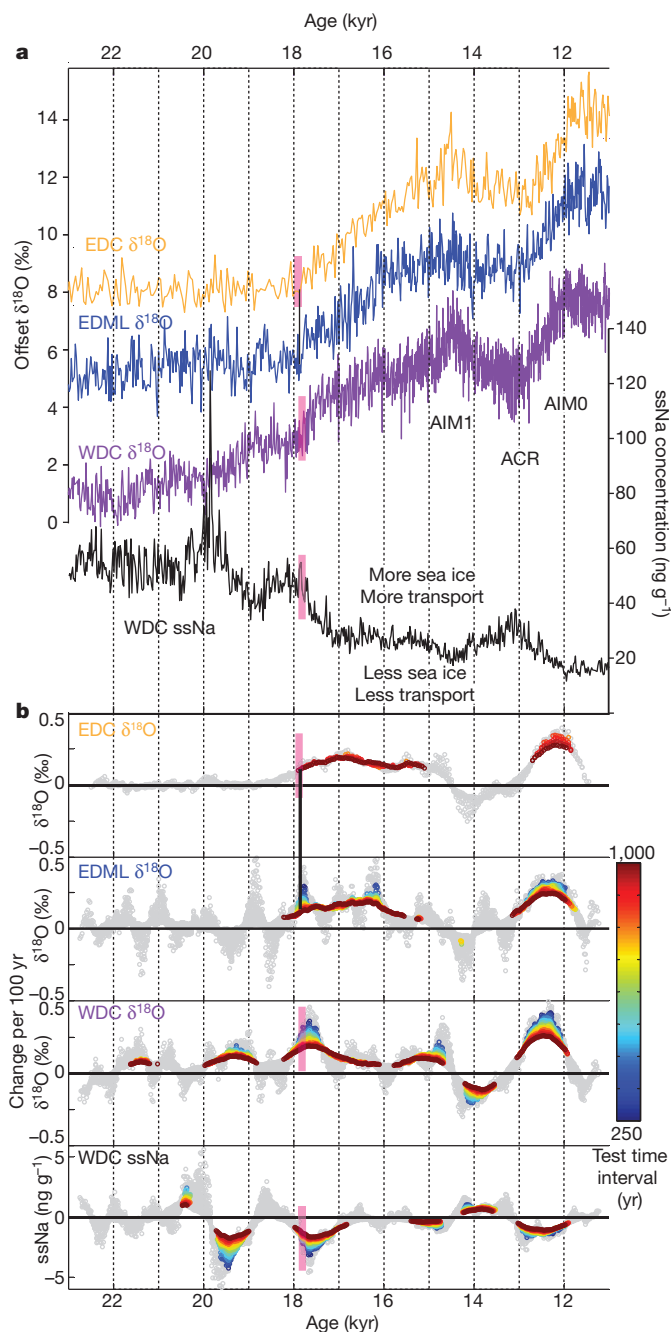
Figure 1 | Antarctic Isotope Records. Water isotope ratios from nine Antarctic ice cores. Inset, outline of Antarctica with the ice-core locations: Law Dome[27] (light green), Siple Dome[28] (red), Byrd[29] (pink), Talos Dome[14] (khaki), WDC (purple, WDC06A-7 timescale), EDML[7] (blue), EDC[6] (orange), Dome Fuji[2] (dark green), Vostok[30] (black). Taylor Dome is not plotted because of timescale uncertainties. All records are at original resolution. Thick lines for WDC and EDML are 50-yr averages. EDML, EDC and Vostok use the Lemieux-Dudon[31] timescale. Numbers above the WDC curve indicate AIM events. ($\delta^{18}O = (^{18}O/^{16}O)_{sample}/(^{18}O/^{16}O)_{VSMOW} - 1$ and $\delta D = (^2H/^1H)_{sample}/(^2H/^1H)_{VSMOW} - 1$).)

Figure 2 | Timing of rapid change in Antarctica. a, Water isotope ratios ($\delta^{18}O$, purple) and ssNa concentrations (black) from WDC on WDC06A-7. EDML[7] (blue) and EDC[6] (orange) $\delta^{18}O$ use the Lemieux-Dudon[31] timescale. Constants have been subtracted from $\delta^{18}O$ records for plotting. Magenta boxes indicate a 150-yr acid deposition event; the black line between EDC and EDML is a volcanic tie point (Methods). ssNa is plotted as 25-yr median values. **b**, Rate of change for $\delta^{18}O$ at WDC, EDML, and EDC and ssNa at WDC. A Wilcoxon rank-sum test (Methods) is used to determine significance. Significant rates of change are coloured by test time interval; rates of change that are not significant are coloured grey.

began at the 18-kyr-ago acid deposition event; and significant warming at WDC began by 20 kyr ago, at least 2,000 yr before significant warming at EDML and EDC.

Further insight into deglacial warming at WDC is gained by investigating the sea-salt sodium (ssNa) record (Methods). Debate remains about whether ssNa on millennial timescales reflects primarily sea-ice production or the strength of atmospheric circulation[17]. In the Amundsen and Ross seas, changes in sea ice and atmospheric circulation are coupled because atmospheric forcing is the dominant control on sea-ice concentration[18]. We interpret ssNa as a proxy for sea-ice extent and a marker of marine changes (Supplementary Information). The rank-sum test reveals that each rapid increase in $\delta^{18}O$, indicating warming, was accompanied by a decrease in ssNa, suggesting less sea ice (Fig. 2).

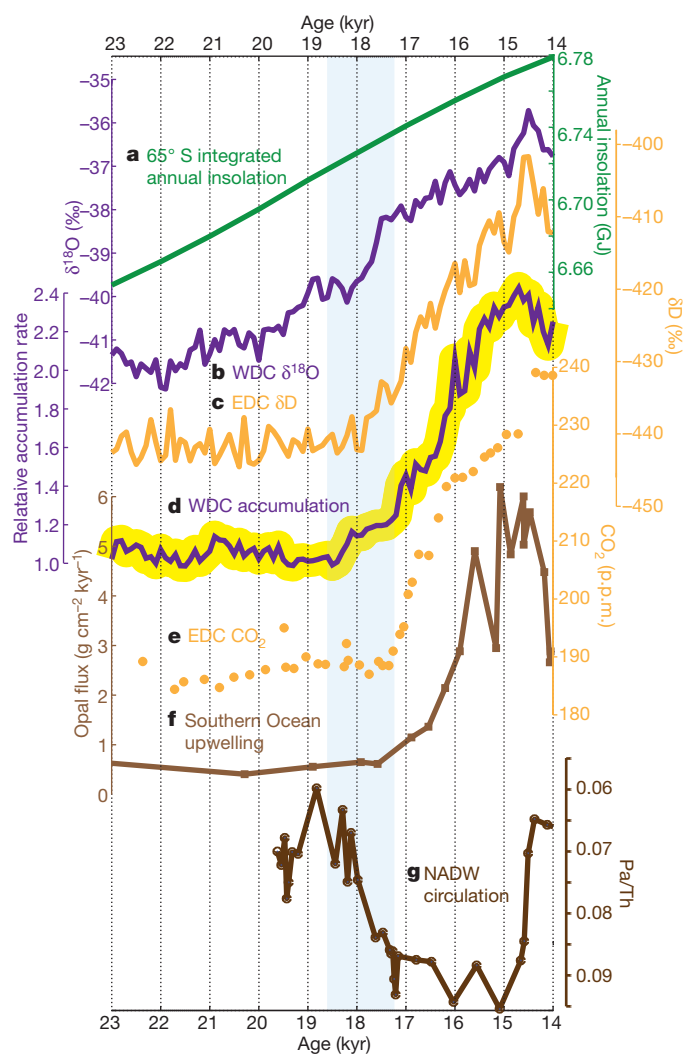Consistent with this, the decrease in $\delta^{18}O$ during the ACR was accompanied by an increase in ssNa.

The accumulation rate at WDC was inferred without assuming a relationship with $\delta^{18}O$ or temperature (Methods). Although uncertainty in the annual-layer interpretation and ice-flow history used to determine the accumulation rate precludes a statistical assessment comparable to that used for the $\delta^{18}O$ and ssNa records, results suggest that an initial increase in accumulation occurred between 18.5 and

17 kyr ago (Fig. 3), consistent with the rapid warming 18 kyr ago. This also coincides with evidence for changes in Southern Ocean upwelling[19], atmospheric carbon dioxide concentration[8,20] and Atlantic meridional overturning circulation[5] (AMOC). The accumulation increase probably results from more frequent or stronger moisture-bearing storms penetrating into West Antarctica. This supports a southward shift[21] or intensification[22] of the mid-latitude westerly storm track, and is consistent with the hypothesis of a decrease in AMOC leading to Southern Hemisphere warming and Northern Hemisphere cooling[3]—the 'bipolar seesaw'.

Both the WDC and the lower-resolution Byrd ice-core records show that warming in West Antarctica began before the decrease in AMOC that has been invoked to explain Southern Hemisphere warming[4,19]. The most significant early warming at WDC occurred between 20 and 18.8 kyr ago, although a period of significant warming also occurred between 22 and 21.5 kyr ago. The magnitude of the warming at WDC before 18 kyr ago is much greater than at EDML or EDC; linear regression of $\delta^{18}O$ between 22 and 18 kyr ago shows that it increased by

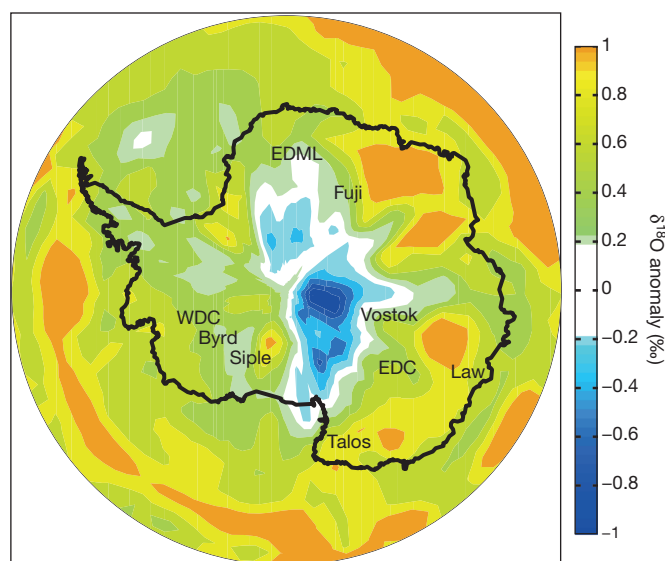2.2‰ at WDC, by 0.4‰ at EDML and by 0.1‰ at EDC (Fig. 2). It is very unlikely that the 2.2‰ increase at WDC can be attributed to elevation change; this magnitude of isotope change would require more than 200 m of ice-sheet thinning, twice the amount of thinning that occurred during the Holocene epoch when the grounding line retreated hundreds of kilometres (Supplementary Information). The subdued warming at EDML and the lack of warming at EDC are consistent with the lack of clear AIM2 signals in some East Antarctic cores, and suggest that cores from the East Antarctic plateau do not capture the full magnitude of Southern Hemisphere climate variability.

There is evidence that warming at WDC before 18 kyr ago is due to decreasing sea ice. The ssNa at WDC began to decrease 20 kyr ago, probably as a result of both decreasing sea-ice extent and decreasing strength of transport from changes in atmospheric circulation. A marine record from the southwest Atlantic Ocean indicates that significant summer and winter sea-ice retreat began before 22 kyr ago[23]. Furthermore, a reduction in sea-ice extent can explain the different magnitude of warming among ice-core sites before 18 kyr ago. The high East Antarctic plateau is largely isolated from coastal changes because the local marine air masses do not have the energy to rise above the steep coastal escarpment[10].

To illustrate the variable sensitivity of different areas in Antarctica to changes in sea-ice extent, we used an atmospheric general circulation model[24]. Using Last Glacial Maximum (LGM) sea surface temperature and sea-ice boundary conditions from a fully coupled model run[25], we performed a control run of the ECHAM4.6 atmospheric model with the LGM sea-ice extent and a comparison run with reduced sea-ice extent (Supplementary Information). Sea surface temperatures are prescribed; the atmospheric circulation therefore responds to the change in sea-ice extent but the sea-ice extent is not further affected by the changes in atmospheric circulation. The magnitude of sea-ice retreat is consistent with evidence for reduced sea ice in the southwest Atlantic between 22 and 18 kyr ago[23]. In response to the sea-ice retreat, all of West Antarctica and coastal East Antarctica is enriched in precipitation-weighted $\delta^{18}O$, whereas interior East Antarctica is little changed or is depleted (Fig. 4). The positive $\delta^{18}O$ anomalies probably extend unrealistically far into the East Antarctic interior because of the low-resolution topography in the climate model. Although the details of the spatial pattern of $\delta^{18}O$ anomalies are dependent on model resolution and on the specified boundary conditions, the greater

Figure 3 | Global records of deglaciation. a, Integrated annual insolation at latitude 65° S. **b**, 100-yr averages of $\delta^{18}O$ at WDC on WDC06A-7. **c**, 100-yr averages of δD at EDC[6] on the Lemieux-Dudon[31] timescale. **d**, Relative accumulation rate (normalized to the mean value between 19.5 and 18.5 kyr ago) at WDC. Yellow shading is the uncertainty in identifying annual layers (Methods). **e**, Atmospheric CO_2 concentration[20] from EDC on the Lemieux-Dudon[31] timescale. **f**, Opal flux[19], a proxy for upwelling, from ocean sediment core TNO57-13-4PC in the South Atlantic. **g**, Pa/Th, a proxy for North Atlantic Deep Water (NADW) circulation[5], from sediment core GCC5. Blue shading indicates a period with relatively abrupt changes in all palaeoclimate records (**b–g**).

Figure 4 | Antarctic $\delta^{18}O$ response to sea-ice decrease. Response of precipitation-weighted $\delta^{18}O$ to an approximately zonally symmetric southward displacement of the sea-ice edge (Supplementary Fig. 9) in the ECHAM4.6 climate model run with LGM boundary conditions.

38

sensitivity of the WAIS Divide region to sea-ice decline compared with locations in interior East Antarctica is clear.

Local orbital forcing is a likely cause of the inferred sea-ice change. Integrated annual insolation at latitude 65° S increased by 1% between 22 and 18 kyr ago. The additional annual insolation is $60\,MJ\,m^{-2}$, which is enough to melt $5\,cm\,m^{-2}$ of sea ice assuming an albedo of 0.75. The increase in integrated summer insolation, where summer is defined as days with insolation above a threshold[26] of $275\,W\,m^{-2}$, is greater than the total annual increase (Supplementary Fig. 10). Thus, the increase comes in summer, when it is most likely to be absorbed by low-albedo open water. The summer duration also begins increasing at 23 kyr ago; longer summers and shorter winters may also contribute to the decrease in sea-ice extent[1]. The effect of an increase in insolation would be amplified by the sea-ice/albedo feedback.

The abrupt onset of East Antarctic warming[4,8], increasing CO_2 (ref. 20) and decreasing AMOC[5] 18 kyr ago has supported the view that deglaciation in the Southern Hemisphere is primarily a response to changes in the Northern Hemisphere[3]. Yet the evidence of warming in West Antarctica and corresponding evidence for sea-ice decline in the southeast Atlantic[23] show that climate changes were ongoing in the Southern Ocean before 18 kyr ago, supporting an important role for local orbital forcing[1]. Warming in the high latitudes of both hemispheres before 18 kyr ago implies little change in the interhemispheric temperature gradient that largely determines the position of the intertropical convergence zone and the position and intensity of the mid-latitude westerlies[21,22]. We propose that when Northern Hemisphere cooling occurred ~18 kyr ago, coupled with an already-warming Southern Hemisphere, the intertropical convergence zone and mid-latitude westerlies shifted southwards in response. The increased wind stress in the Southern Ocean drove upwelling, venting of CO_2 from the deep ocean[19] and warming in both West Antarctica and East Antarctica. The new WDC record thus reveals an active role for the Southern Hemisphere in initiating global deglaciation.

METHODS SUMMARY

The WDC06A-7 timescale is based on measurements of sulphur, sodium, black carbon and electrical conductivity above 577 m (to 2,358 yr before AD 1950), and primarily on electrical measurements below 577 m. Using atmospheric methane as a stratigraphic marker, WDC06A-7 and GICC05 agree to within 100 ± 200 yr at the three abrupt changes between 14.7 and 11.7 kyr ago; WDC06A-7 is older by 500 ± 600 yr at 24 kyr ago, by 250 ± 300 yr at 28 kyr ago and by 350 ± 250 yr at 29 kyr ago (Supplementary Fig. 6). WDC06A-7 agrees within the uncertainties with the Hulu Cave timescale and is older by 50 ± 300 yr at 28 kyr ago and by 100 ± 300 yr at 29 kyr ago.

We measured $\delta^{18}O$ at a resolution of 0.5 m using laser spectroscopy with calibration to Vienna Standard Mean Ocean Water (VSMOW). We report ssNa concentration rather than flux because wet deposition dominates at higher accumulation rates. The accumulation-rate record was derived independently from the stable-isotope record using a one-dimensional ice-flow model to calculate the thinning function.

Periods of significant change in $\delta^{18}O$ and ssNa are identified with a sliding, non-parametric Wilcoxon rank-sum test. The data were averaged to 25-yr resolution for WDC and EDML, and to 50-yr resolution for EDC. We tested pairs of adjacent blocks of data against the null hypothesis of equal medians, performing the test at all points along the record. We assessed change on multiple timescales using a range of block sizes corresponding to time intervals of 250–1,000 yr for WDC and EDML and 500–1,000 yr for EDC. We used an effective 95% a-posteriori confidence requirement; the critical significance level (p) was determined as $1 - 0.95^{1/N}$ where N is the number of test realizations.

We used the ECHAM4.6 atmospheric general circulation model at T42 resolution ($2.8°$ by $2.8°$) with 19 vertical levels and glacial sea surface temperature boundary conditions.

Full Methods and any associated references are available in the online version of the paper.

1. Huybers, P. & Denton, G. Antarctic temperature at orbital timescales controlled by local summer duration. *Nature Geosci.* **1**, 787–792 (2008).
2. Kawamura, K. *et al.* Northern Hemisphere forcing of climatic cycles in Antarctica over the past 360,000 years. *Nature* **448**, 912–916 (2007).
3. Clark, P. U., Pisias, N. G., Stocker, T. F. & Weaver, A. J. The role of the thermohaline circulation in abrupt climate change. *Nature* **415**, 863–869 (2002).
4. Shakun, J. D. *et al.* Global warming preceded by increasing carbon dioxide concentrations during the last deglaciation. *Nature* **484**, 49–54 (2012).
5. McManus, J. F., Francois, R., Gherardi, J. M., Keigwin, L. D. & Brown-Leger, S. Collapse and rapid resumption of Atlantic meridional circulation linked to deglacial climate changes. *Nature* **428**, 834–837 (2004).
6. EPICA community members. Eight glacial cycles from an Antarctic ice core. *Nature* **429**, 623–628 (2004).
7. EPICA. Community Members. One-to-one coupling of glacial climate variability in Greenland and Antarctica. *Nature* **444**, 195–198 (2006).
8. Parrenin, F. *et al.* Synchronous change of atmospheric CO_2 and Antarctic temperature during the last deglacial warming. *Science* **339**, 1060–1063 (2013).
9. Nicolas, J. P. & Bromwich, D. H. Climate of West Antarctica and influence of marine air intrusions. *J. Clim.* **24**, 49–67 (2011).
10. Noone, D. & Simmonds, I. Sea ice control of water isotope transport to Antarctica and implications for ice core interpretation. *J. Geophys. Res.* **109**, D07105 (2004).
11. Steig, E. J. *et al.* in *The West Antarctic Ice Sheet: Behavior and Environment* Vol. 77 (eds Alley, R. & Bindschadler, R.) 75–90 (American Geophysical Union, 2001).
12. Svensson, A. *et al.* A 60,000 year Greenland stratigraphic ice core chronology. *Clim. Past* **4**, 47–57 (2008).
13. Steig, E. J. *et al.* Recent climate and ice-sheet changes in West Antarctica compared with the past 2,000 years. *Nature Geosci.* **6**, 372–375 (2013).
14. Stenni, B. *et al.* Expression of the bipolar see-saw in Antarctic climate records during the last deglaciation. *Nature Geosci.* **4**, 46–49 (2011).
15. Hammer, C. U., Clausen, H. B. & Langway, C. C. 50,000 years of recorded global volcanism. *Clim. Change* **35**, 1–15 (1997).
16. Schwander, J. *et al.* A tentative chronology for the EPICA Dome Concordia ice core. *Geophys. Res. Lett.* **28**, 4243–4246 (2001).
17. Wolff, E. W., Rankin, A. M. & Rothlisberger, R. An ice core indicator of Antarctic sea ice production? *Geophys. Res. Lett.* **30**, 2158 (2003).
18. Holland, P. R. & Kwok, R. Wind-driven trends in Antarctic sea-ice drift. *Nature Geosci.* **5**, 872–875 (2012).
19. Anderson, R. F. *et al.* Wind-driven upwelling in the Southern Ocean and the deglacial rise in atmospheric CO_2. *Science* **323**, 1443–1448 (2009).
20. Monnin, E. *et al.* Atmospheric CO_2 concentrations over the last glacial termination. *Science* **291**, 112–114 (2001).
21. Toggweiler, J. R., Russell, J. L. & Carson, S. R. Midlatitude westerlies, atmospheric CO2, and climate change during the ice ages. *Paleoceanography* **21**, PA2005 (2006).
22. Lee, S. Y., Chiang, J. C. H., Matsumoto, K. & Tokos, K. S. Southern Ocean wind response to North Atlantic cooling and the rise in atmospheric CO_2: modeling perspective and paleoceanographic implications. *Paleoceanography* **26**, PA1214 (2011).
23. Collins, L. G., Pike, J., Allen, C. S. & Hodgson, D. A. High-resolution reconstruction of southwest Atlantic sea-ice and its role in the carbon cycle during marine isotope stages 3 and 2. *Paleoceanography* **27**, PA3217 (2012).
24. Roeckner, E. *et al. The Atmospheric General Circulation Model ECHAM-4: Model Description and Simulation of Present-Day Climate.* Report No. 218 90 (Max-Planck-Institut für Meteorologie, 1996).
25. Braconnot, P. *et al.* Results of PMIP2 coupled simulations of the Mid-Holocene and Last Glacial Maximum - Part 1: experiments and large-scale features. *Clim. Past* **3**, 261–277 (2007).
26. Huybers, P. Early Pleistocene glacial cycles and the integrated summer insolation forcing. *Science* **313**, 508–511 (2006).
27. Pedro, J. B. *et al.* The last deglaciation: timing the bipolar seesaw. *Clim. Past* **7**, 671–683 (2011).
28. Brook, E. J. *et al.* Timing of millennial-scale climate change at Siple Dome, West Antarctica, during the last glacial period. *Quat. Sci. Rev.* **24**, 1333–1343 (2005).
29. Blunier, T. & Brook, E. J. Timing of millennial-scale climate change in Antarctica and Greenland during the last glacial period. *Science* **291**, 109–112 (2001).
30. Petit, J. R. *et al.* Climate and atmospheric history of the past 420,000 years from the Vostok ice core, Antarctica. *Nature* **399**, 429–436 (1999).
31. Lemieux-Dudon, B. *et al.* Consistent dating for Antarctic and Greenland ice cores. *Quat. Sci. Rev.* **29**, 8–20 (2010).

39

WAIS Divide Project Members T. J. Fudge[1], Eric J. Steig[1,2], Bradley R. Markle[1], Spruce W. Schoenemann[1], Qinghua Ding[1,2], Kendrick C. Taylor[3], Joseph R. McConnell[3], Edward J. Brook[4], Todd Sowers[5], James W. C. White[6,7], Richard B. Alley[5,8], Hai Cheng[9,10], Gary D. Clow[11], Jihong Cole-Dai[12], Howard Conway[1], Kurt M. Cuffey[13], Jon S. Edwards[4], R. Lawrence Edwards[10], Ross Edwards[14], John M. Fegyveresi[5,8], David Ferris[12], Joan J. Fitzpatrick[15], Jay Johnson[16], Geoffrey Hargreaves[17], James E. Lee[4], Olivia J. Maselli[3], William Mason[18], Kenneth C. McGwire[3], Logan E. Mitchell[4], Nicolai Mortensen[16], Peter Neff[1,19], Anais J. Orsi[20], Trevor J. Popp[21], Andrew J. Schauer[1], Jeffrey P. Severinghaus[20], Michael Sigl[3], Matthew K. Spencer[22], Bruce H. Vaughn[7], Donald E. Voigt[5,8], Edwin D. Waddington[1], Xianfeng Wang[23] & Gifford J. Wong[24]

Affiliations for participants: [1]Department of Earth and Space Sciences, University of Washington, Seattle, Washington 98195, USA. [2]Quaternary Research Center, University of Washington, Seattle, Washington 98195, USA. [3]Desert Research Institute, Nevada System of Higher Education, Reno, Nevada 89512, USA. [4]College of Earth, Ocean and Atmospheric Sciences Oregon State University, Corvallis, Oregon 97331, USA. [5]Earth and Environmental Systems Institute, Pennsylvania State University, University Park, Pennsylvania 16802, USA. [6]Department of Geological Sciences and Department of Environmental Studies, Boulder, Colorado 80309, USA. [7]INSTAAR, University of Colorado, Boulder, Colorado 80309, USA. [8]Department of Geosciences, Pennsylvania State University, University Park, Pennsylvania 16802, USA. [9]Institute of Global Environmental Change, Xi'an Jiaotong University, Xi'an 710049, China. [10]Department of Earth Sciences, University of Minnesota, Minneapolis, Minnesota 55455, USA. [11]US Geological Survey, Geosciences and Environmental Change Science Center, Lakewood, Colorado 80225, USA. [12]Department of Chemistry and Biochemistry, South Dakota State University, Brookings, South Dakota 57007, USA. [13]Department of Geography, University of California-Berkeley, Berkeley 94720, USA. [14]Department of Imaging and Applied Physics, Curtin University, Perth, Western Australia 6102, Australia. [15]US Geological Survey, Denver, Colorado 80225, USA. [16]Ice Drilling Design and Operations, Space Science Engineering Center, University of Wisconsin-Madison, Madison, Wisconsin 53706, USA. [17]US Geologic Survey, National Ice Core Laboratory, Denver, Colorado 80225, USA. [18]EMECH Designs, Brooklyn, Wisconsin 53521, USA. [19]Antarctic Research Centre, Victoria University of Wellington, Wellington 6012, New Zealand. [20]Scripps Institution of Oceanography, University of California, San Diego, La Jolla, California 92037, USA. [21]Centre for Ice and Climate, Niels Bohr Institute, University of Copenhagen, Juliane Maries Vej 30, 2100 Copenhagen, Denmark. [22]Department of Geology and Physics, Lake Superior State University, Sault Ste Marie, Michigan 49783, USA. [23]Earth Observatory of Singapore, Nanyang Technological University, Singapore 639798. [24]Department of Earth Sciences, Dartmouth College, Hanover, New Hampshire 03755, USA.

40

METHODS

Stable-isotope measurements of ice. Water isotope analyses were by laser spectroscopy[32] at the University of Washington. Values of $\delta^{18}O$ represent the deviation from Vienna Standard Mean Ocean Water (VSMOW) normalized[11] to the VSMOW-SLAP standards and reported in per mil (‰). The precision of the measurements is better than 0.1‰. The data have not been corrected for advection, elevation, or mean seawater $\delta^{18}O$.

Accumulation rates. The accumulation-rate record was derived independently from the stable-isotope record using an ice-flow model to calculate the thinning function. We use a transient one-dimensional ice-flow model to compute the vertical-velocity profile:

$$w(z) = -\left(\dot{b} - \dot{m} - \dot{H}\right)\psi(z) - \dot{m} - \left(\frac{\rho_i}{\rho(z)} - 1\right)\dot{b} \quad (1)$$

Here z is the height above the bed, $\dot{b}$ is the accumulation rate, $\dot{m}$ is the melt rate, $\dot{H}$ is the rate of ice-thickness change, ρ_i is the density of ice, $\rho(z)$ is the density profile and $\psi(z)$ is the vertical velocity shape function computed as

$$\psi(z) = \frac{(f_B z + (1/2)(1 - f_B)(z^2/h))}{(H - (h/2)(1 - f_B))} \quad \text{for } h \geq z > 0$$

$$\psi(z) = \frac{(z - (h/2)(1 - f_B))}{(H - (h/2)(1 - f_B))} \quad \text{for } H \geq z > h$$

following ref. 33. Here h is the distance above bedrock of the Dansgaard–Johnsen[34] kink height, f_B is the fraction of the horizontal surface velocity due to sliding over the bed and H is the ice thickness. Firn compaction is incorporated through the rightmost term in equation (1) and assumes a density profile that does not vary with time.

A constant ice thickness was specified because the thickness change near the divide was probably small (~100 m) and the timing of thickening and thinning is not well constrained; a 100-m thickness change would alter the inferred accumulation rate by ~3%. A constant basal melt rate of 1 cm yr^{-1} and non-divide flow conditions, represented by a Dansgaard–Johnsen kink height of 0.2H, were assumed. We also prescribed a sliding fraction of 0.5 of the surface velocity, which approximates effects of both basal sliding and enhanced shear near the bed, neither of which is well constrained. To assess the possible range of inferred accumulation rates, we also used sliding fractions of 0.15 and 0.9 (Supplementary Fig. 2). The inferred accumulation rate was only slightly affected for the Holocene part of the record but differed by up to 16% for the oldest part of the record (29.6 kyr ago). Because the thinning function varies smoothly, the uncertainty in the timing of the changes in accumulation rate is only weakly affected by the uncertainty in the magnitude of the accumulation rate. The main uncertainty in identifying the timing of accumulation rate changes is the uncertainty in the timescale itself. During the deglacial transition, the uncertainty in the interpretation is estimated at 8%. The yellow shading in Fig. 3 shows this uncertainty.

WDC06A-7 timescale. The WDC06A-7 timescale is based on high-resolution (<1 cm) measurements of sulphur, sodium, black carbon and electrical conductivity (ECM) above 577 m (2,358 yr before present (BP; AD 1950); ref. 35). Below 577 m, WDC06A-7 is based primarily on electrical measurements: di-electrical profiling was used for the brittle ice from 577 to 1,300 m (to 6,063 yr BP). Alternating-current ECM measurements were used from 1,300 to 1,955 m (to 11,589 yr BP) and both alternating-current and direct-current ECM measurements were used below 1,955 m. The interpretation was stopped at 2,800 m because the expression of annual layers becomes less consistent, suggesting that all years may not be easily recognized.

The upper 577 m of the timescale has been compared with volcanic horizons dated on multiple other timescales[35]; the uncertainty at 2,358 yr BP is ±19 yr. For the remainder of the timescale, we assigned an uncertainty based on a qualitative assessment of the clarity of the annual layers. For ice from 577 to 2,020 m (2–12 kyr ago), we estimated a 2% uncertainty based on comparisons between the ECM and chemical (Na, SO$_4$) interpretations between 577 and 1,300 m, which agreed to within 1% (Supplementary Fig. 4). The estimated uncertainty increased during the deglacial transition owing to both thinner layers and a less pronounced seasonal cycle. We compared the annual-layer interpretation of the ECM records in an 800-yr overlap section (1,940–2,020-m depth, corresponding to 11.4–12.2 kyr ago) with various high-resolution chemistry records (sodium and sulphur). We found overall good agreement (19 yr more in the ECM-only interpretation) but did observe a tendency for the ECM record to 'split' one annual peak into two small peaks. We used this knowledge in the annual-layer interpretation of the ECM record. We increased the uncertainty to 4% between 2,020 and 2,300 m (12.2–15.5 kyr ago) and to 8% between 2,300 and 2,500 m (15.5–20 kyr ago). The glacial period had a stronger annual-layer signal than the transition, and we estimate a 6%

uncertainty for the rest of the glacial. The 150-yr acid deposition event, first identified in the Byrd ice core[15], was found in WDC at depths of 2,421.75 to 2,427.25 m. Because there is consistently high conductance without a clear annual signal, we used the average annual layer thickness of the 10 m above and below this section to determine the number of years within it. There are periods of detectable annual variations within this depth range, and they have approximately the same annual-layer thickness as the 10-m averages. A 10% uncertainty was assumed.

We assess the accuracy of WDC06A-7 by comparing it with two high-precision timescales: GICC05 and a new speleothem timescale from Hulu Cave. Because the age of the gas at a given depth is less than that of the ice surrounding it, we first need to calculate the age offset (Δage). We use the inferred accumulation rates and surface temperatures estimated from the $\delta^{18}O$ record constrained by the borehole temperature profile (Supplementary Information) in a steady-state firn-densification model[36]. The model is well-suited to WDC because it was developed using data from modern ice-core sites that span the full range of past WDC temperatures and accumulation rates. We calculate Δage using 200-yr smoothed histories of surface temperature and accumulation rate, a surface density of 370 kg m^{-3} and a close-off density of 810 kg m^{-3} (Supplementary Fig. 5a). The calculated present-day Δage is 210 yr, which is similar to the value, 205 yr, measured for WDC[37]. The steady-state model is acceptable for WDC because the surface temperature and accumulation rate vary more slowly than in Greenland. Because our primary purpose is to assess the accuracy of the WDC06A-7 timescale, calculation of Δage to better than a few decades is not necessary. The Δage uncertainty between 15 and 11 kyr ago is estimated to be 100 yr. The Δage uncertainty is estimated to be 150 yr for times before 20 kyr ago because of the colder temperatures and lower and less certain accumulation rates.

Because methane is well mixed in the atmosphere and should have identical features in both hemispheres, we use atmospheric methane measurements from WDC and the Greenland composite methane record[33] to compare WDC06A-7 and GICC05 at six times. The age differences are summarized in Supplementary Fig. 6 and the correlation and Δage uncertainties are shown in Supplementary Table 1. In Greenland, methane and $\delta^{18}O$ changes are nearly synchronous[38–40] and we therefore assume no Δage uncertainty in the Greenland gas timescale at times of abrupt change. An exception is at 24 kyr ago (Dansgaard–Oeschger event 2), when methane and $\delta^{18}O$ changes do not seem to be synchronous. We estimate the correlation uncertainty from the agreement of the methane records in Supplementary Fig. 5.

Speleothems can be radiometrically dated with U/Th and have smaller absolute age uncertainties than do annually resolved timescales in the glacial period[37]. Records of speleothem $\delta^{18}O$ show many abrupt changes that have been tied to the Greenland climate record[41,42]. However, the physical link between $\delta^{18}O$ variations in the caves and methane variations is not fully understood. Therefore, there is an additional and unknown correlation uncertainty in these comparisons. We compare WDC06A-7 with the new record from Hulu Cave, China, which is the best-dated speleothem record during this time interval. Comparisons can be made at only three times; our best estimate of the age differences is 100 yr or less.

The EDC timescale can be compared with the WDC06A-7 at a ~150-yr-long acid deposition event[15,16]. The two timescales agree within 100 yr, and we therefore do not adjust either timescale. The EDML timescale has been synchronized with the EDC timescale using sulphate matches[43]. The sulphate match that occurs during the 150-yr acid deposition event is marked in Fig. 2.

Sea-salt sodium measurements. Sea-salt sodium (ssNa) is the amount of Na that is of marine origin. The Na record was measured at the Trace Chemistry Laboratory at the Desert Research Institute. Na is one of many elements measured on the continuous-flow analysis system, which is coupled to two inductively coupled plasma mass spectrometers. The effective sampling resolution is ~1 cm. Details of the analytical set-up are described elsewhere[35,44–47]. Sea-salt Na is calculated assuming Na/Ca mass ratios of 26.3 for marine aerosols and 0.562 for average crust composition[48]. Sea-salt Na can be influenced by volcanic activity if the ratio of Na to Ca is different from the sea water and crustal ratios; the spike 20 kyr ago is part of an Na-rich but Ca-poor volcanic event. We present ssNa concentration in the main text instead of ssNa flux because wet deposition dominates at higher accumulation rates[49]. For comparison, the ssNa flux is shown in Supplementary Fig. 7.

Methane measurements. The methane concentration was measured in discrete samples at Oregon State University (OSU) and Pennsylvania State University (PSU) using automated melt–refreeze extraction and gas chromatography, with final concentration values reported on the NOAA04 concentration scale[50]. OSU data are corrected for gravitational fractionation, solubility and blanks as described in ref. 37. The gravitation fractionation correction assumes that $\delta^{15}N$ of N_2 is 0.3‰, a value based on late-Holocene measurements.

PSU methods were modelled on the basis of the OSU melt–refreeze system. The major difference between the OSU and PSU methods is the extraction cylinders; glass at OSU and stainless steel at PSU. Using stainless steel cylinders carries the

added problem of a blank associated with CH_4 outgassing, which we have estimated to be 19 ± 8 p.p.b. We have used a calculation similar to that derived in ref. 37, to estimate the amount of CH_4 left in the vessel after refreezing; we verified this using artificially degassed ice samples over which standard air was introduced and processed. These results indicate a 3.8% reduction in the measured headspace CH_4 value relative to the original trapped air, owing to solubility effects. The constant solubility and blank corrections were applied to all PSU data. In general, replicate samples from each depth were run on separate days to ensure that the final averaged data were not aliased by day-to-day instrument drifts. The average difference between replicate analyses of 1,316 individual depths run over 4 yr was 7 ± 8 p.p.b. (1σ). Finally, the PSU data were also corrected for gravitational fractionation by assuming that $\delta^{15}N$ of N_2 is 0.3‰ throughout.

To ensure that the PSU and OSU CH_4 data sets can be accurately merged into a single record, we performed an inter-calibration exercise involving a 100-m section of the WDC06A core (400–500 m) where both labs sampled for CH_4 every 2 m. By interpolating the OSU data to compare with the PSU data, we determined the average difference between the two labs over this 100 m interval to be 0.2 ± 9.9 p.p.b. (1σ). This result implies that we can merge CH_4 data from the two labs without correcting for inter-laboratory offsets.

Wilcoxon rank-sum test. Initial inspection of the WDC isotope record showed that warming was pulsed. We applied a sliding Wilcoxon rank-sum statistical test[51] to identify periods of significant change. A figure of the P values, for each individual Wilcoxon rank-sum test, is shown in Supplementary Fig. 8. A dashed line indicates the effective critical P value. Insignificant P values are plotted in grey, and significant P values are plotted in colours that correspond to timespan (block size) as in Fig. 2. The Wilcoxon rank-sum test makes no assumption of normality within the data and has been shown to be robust when used in windowing algorithms for the identification of periods of significant change in climate data[52]. Our windowing algorithm can also be applied using the more common Student's t-test. Though parametric, such an implementation has the benefit of a well-established method for correcting the degrees of freedom for autocorrelation within the data[53]. Applying either statistical test, we identify nearly identical periods of significant change in the data sets.

Climate modelling. To assess the effects of changing sea-ice conditions on precipitation-weighted $\delta^{18}O$ in Antarctica, we used the ECHAM4.6 climate model[24], implemented with the water isotope module[54]. Model simulations used a horizontal resolution of T42 ($2.8°$ latitude by $2.8°$ longitude) with 19 vertical levels. The ECHAM4.6 model has been shown to reproduce Antarctic conditions realistically in the modern climate[13,55]. We used the sea surface temperatures from the PMIP2 fully coupled model experiments[25] for LGM conditions ~ 21 kyr ago. Those sea surface temperatures are prescribed as a model boundary condition for the atmospheric model runs with ECHAM4.6. We used a modern Antarctic ice-sheet configuration because the LGM configuration remains poorly known.

Model experiments were designed to test the sensitivity of $\delta^{18}O$ to changes in sea-ice extent. In the control experiment, sea ice forms at $-1.7\ °C$ and the model grid cell is set to 100% concentration below this threshold. The latitude of sea-ice coverage is decreased by lowering the ocean surface temperature threshold at which sea ice forms in the model. For the run with decreased sea ice, the freezing point was lowered from -1.7 to $-3.7\ °C$. The amount of sea-ice reduction is not zonally uniform around Antarctica because of asymmetric gradients in the prescribed sea surface temperature. We note that model sea surface temperatures do not change whether model sea ice is present or not. Newly formed open water in the run with reduced sea ice is below the freezing point.

Integrated insolation. We calculate integrated annual insolation at latitude $65°$ S following the tables prepared in ref. 26. We also calculate integrated 'summer' and 'winter' insolation using a cut-off of $275\ \mathrm{W\ m^{-2}}$ (ref. 26; Supplementary Fig. 10).

32. Crosson, E. R. A cavity ring-down analyzer for measuring atmospheric levels of methane, carbon dioxide, and water vapor. *Appl. Phys. B* **92,** 403–408 (2008).
33. Dahl-Jensen, D., Gundestrup, N., Gogineni, S. P. & Miller, H. Basal melt at NorthGRIP modeled from borehole, ice-core and radio-echo sounder observations. *Ann. Glaciol.* **37,** 207–212 (2003).
34. Dansgaard, W. & Johnsen, S. J. A flow model and a time scale for the ice core from Camp Century, Greenland. *J. Glaciol.* **8,** 215–223 (1969).
35. Sigl, M. *et al.* A new bipolar ice core record of volcanism from WAIS Divide and NEEM and implications for climate forcing of the last 2000 years. *J. Geophys. Res.* **18,** 1151–1169 (2013).
36. Herron, M. M. & Langway, C. C. Firn densification: an empirical model. *J. Glaciol.* **25,** 373–385 (1980).
37. Mitchell, L. E., Brook, E. J., Sowers, T., McConnell, J. R. & Taylor, K. Multidecadal variability of atmospheric methane, 1000-1800 CE. *J. Geophys. Res.* **116,** G02007 (2011).
38. Huber, C. *et al.* Evidence for molecular size dependent gas fractionation in firn air derived from noble gases, oxygen, and nitrogen measurements. *Earth Planet. Sci. Lett.* **243,** 61–73 (2006).
39. Kobashi, T., Severinghaus, J. P., Brook, E. J., Barnola, J. M. & Grachev, A. M. Precise timing and characterization of abrupt climate change 8200 years ago from air trapped in polar ice. *Quat. Sci. Rev.* **26,** 1212–1222 (2007).
40. Severinghaus, J. P., Sowers, T., Brook, E. J., Alley, R. B. & Bender, M. L. Timing of abrupt climate change at the end of the Younger Dryas interval from thermally fractionated gases in polar ice. *Nature* **391,** 141–146 (1998).
41. Fleitmann, D. *et al.* Timing and climatic impact of Greenland interstadials recorded in stalagmites from northern Turkey. *Geophys. Res. Lett.* **36,** L19707 (2009).
42. Cheng, H. *et al.* Ice age terminations. *Science* **326,** 248–252 (2009).
43. Ruth, U. *et al.* "EDML1": a chronology for the EPICA deep ice core from Dronning Maud Land, Antarctica, over the last 150,000 years. *Clim. Past* **3,** 475–484 (2007).
44. Bisiaux, M. M. *et al.* Changes in black carbon deposition to Antarctica from two high-resolution ice core records, 1850-2000 AD. *Atmos. Chem. Phys.* **12,** 4107–4115 (2012).
45. McConnell, J. R. Continuous ice-core chemical analyses using inductively coupled plasma mass spectrometry. *Environ. Sci. Technol.* **36,** 7–11 (2002).
46. McConnell, J. R. *et al.* 20th-century industrial black carbon emissions altered arctic climate forcing. *Science* **317,** 1381–1384 (2007).
47. Pasteris, D. R., McConnell, J. R. & Edwards, R. High-resolution, continuous method for measurement of acidity in ice cores. *Environ. Sci. Technol.* **46,** 1659–1666 (2012).
48. Röthlisberger, R., Crosta, X., Abram, N. J., Armand, L. & Wolff, E. W. Potential and limitations of marine and ice core sea ice proxies: an example from the Indian Ocean sector. *Quat. Sci. Rev.* **29,** 296–302 (2010).
49. Alley, R. B. *et al.* Changes in continental and sea-salt atmospheric loadings in central Greenland during the most recent deglaciation: model-based estimates. *J. Glaciol.* **41,** 503–514 (1995).
50. Dlugokencky, E. J. *et al.* Conversion of NOAA atmospheric dry air CH_4 mole fractions to a gravimetrically prepared standard scale. *J. Geophys. Res.* **110,** D18306 (2005).
51. Wilcoxon, F. Individual comparisons by ranking methods. *Biom. Bull.* **1,** 80–83 (1945).
52. Mauget, S. A. Intra- to multidecadal climate variability over the continental United States: 1932-99. *J. Clim.* **16,** 2215–2231 (2003).
53. Bretherton, C. S., Widmann, M., Dymnikov, V. P., Wallace, J. M. & Blade, I. The effective number of spatial degrees of freedom of a time-varying field. *J. Clim.* **12,** 1990–2009 (1999).
54. Hoffmann, G., Werner, M. & Heimann, M. Water isotope module of the ECHAM atmospheric general circulation model: a study on timescales from days to several years. *J. Geophys. Res.* **103,** 16871–16896 (1998).
55. Ding, Q. H., Steig, E. J., Battisti, D. S. & Kuttel, M. Winter warming in West Antarctica caused by central tropical Pacific warming. *Nature Geosci.* **4,** 398–403 (2011).

Chapter 5: Supplement to: *Onset of deglacial warming in central West Antarctica driven by local orbital forcing*

Originally published in Nature

This supplement was published in Nature. It provides many details that could not be included in the main paper. A feature of particular interest is the rapid accumulation increase of 40% between 12 and 11.6 ka. An accumulation rate increase of this rapidity was not expected in Antarctica and it will be interesting to explore the cause of this event in future work.

See the explanation in Chapter 4 of my contribution.

Contents

1. Modern climate and glaciological setting

The WAIS Divide ice core (WDC) was drilled at 79° 28.058' S, 112° 05.189' W, ~160 km east from the Byrd ice-core drilling site and ~24 km towards the Ross Sea from the current Ross-Amundsen ice-flow divide (Figure S1). The elevation is 1766 meters above sea level, average annual ice accumulation[1] is ~0.22 m, ice thickness is 3455 m, and the average annual surface temperature[2] is –30°C. The modern climate conditions are similar to those in central Greenland. Compared with the interior of East Antarctica, central West Antarctica is strongly influenced by intrusions of marine air[3]. There is a strong gradient in accumulation across the ice divide, with higher accumulation towards the Amundsen Sea and lower accumulation towards the Ross Sea[4,5]. This reflects the prevailing pattern of cyclonic activity over the Amundsen Sea[3]. There is no apparent climate divide corresponding to the physical ice divide[4,6], so variations in the location of the ice divide through time should not significantly influence the climate at WDC.

Measurements of oxygen stable-isotope ratios ($\delta^{18}O$) in multiple firn and ice cores from across West Antarctica show that WDC is well-situated to represent West Antarctic climate conditions as a whole; interannual $\delta^{18}O$ variations in ice cores west and east of the ice divide are most highly correlated with other cores from their respective regions, while $\delta^{18}O$ at WDC is equally well correlated with cores from both regions[6]. Annual isotope variations at WDC are significantly correlated (r=0.44; p=0.004) with local mean annual temperature, and decadal-scale trends show the same $\delta^{18}O$-temperature scaling[7]. Comparison with borehole temperature data[2,7] and independent estimates from bubble-number densities[8] further support the interpretation of low frequency $\delta^{18}O$ variations as a measure of temperature. Investigation of the seasonal $\delta^{18}O$ variations in the nearby ITASE 2000-01 ice core and other cores from West Antarctica show that sea-ice variations over the Amundsen Sea contribute significantly to $\delta^{18}O$ variability[6], consistent with the prevailing wind pattern and the strong marine influence at this site[3].

2. Non-climate effects on the δ^{18}O record

2a. Ice Sheet Elevation Change

The site for WDC was selected near the ice-flow divide to minimize the influence of ice-sheet elevation change on the climate record; interior locations experience smaller ice thickness changes than coastal locations[9,10]. The best evidence for ice-sheet elevation change in the interior of the West Antarctic ice sheet comes from the Ohio Range, to the south of the WDC site at 1600 m elevation, and from Mt. Waesche to the north at 2000 m elevation[9,11,12]. Moraines at Mt. Waesche were ~50 m higher and trimlines in the Ohio Range were ~125 m higher, between 12 and 10 ka. The ~100 m of thinning throughout the Holocene occurred as the grounding line retreated by hundreds of km[13,14] and the accumulation rates were relatively stable. The elevation changes are much smaller than early model estimates[15,16] and comparable to the amount of elevation change inferred for interior East Antarctic sites[17].

While there are no direct constraints on elevation changes prior to ~12 ka, the ice sheet either had to be at its high stand during the last glacial maximum or thicken in response to increasing accumulation rates during the deglaciation[11,12]. A thinner ice sheet in the interior during the Last Glacial Maximum (LGM) is difficult to reconcile with the large advance in the grounding line position. Numerical modeling of the WAIS suggests little ice-thickness change in the interior[18,19].

Rapid changes in δ^{18}O are particularly unlikely to have been caused by changes in ice sheet elevation. For instance, the 1.5‰ increase in δ^{18}O between 20 and 18.8 ka would require >150 m of thinning in only 1200 years. This is a rate of ~0.12 m a^{-1}. In comparison, the accumulation rate at the time was ~0.1 m a^{-1} and had been reasonably constant for thousands of years (Figure S2). A rapid thinning of the ice sheet at the divide is also unlikely because of the long distance that perturbations at the grounding line need to propagate inland. There is also no evidence of large grounding line retreat at the LGM. Rates of thinning in response a retreat of the grounding line are highest near the coast and decrease inland[9-11].

2b. Ice Advection

The modern divide is 1‰ enriched in δ^{18}O relative to the ice-core site[6]. The divide position likely varied through time because no Raymond bump is observed in the internal radar stratigraphy[4] and it is currently migrating[20]. Using the modern horizontal ice flow velocity[20] of 3 m a^{-1} at the core site and the modern isotope gradient (~0.005‰/km), we estimate the effect of ice advection to be ~0.15‰ per 1000 years over the last one to two thousand years. This rate was likely smaller in the past because the ice would have been closer to the divide where the ice velocity is lower. The ice-flow velocity was also likely smaller in the glacial period when accumulation rates were lower. While ice advection is unlikely to substantially affect the glacial-interglacial changes, the advection effect may be important during periods of relatively stable isotopic values, such as the Holocene.

3. Ice and heat flow modeling

Although a full analysis of past surface temperature and accumulation rate is beyond the scope of this Letter, we make quantitative estimates of both to calculate the gas-age ice-age difference (Δage) and compare the accuracy of the annually resolved portion of the WDC06A-7 timescale

to Greenland and speleothem timescales. Two features unique to WDC among Antarctic ice cores allow our temperature and accumulation histories to have good accuracy:

1) The magnitude of the glacial-interglacial temperature change is preserved in the borehole temperature profile, allowing a first-order calibration of the isotope-temperature relationship.
2) The annually-resolved timescale can be used to directly infer the accumulation rate without assuming a particular relationship with temperature.

We use a transient one-dimensional ice-flow model to compute the vertical-velocity profile:

$$w(z) = -\left(\dot{b} - \dot{m} - \dot{H}\right)\psi(z) - \dot{m} - \left(\frac{\rho_i}{\rho(z)} - 1\right)\dot{b} \qquad (1)$$

where z is the height above the bed, $\dot{b}$ is the accumulation rate, $\dot{m}$ is the melt rate, $\dot{H}$ is the rate of ice-thickness change, ρ_i is the density of ice, $\rho(z)$ is the density profile and $\Psi(z)$ is the vertical velocity shape function computed as:

$$\psi(z) = \left(f_B z + \frac{1}{2}(1 - f_B)\frac{z^2}{h}\right) / \left(H - \frac{1}{2}h(1 - f_B)\right) \quad \text{for } h \geq z > 0 \qquad (2a)$$

$$\psi(z) = \left(z - \frac{1}{2}h(1 - f_B)\right) / \left(H - \frac{1}{2}h(1 - f_B)\right) \quad \text{for } H \geq z > h \qquad (2b)$$

following Dahl-Jensen et al.[21] where h is the distance above bedrock of the Dansgaard-Johnsen[22] kink height, f_B is the fraction of the horizontal surface velocity due to sliding over the bed, and H is the ice thickness. Firn compaction is incorporated through the right hand term in equation 1 and assumes a density profile that does not vary with time.

The heat equation following Cuffey and Paterson[23] is:

$$\rho c_p \frac{\partial T}{\partial t} = \frac{\partial}{\partial z}\left(k\frac{\partial T}{\partial z}\right) - \rho c_p w \frac{\partial T}{\partial z} + Q \qquad (3)$$

where c_p is the heat capacity, T is temperature, k is the thermal conductivity, and Q is the heat production term. The firn density profile is modeled using the Herron and Langway[27] model matched to modern measurements[28] to assure a smooth vertical velocity profile. Values of c_p and k are calculated at each time step following standard relationships in Cuffey and Paterson[23].

The ice-flow and heat-flow models are not explicitly coupled; the ice-flow model is used to calculate the vertical velocity for the heat-flow model but the temperature profile is not incorporated in the calculation of the vertical velocity. The ice thickness was held constant. The basal melt rate is prescribed and does not vary in time; the ice/bed interface is always at the melting point. Any water produced by melt at the bed is assumed to drain away instantaneously.

3a. Basal Melt Rate
The first indication of a high basal melt rate at WDC was the young ice at depth and the correspondingly thick (~1cm) annual layers. Similar to the situation at North GRIP[21], the basal melting reduces the vertical strain of layers as ice is removed through melting rather than horizontal shear. The melting also steepens the basal temperature gradient as the colder ice near

46

the surface is advected towards the bed more quickly. The borehole temperature gradient, measured in December 2011, allows an estimate of basal melting. Rearranging equation 3 to solve for w:

$$w = \left[\kappa \left(\frac{\partial T^2}{\partial z^2} \right) - b\kappa \left(\frac{\partial T}{\partial z} \right)^2 - \frac{\partial T}{\partial t} + \frac{1}{\rho C_p} Q \right] / \frac{\partial T}{\partial z} \qquad (4)$$

where κ is the thermal diffusivity and b is an exponent that relates the thermal conductivity to temperature[23]. We evaluate these terms at 3300 m. The first two terms in the brackets can be measured from the borehole temperature profile: $\partial T/\partial z$ is 34.8×10^{-3} K^{-1}m and $\partial^2 T/\partial z^2$ is 0.029×10^{-3} K^{-1}m^2. A model must be used to estimate the second two terms; both are small compared to the first two terms. At 3300 m depth, the vertical velocity is 2.1 cm a^{-1}. It is unlikely this large of a vertical flux can be removed through horizontal shear in the remaining ~160 m of the ice column, and we therefore conclude that the basal melt rate is likely between 0.7 and 1.5 cm a^{-1}.

3b. Accumulation Rates

The accumulation rate is calculated from the depth-age relationship using the ice-flow model described above. A constant ice thickness was specified because the thickness change near the divide was probably small (~100 m) and the timing of thickening and thinning is not well constrained; a 100 m thickness change would alter the inferred accumulation rate by ~3%. A constant basal melt rate of 1 cm a^{-1} and non-divide flow conditions, represented by a Dansgaard-Johnsen kink height of 0.2H, are assumed. We also prescribe a sliding fraction of 0.5 of the surface velocity, which approximates effects of both basal sliding and enhanced shear near the bed, neither of which are well constrained. To assess the possible range of inferred accumulation rates, we also use sliding fractions of 0.15 and 0.9 (Figure S2). The inferred accumulation rate is only slightly affected for the Holocene part of the record but is up to 16% different for the oldest part of the record (29.6 ka). Because the thinning function varies smoothly, the uncertainty in the timing of the changes in the accumulation rate is only weakly affected by the uncertainty in the magnitude of the accumulation rate. The main uncertainty in identifying the timing of accumulation rate changes is the uncertainty in the timescale itself. During the deglacial transition, the uncertainty in the interpretation is estimated at 8% (section 4b). The yellow shading in Figure 3 of the main text shows this uncertainty.

The inferred accumulation rate is an "ice-core accumulation rate" rather than a "climate accumulation rate." Because ice at depth originated upstream from the core site, the annual layer thicknesses record both temporal and spatial gradients in the accumulation rate. The current divide receives approximately 30% more accumulation than the ice core site[5]. Assuming that the accumulation gradient was similar in the past, this results in a gradient of 1.3% per km. Modern ice-flow velocities at the ice-core site are ~3 m a^{-1} and were likely lower in the past. Therefore, accumulation changes from ice-advection may amount to ~2% per 1000 years. However, the effect is cumulative so the snow that fell at the LGM could have been at a location, such as the modern divide, that received ~30% more accumulation than the core site without any change in climate.

We do not develop an accumulation rate derived from the temperature estimated from δ^{18}O. The relationship between stable isotopes and accumulation rate in West Antarctica does not follow a

simple relationship that would justify such a calculation. For instance, in the modern climate Byrd is 2‰ lighter in $\delta^{18}O$ than WAIS Divide but receives 40% less accumulation. While the accumulation record from WDC does show a general correspondence to $\delta^{18}O$ and thus local temperature at orbital timescales, there are significant differences between the isotope and accumulation records. Foremost is the abrupt accumulation increase of 37±10% between 12.0 and 11.6 ka during the double isotope peak of Antarctic Isotope Maximum (AIM) 0 (Figure S2). The uncertainty bounds are the additive effects of possible ice-thickness change (3%), ice advection through an accumulation gradient (3%), and annual-layer interpretation (4%). Abrupt changes in accumulation cannot be recognized in other Antarctic cores because their timescales lack sufficient resolution. The timing of the abrupt accumulation increase is coincident within uncertainty with a minimum in dust concentration at three sites on the East Antarctic plateau[24] (EDC, Dome B, Komosmolskaia) raising the possibility that the atmospheric circulation changed during this period across much of Antarctica.

3c. Surface temperature:
The surface temperature history is derived as a linear function of the $\delta^{18}O$ record, with calibration coefficients determined by optimizing the match between model and measured borehole temperature profiles. For a range of ice-dynamical scenarios, results suggest that the Last Glacial Maximum was 7 to 9 °C colder than present. Work on this topic is in progress and full results and analyses will be reported in a future publication. Figure S3 illustrates results for simplified scenarios with a range of temperature-change magnitudes.

4. Sea-salt sodium
The concentration of sea-salt Sodium (ssNa) in surface snow decreases with distance from the ocean and elevation above sea level[25]. However, concentrations also vary regionally indicating the importance of both the source region and the intensity of transport on the ssNa concentration at a specific location[26]. While ssNa is clearly a proxy for oceanic and atmospheric conditions, it is debated whether ssNa is a better indicator of sea-ice production or atmospheric circulation. Increasing ssNa concentrations at Siple Dome throughout the Holocene have been interpreted to indicate increasing incursions of marine air as the grounding line of the Ross ice sheet retreated[27]. The large Holocene increase at Siple Dome (modern levels are higher than glacial levels) is unique among long ice-core records (WDC, EDC[28,29], EDML[30], and Taylor Dome[27]); however, the glacial record is quite similar to that at WDC, with a large decrease during the deglaciation.

Different interpretations of ssNa may be due to both different locations of ice cores and different timescales of analysis. The use of ssNa as a sea-ice proxy has focused on interior ice-core sites at multi-millenial timescales; the use of ssNa as an atmospheric-circulation proxy has focused on coastal ice-core sites at annual to decadal timescales. At the centennial to millennial timescales we are investigating at WDC, we favor the interpretation of ssNa as a sea-ice proxy[29,31]. The large decrease in ssNa during the deglaciation is difficult to explain on the basis of decreased strength of atmospheric circulation; model results do not support a large change in wind strength[32] and instead predict decreased ssNa deposition at the LGM due to the increased distance to open water[33]. Atmospheric circulation undoubtedly is also important. In fact, sea ice and atmospheric circulation are strongly correlated in the modern climate of the Ross and

Amundsen Seas[34]. Because of the uncertainties in ssNa as a sea-ice proxy, we do not attempt a detailed sea-ice reconstruction. The strong relationship with $\delta^{18}O$ at times of abrupt change may indicate significant sea-ice decreases, changes in atmospheric circulation and transport, or both.

5. Climate Modeling

To assess the effects of changing sea-ice conditions on the $\delta^{18}O$ of Antarctica, we used the ECHAM 4.6 climate model[35], implemented with the water isotope module[36]. Model simulations used a horizontal resolution of T42 (2.8° latitude by 2.8° longitude) with 19 vertical levels. The ECHAM 4.6 model has been shown to realistically reproduce variability in Antarctic climate and water isotope ratios in precipitation given observed sea surface temperature boundary conditions[7,37]. In this paper, we use sea surface temperatures from the PMIP2 fully-coupled model experiments[38] for LGM ~21 ka conditions. Those sea surface temperatures are prescribed as a model boundary condition for the atmospheric model runs with ECHAM4.6. We used a modern Antarctic Ice Sheet configuration because the LGM configuration remains poorly known; for example, the ICE-5g reconstruction[39] has greatly increased elevations at interior locations in West Antarctica that exceed estimates from geological observations and recent modeling work[40]. Using the modern topography underestimates the ice sheet elevation in the Ross Sea sector but, the effect of a thinner Ross Ice Sheet on WDC is relatively small because the precipitation received at WDC is predominantly from the Amundsen Sea[3].

Model experiments were designed to test the sensitivity of $\delta^{18}O$ to changes in the sea-ice extent. In the control experiment, sea ice forms at –1.7 °C and the model grid cell is set to 100% concentration below this threshold. The latitude of sea ice coverage is decreased by lowering the ocean surface temperature threshold at which sea ice forms in the model. For the decreased sea ice run, the freezing point was artificially lowered from -1.7 °C to -3.7 °C. The amount of sea ice reduction is not zonally uniform around Antarctica because of asymmetric gradients in the prescribed sea surface temperature (SST). It is important to note that model SSTs do not change whether model sea ice is present or not; newly formed open water in the reduced sea-ice run is below the freezing point. We have refrained from modeling the change in sea ice due to orbital forcing because of the known limitations in modeling sea ice correctly. Roche et al.[41] show that different models simulate very different amounts of sea-ice for both the modern and LGM conditions. Furthermore, they show that the amplitude of the seasonal cycle of sea-ice growth for the LGM is underestimated by all models.

The difference between 30-year integrations of the control run and the sea-ice reduction run are shown in Figure 4. In West Antarctica, the $\delta^{18}O$ is enriched across the entire ice sheet. In East Antarctica, there is a sharp contrast between the enriched $\delta^{18}O$ along the coast and unchanged or depleted $\delta^{18}O$ in the interior. The deep ice core positions are also shown in Figure 4. WDC is located in the enriched $\delta^{18}O$ signal initiating from the Amundsen Sea region, just as expected from the modern trajectory of marine air masses into West Antarctica[3].

The magnitude of the $\delta^{18}O$ anomalies in East Antarctica vary inversely with measures of a site's isolation from marine influence, such as elevation and distance from the coast. Most of the East Antarctic core sites are located in the strong gradient between positive coastal anomalies and zero or negative interior anomalies. The inland extent of the positive anomalies depends on the

horizontal resolution in the model, which smoothes the steep coastal topography. The anomalies at any given position are also model dependent, but higher-resolution (T106) model experiments show that the pattern of coastal enrichment and little interior change is robust. Law Dome is the lone East Antarctic core not in the interior and seemingly well-positioned to record coastal changes; however the accumulation rate during the LGM was inferred to be less than 10% of the modern value[42]. This suggests that the climate during the LGM was more similar to the East Antarctic plateau than to the current maritime climate[42]. Like Siple Dome, Law Dome highlights the difficulties associated with interpreting the climate records of coastal domes.

6. Insolation

Figure 3 shows integrated annual insolation as calculated by Huybers[43]. Figure S10 shows the integrated insolation on "summer" and "winter" days, as defined by a threshold of 275 W m^{-2} of insolation following Huybers[43]. At ~28 ka, the integrated annual insolation begins increasing as the integrated summer insolation increases and integrated winter insolation decreases. Therefore, not only is integrated annual insolation increasing, it is increasing more in the summer when there is the greatest potential to warm the ocean and melt sea ice because of the lower albedo. The increase in integrated summer insolation is related to the increasing summer duration as discussed by Huybers and Denton[44]. They primarily discuss the impact of the lengthening summer on radiative equilibrium, which is a mechanism for increasing surface temperature, but note that sea ice may be affected as well. Future work is needed to determine what forcing sea ice is most sensitive too, but both integrated summer insolation and summer duration show that local forcing were increasing significantly at the onset of warming at WDC.

References

1   Banta, J. R., McConnell, J. R., Frey, M. M., Bales, R. C. & Taylor, K. Spatial and temporal variability in snow accumulation at the West Antarctic Ice Sheet Divide over recent centuries. *Journal of Geophysical Research-Atmospheres* **113**, doi:D23102 (2008).

2   Orsi, A. J., Cornuelle, B. D. & Severinghaus, J. P. Little Ice Age cold interval in West Antarctica: Evidence from borehole temperature at the West Antarctic Ice Sheet (WAIS) Divide. *Geophysical Research Letters* **39**, doi:10.1029/2012gl051260 (2012).

3   Nicolas, J. P. & Bromwich, D. H. Climate of West Antarctica and Influence of Marine Air Intrusions. *Journal of Climate* **24**, 49-67, doi:10.1175/2010jcli3522.1 (2011).

4   Neumann, T. A. *et al.* Holocene accumulation and ice sheet dynamics in central West Antarctica. *Journal of Geophysical Research-Earth Surface* **113**, doi:F02018 (2008).

5   Morse, D. L., Blankenship, D. D., Waddington, E. D. & Neumann, T. A. A site for deep ice coring in West Antarctica: results from aerogeophysical surveys and thermo-kinematic modeling. *Annals of Glaciology, Vol 35* **35**, 36-44, doi:10.3189/172756402781816636 (2002).

6   Küttel, M., Steig, E. J., Ding, Q. H., Monaghan, A. J. & Battisti, D. S. Seasonal climate information preserved in West Antarctic ice core water isotopes: relationships to temperature, large-scale circulation, and sea ice. *Climate Dynamics* **39**, 1841-1857, doi:10.1007/s00382-012-1460-7 (2012).

7   Steig, E. J. *et al.* Recent climate and ice-sheet changes in West Antarctica compared with the past 2,000 years. *Nature Geoscience* **6**, 372-375, doi: 10.1038/NGEO1778 (2013).

8   Fegyveresi, J. M. *et al.* Late-Holocene climate evolution at the WAIS Divide site, West Antarctica: bubble number-density estimates. *Journal of Glaciology* **57**, 629-638 (2011).

50

9   Ackert, R. P., Mukhopadhyay, S., Parizek, B. R. & Borns, H. W. Ice elevation near the West Antarctic Ice Sheet divide during the Last Glaciation. *Geophysical Research Letters* **34**, 6, doi:L21506 10.1029/2007gl031412 (2007).

10   Stone, J. O. *et al.* Holocene deglaciation of Marie Byrd Land, West Antarctica. *Science* **299**, 99-102 (2003).

11   Ackert, R. P. *et al.* Measurements of past ice sheet elevations in interior West Antarctica. *Science* **286**, 276-280, doi:10.1126/science.286.5438.276 (1999).

12   Steig, E. J. *et al.* in *R. Alley and R. Bindschadler* Vol. **77** (ed The West Antarctic Ice Sheet: Behavior and Environment) 75-90 (Antarctic Research Series, 2001).

13   Anderson, J. B., Shipp, S. S., Lowe, A. L., Wellner, J. S. & Mosola, A. B. The Antarctic Ice Sheet during the Last Glacial Maximum and its subsequent retreat history: a review. *Quaternary Science Reviews* **21**, 49-70, doi:10.1016/s0277-3791(01)00083-x (2002).

14   Conway, H., Hall, B. L., Denton, G. H., Gades, A. M. & Waddington, E. D. Past and future grounding-line retreat of the West Antarctic Ice Sheet. *Science* **286**, 280-283 (1999).

15   Huybrechts, P. Sea-level changes at the LGM from ice-dynamic reconstructions of the Greenland and Antarctic ice sheets during the glacial cycles. *Quaternary Science Reviews* **21**, 203-231, doi:10.1016/s0277-3791(01)00082-8 (2002).

16   Denton, G. H. & Hughes, T. J. Reconstructing the Antarctic Ice Sheet at the Last Glacial Maximum. *Quaternary Science Reviews* **21**, 193-202, doi:10.1016/s0277-3791(01)00090-7 (2002).

17   Parrenin, F. *et al.* 1-D-ice flow modelling at EPICA Dome C and Dome Fuji, East Antarctica. *Climate of the Past* **3**, 243-259 (2007).

18   Pollard, D. & DeConto, R. M. Modelling West Antarctic ice sheet growth and collapse through the past five million years. *Nature* **458**, 329-U389, doi:10.1038/nature07809 (2009).

19   Whitehouse, P. L., Bentley, M. J. & Le Brocq, A. M. A deglacial model for Antarctica: geological constraints and glaciological modelling as a basis for a new model of Antarctic glacial isostatic adjustment. *Quaternary Science Reviews* **32**, 1-24, doi:10.1016/j.quascirev.2011.11.016 (2012).

20   Conway, H. & Rasmussen, L. A. Recent thinning and migration of the Western Divide, central West Antarctica. *Geophysical Research Letters* **36**, doi:L12502 10.1029/2009gl038072 (2009).

21   Dahl-Jensen, D., Gundestrup, N., Gogineni, S. P. & Miller, H. Basal melt at NorthGRIP modeled from borehole, ice-core and radio-echo sounder observations. *Annals of Glaciology, Vol 37* **37**, 207-212, doi:10.3189/172756403781815492 (2003).

22   Dansgaard, W. & Johnsen, S. J. A flow model and a time scale for the ice core from Camp Century, Greenland. *Journal of Glaciology* **8**, 215-223 (1969).

23   Cuffey, K. M. & Paterson, W. S. B. *The Physics of Glaciers*. Fourth Edition edn, (2010).

24   Delmonte, B. *et al.* Dust size evidence for opposite regional atmospheric circulation changes over east Antarctica during the last climatic transition. *Climate Dynamics* **23**, 427-438, doi:10.1007/s00382-004-0450-9 (2004).

25   Bertler, N. *et al.* Snow chemistry across Antarctica. *Annals of Glaciology, Vol 41, 2005* **41**, 167-179 (2005).

26   Kaspari, S., Dixon, D. A., Sneed, S. B. & Handley, M. J. Sources and transport pathways of marine aerosol species into West Antarctica. *Annals of Glaciology, Vol 41 2005* **41**, 1-9, doi:10.3189/172756405781813221 (2005).

27   Mayewski, P. A. *et al.* West Antarctica's Sensitivity to Natural and Human Forced Climate Change over the Holocene. *Journal of Quaternary Science* (in press).

28   Rothlisberger, R. *et al.* Dust and sea salt variability in central East Antarctica (Dome C) over the last 45 kyrs and its implications for southern high-latitude climate. *Geophysical Research Letters* **29**, doi:10.1029/2002gl015186 (2002).

29   Wolff, E. W. *et al.* Southern Ocean sea-ice extent, productivity and iron flux over the past eight glacial cycles. *Nature* **440**, 491-496, doi:10.1038/nature04614 (2006).

30   Fischer, H. *et al.* Reconstruction of millennial changes in dust emission, transport and regional sea ice coverage using the deep EPICA ice cores from the Atlantic and Indian Ocean sector of Antarctica. *Earth and Planetary Science Letters* **260**, 340-354, doi:10.1016/j.epsl.2007.06.014 (2007).

31   Rothlisberger, R., Crosta, X., Abram, N. J., Armand, L. & Wolff, E. W. Potential and limitations of marine and ice core sea ice proxies: an example from the Indian Ocean sector. *Quaternary Science Reviews* **29**, 296-302, doi:10.1016/j.quascirev.2009.10.005 (2010).

32   Rojas, M. *et al.* The Southern Westerlies during the last glacial maximum in PMIP2 simulations. *Climate Dynamics* **32**, 525-548, doi:10.1007/s00382-008-0421-7 (2009).

33   Mahowald, N. M., Lamarque, J. F., Tie, X. X. & Wolff, E. Sea-salt aerosol response to climate change: Last Glacial Maximum, preindustrial, and doubled carbon dioxide climates. *Journal of Geophysical Research-Atmospheres* **111**, doi:10.1029/2005jd006459 (2006).

34   Holland, P. R. & Kwok, R. 2012. Wind-driven trends in Antarctic sea-ice drift. *Nature Geoscience*, **5** 872-875.

35   Roeckner, E. *et al.* Vol. 218   (Max Planck Institut für Meteorologie Report, 1996).

36   Hoffmann, G., Werner, M. & Heimann, M. Water isotope module of the ECHAM atmospheric general circulation model: A study on timescales from days to several years. *Journal of Geophysical Research-Atmospheres* **103**, 16871-16896, doi:10.1029/98jd00423 (1998).

37   Ding, Q. H., Steig, E. J., Battisti, D. S. & Kuttel, M. Winter warming in West Antarctica caused by central tropical Pacific warming. *Nature Geoscience* **4**, 398-403, doi:10.1038/ngeo1129 (2011).

38   Braconnot, P. *et al.* Results of PMIP2 coupled simulations of the Mid-Holocene and Last Glacial Maximum - Part 1: experiments and large-scale features. *Climate of the Past* **3**, 261-277 (2007).

39   Peltier, W. R. Global glacial isostasy and the surface of the ice-age earth: The ice-5G (VM2) model and grace. *Annual Review of Earth and Planetary Sciences* **32**, 111-149, doi:10.1146/annurev.earth.32.082503.144359 (2004).

40   Ackert, R. P. *et al.* Controls on interior West Antarctic Ice Sheet Elevations: inferences from geologic constraints and ice sheet modeling. *Quaternary Science Reviews* **65**, 26-38 (2013).

41   Roche, D. M., Crosta, X. & Renssen, H. Evaluating Southern Ocean sea-ice for the Last Glacial Maximum and pre-industrial climates: PMIP-2 models and data evidence. *Quaternary Science Reviews* **56**, 99-106, doi:10.1016/j.quascirev.2012.09.020 (2012).

42   Van Ommen, T. D., Morgan, V. & Curran, M. A. J. Deglacial and Holocene changes in accumulation at Law Dome, East Antarctica. *Annals of Glaciology, Vol 39, 2005* **39**, 359-365, doi:10.3189/172756404781814221 (2004).

43   Huybers, P. Early Pleistocene glacial cycles and the integrated summer insolation forcing. *Science* **313**, 508-511, doi:10.1126/science.1125249 (2006).

44   Huybers, P. & Denton, G. Antarctic temperature at orbital timescales controlled by local summer duration. *Nature Geoscience* **1**, 787-792, doi:10.1038/ngeo311 (2008).
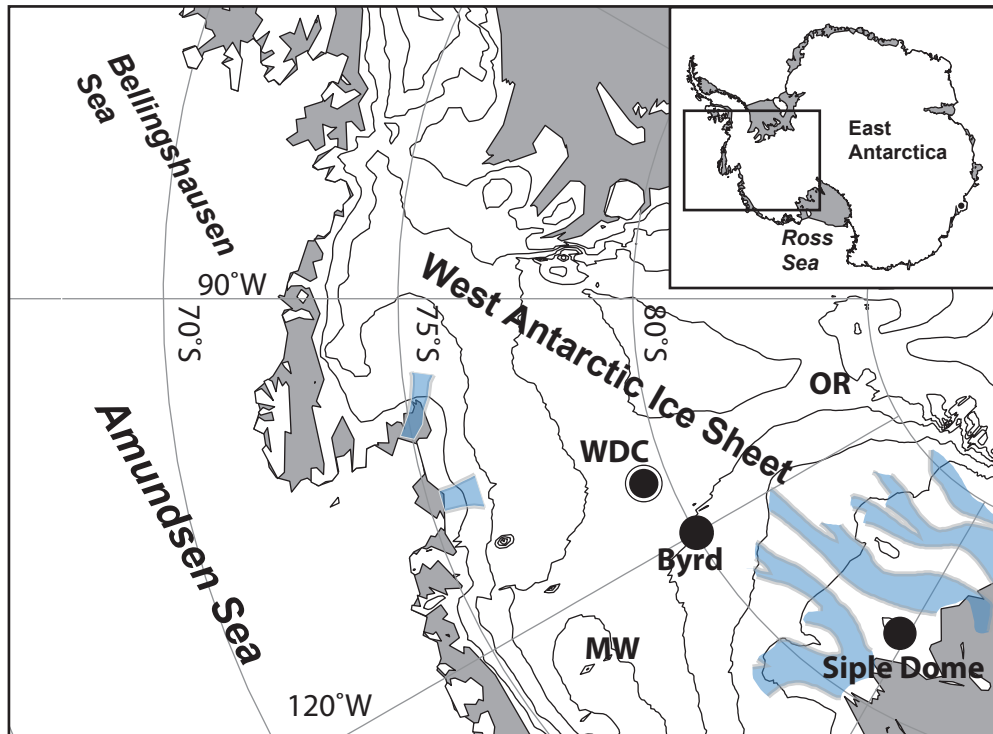
Figure S1. Map of West Antarctica.
Locations of the WDC, Byrd, and Siple Dome ice cores and the Ohio Range (OR) and Mt. Waesche (MW). Ice shelves are shown in gray; Siple Coast and Amundsen Sea ice streams are shown by blue shading. Contour interval is 500 m.
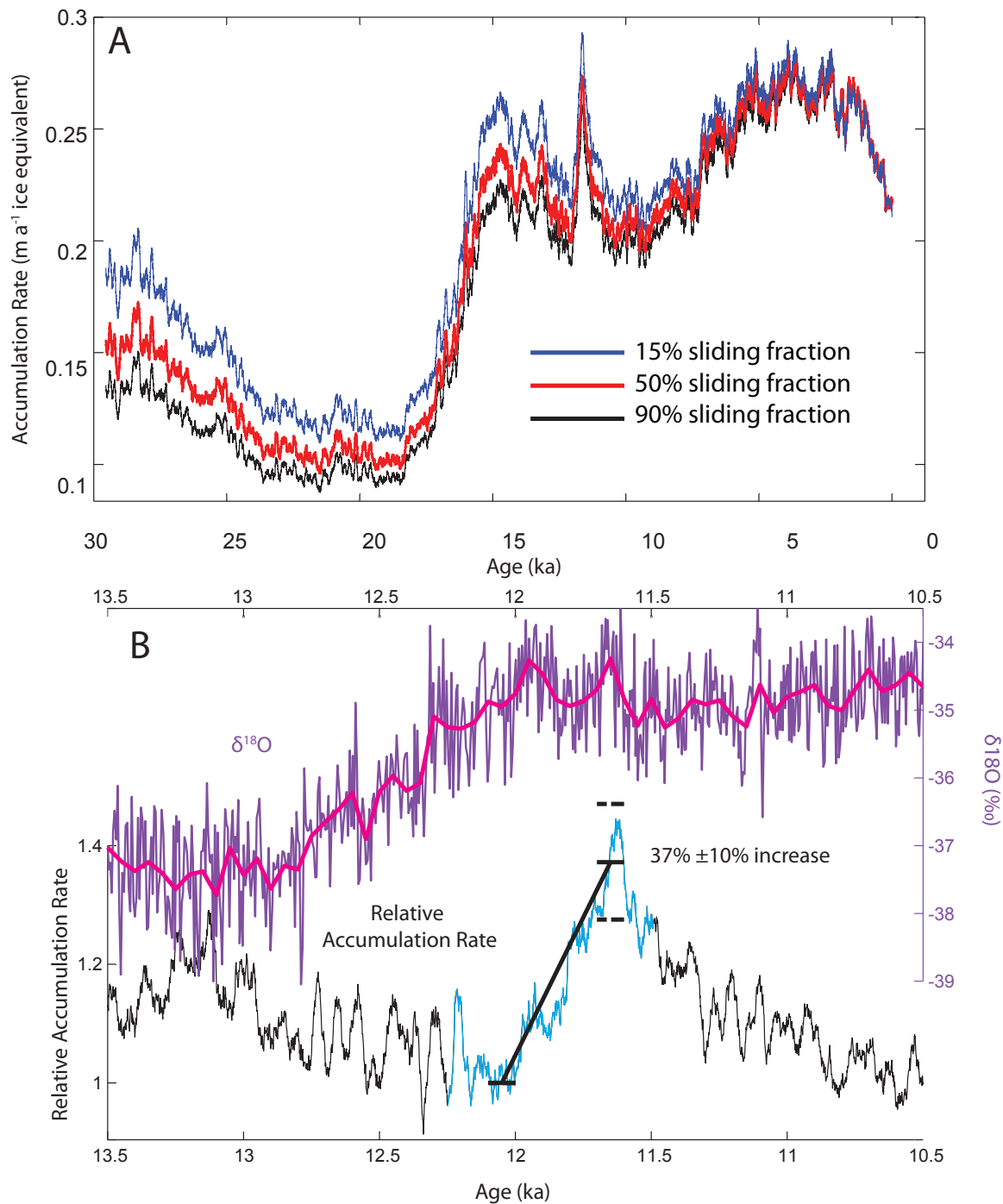
Figure S2: Accumulation Rate History.
(A) Inferred accumulation rate using a one-dimensional ice-flow model and three different vertical-strain profiles. The red profile is preferred. Accumulation rates shown are the 100-year running average.
(B) 31-year running average of accumulation rate relative to 100-year average between 12.1 and 12.0 ka. The relative accumulation rate increase between 12.1 to 12.0 ka and 11.7 to 11.6 ka is shown with the thick black line. The uncertainty bounds are the additive effects of possible ice-thickness change (3%), ice advection through an accumulation gradient (3%), and annual-layer interpretation uncertainties (4%). The annual-layer interpretation for the section in light blue (1940 to 2020 m) was confirmed with multi-parameter chemistry measurements; black is from ECM only. The ECM-only interpretation from 1940 to 2020 m found 19 fewer years (2.5%) and the same magnitude of accumulation rate change. Note that trends in relative accumulation rate are less certain away from the abrupt increase.
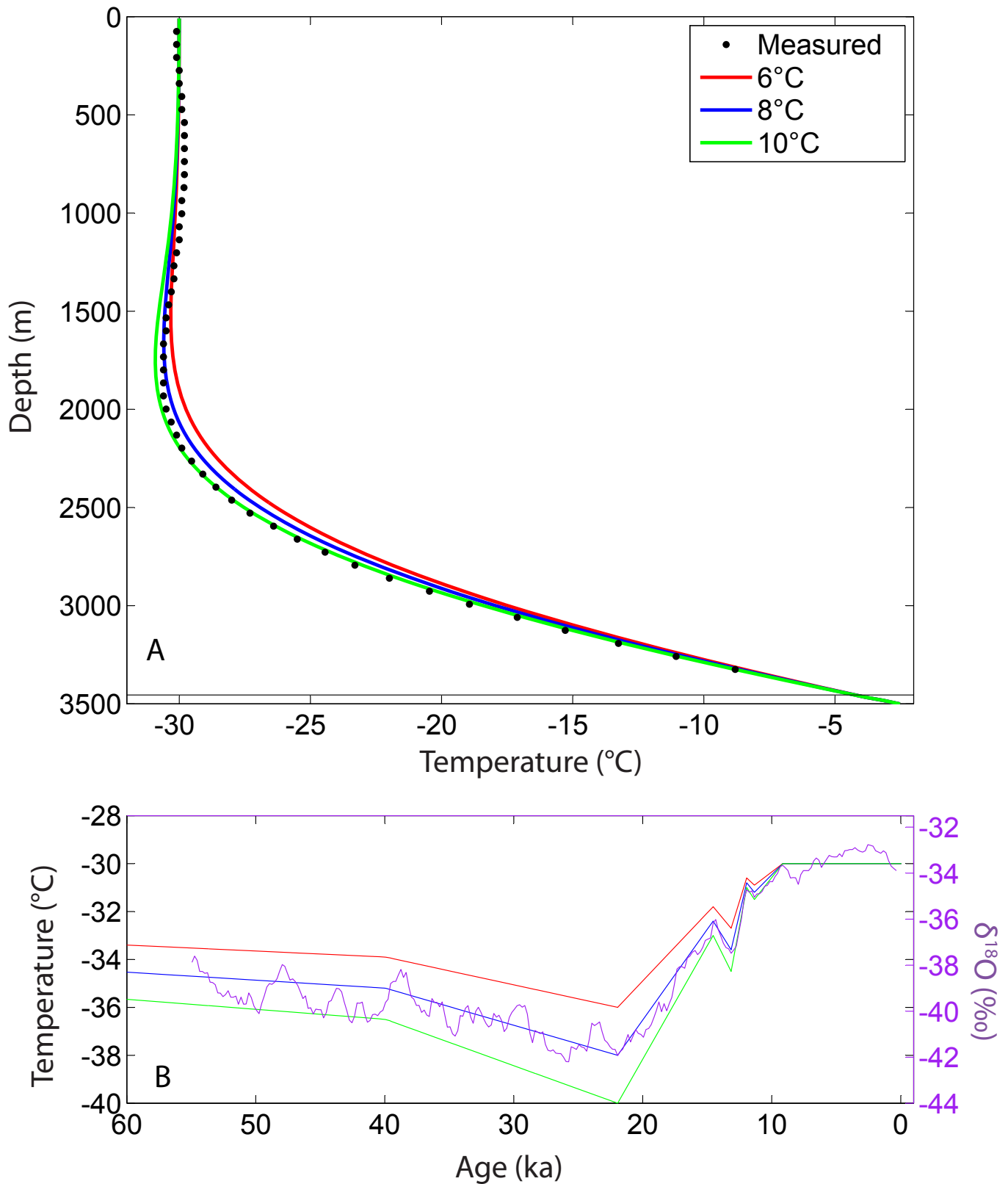
Figure S3. Borehole Temperature Profile and Surface Temperature History.
Match of modeled temperature profiles (A) with surface temperature histories shown in (B) to the measured borehole temperature profile. Legends in (A) indicate the magnitude of the glacial-interglacial temperature change used in the model runs.
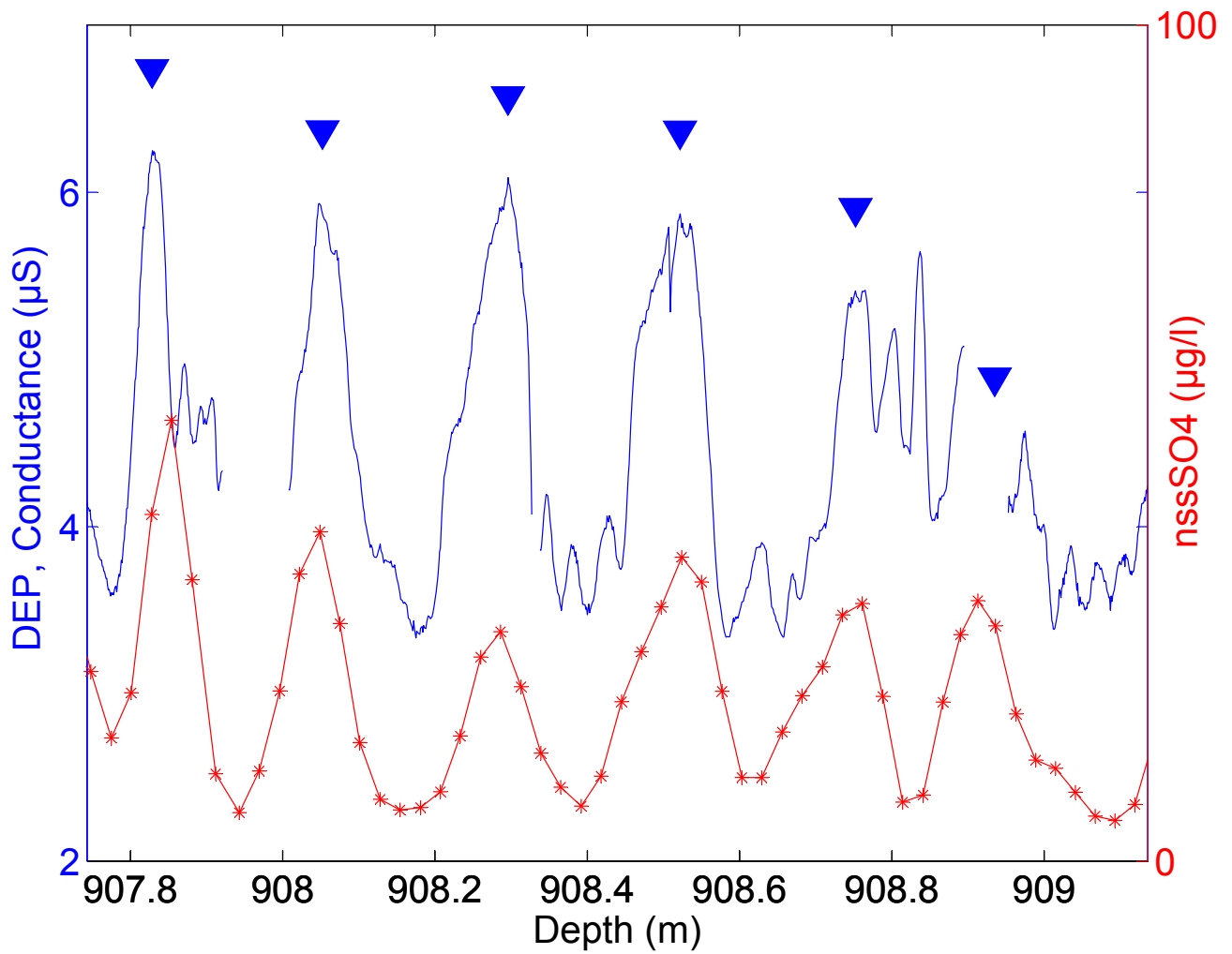
Figure S4. Brittle Ice Annual Signals
Comparison of electrical (dielectric profiling) and chemical (non-sea-salt sulfate) annual signals in a section of brittle ice that was rated "very poor," the worst rating for ice quality. Blue triangles are annual layer picks.
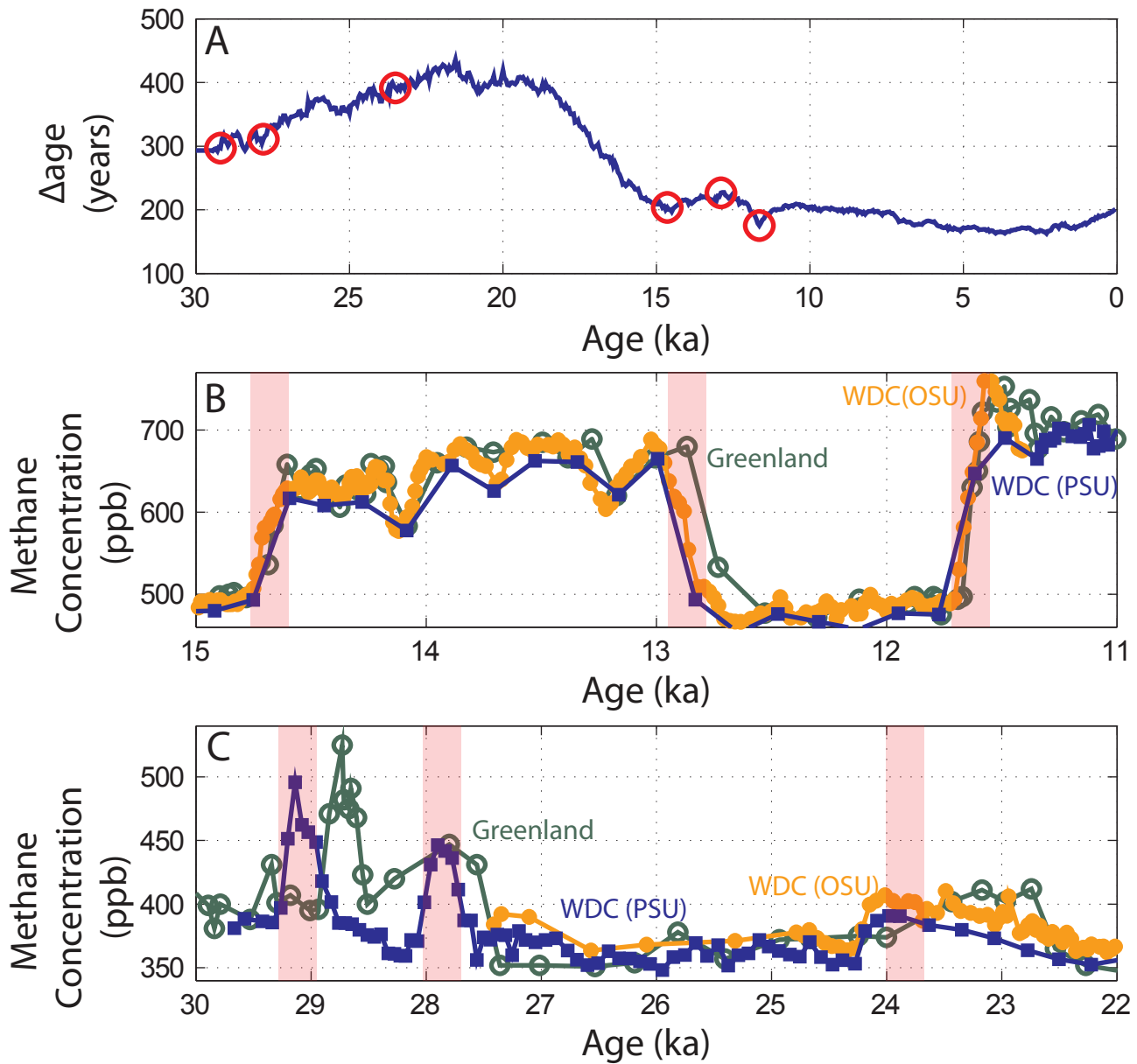
Figure S5: Assessment of WDC06A-7 Timescale via atmospheric methane.

A) Δage for WDC calculated with Herron and Langway[27] firn densification model using the inferred accumulation rate and temperature histories. Circles are the Δage values at the times of abrupt variations in methane used to compare timescales.

B and C) WDC methane on WDC06A-7 minus Δage and Greenland methane composite on GICC05 gas timescale[33]. Red vertical bars correspond to the times of the red circles in A where the Δage was calculated. The age differences between the WDC and Greenland timescales are shown in Figure S6.
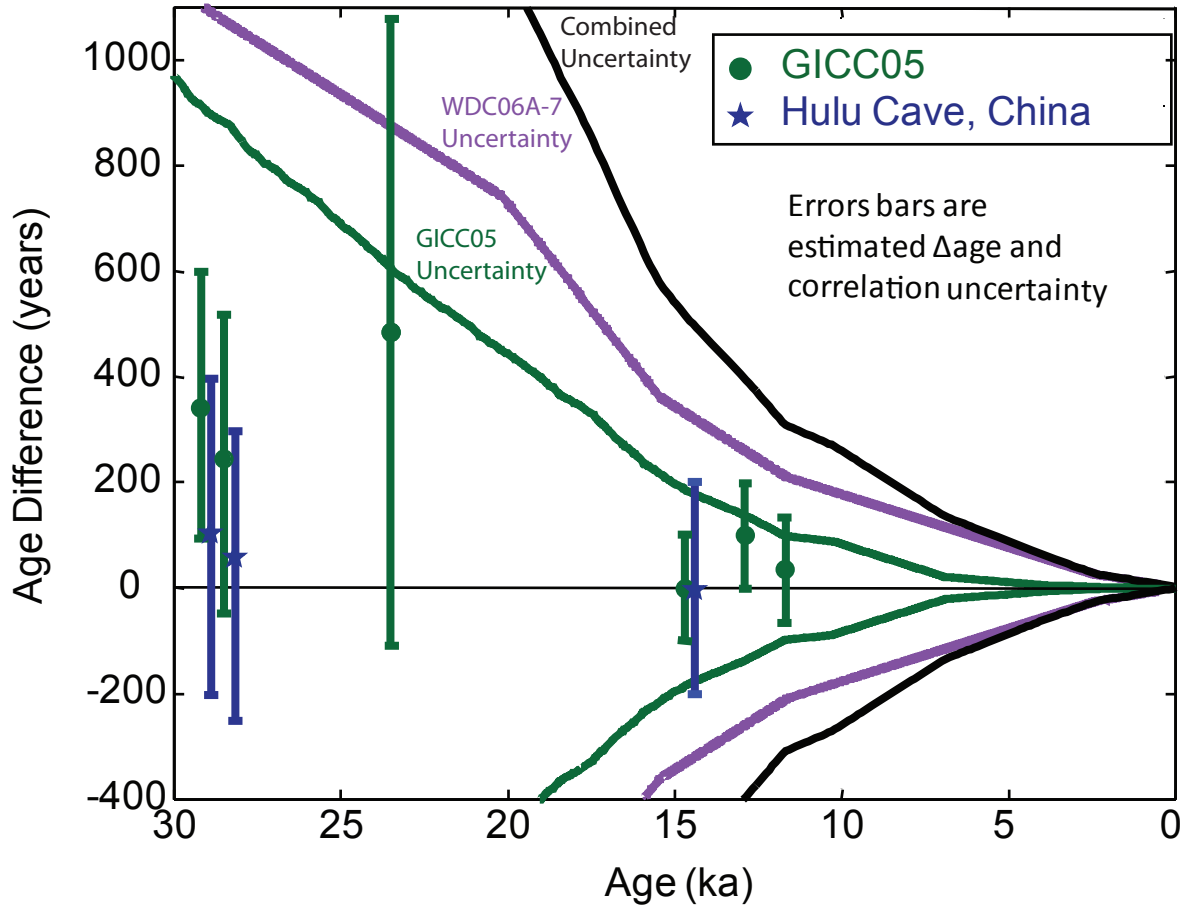
Figure S6: Timescale Comparison
Age differences between methane records shown in Figure S5 for
WDC06A-7 and GICC05[33,40] and age differences between WDC methane and
stalagmite $\delta^{18}O$ from Hulu Cave[41]. Uncertainty of age comparisons is the Δ
age and correlation uncertainties and does not include timescale uncer-
tainties.
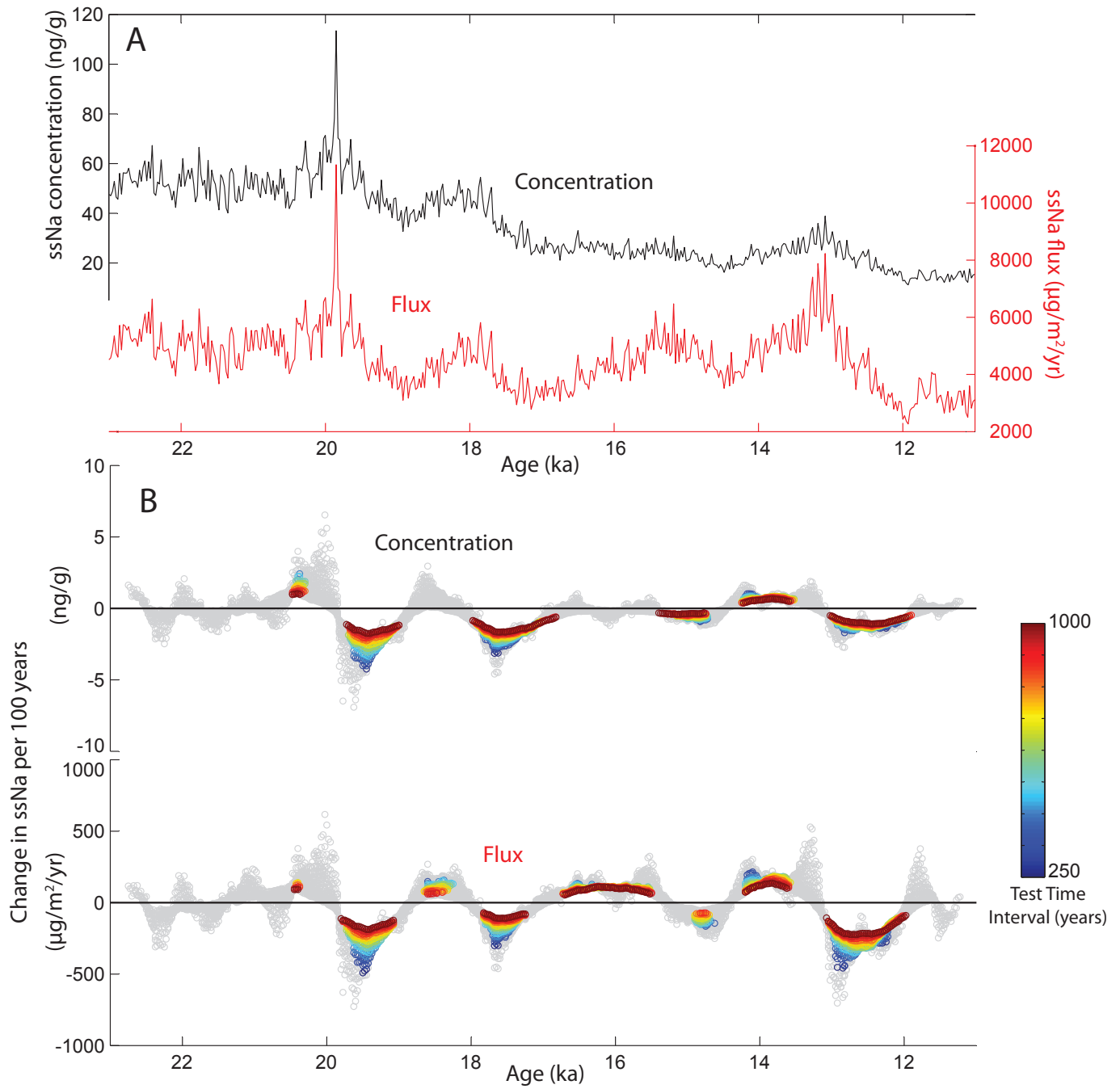
Figure S7: Sea-salt sodium (ssNa) concentration and flux.
Results of rank sum test shown in (B) are described in methods. Colored circles indicate times of significant change.
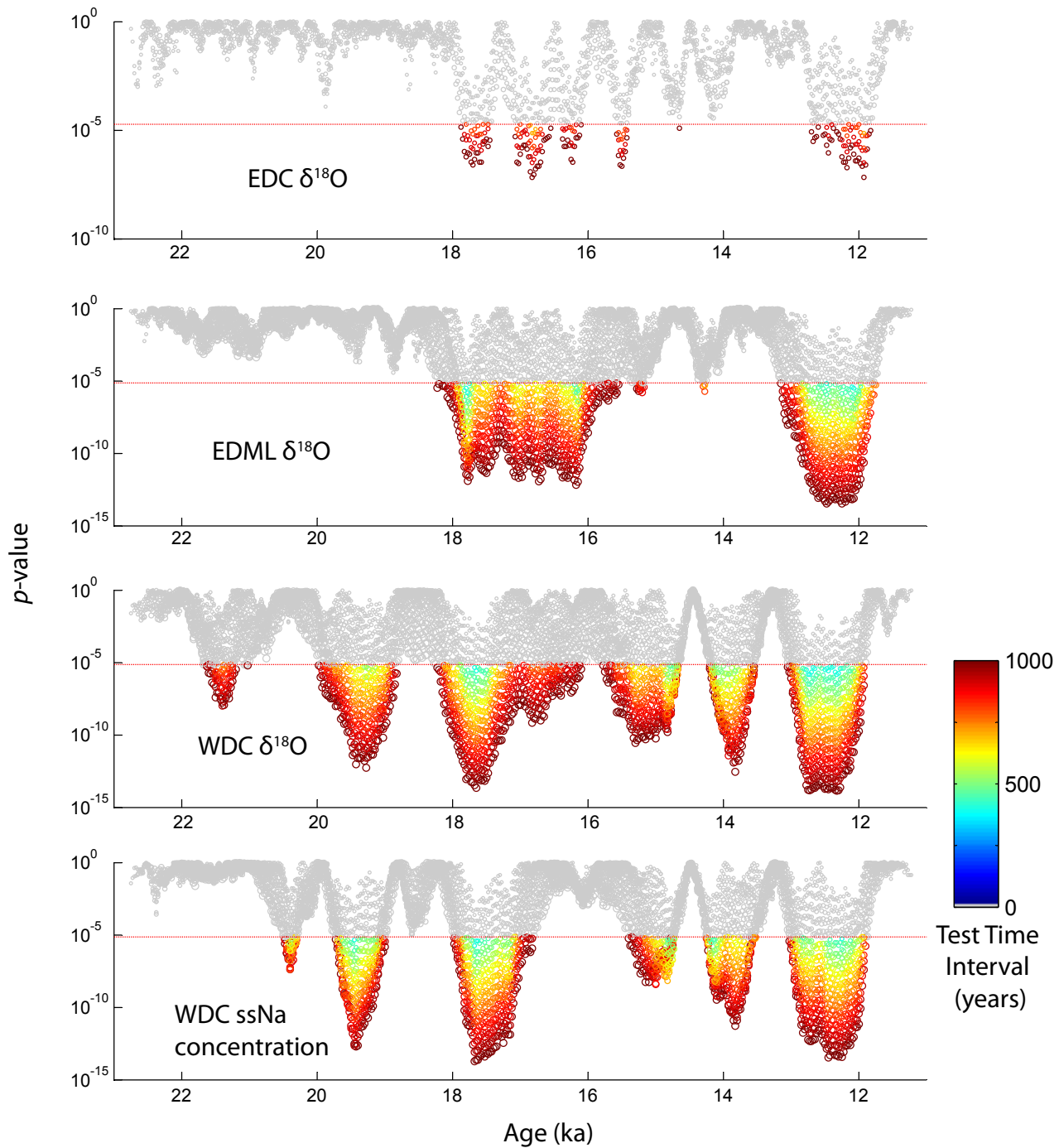
Figure S8. Significance levels for Wilcoxon Rank Sum tests.
The four plots show the *p*-values of the sliding Wilcoxon Rank Sum test for the difference of medians shown in Figure 2. The test algorithm and interpretation is described in Methods. The 95% a posteriori confidence level, that accounts for the large number of test realizations, is shown with the red line. Each point is a test realization and is colored by the test time interval.
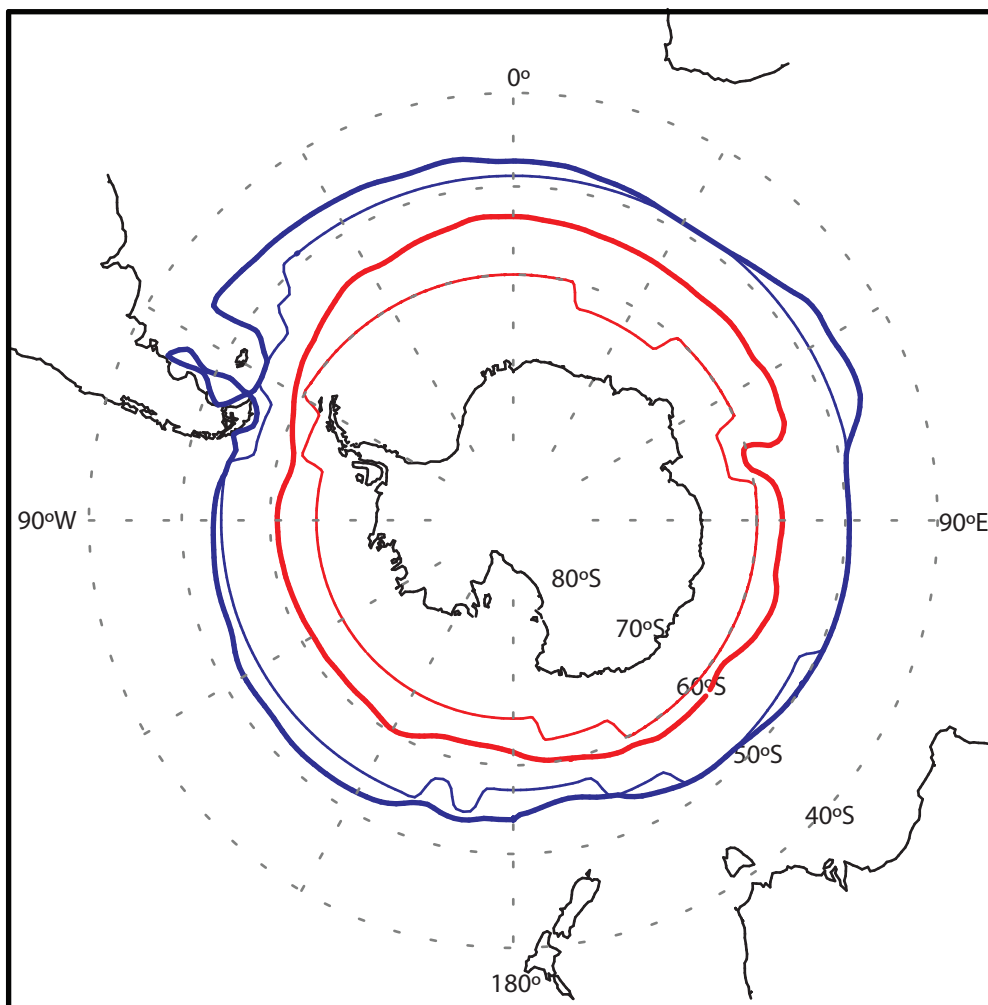
Figure S9: Sea-ice reduction in climate model experiements.
Thick line is control run; thin line is reduced sea-ice run. Blue is winter (July) and red is summer (January) sea-ice extent.
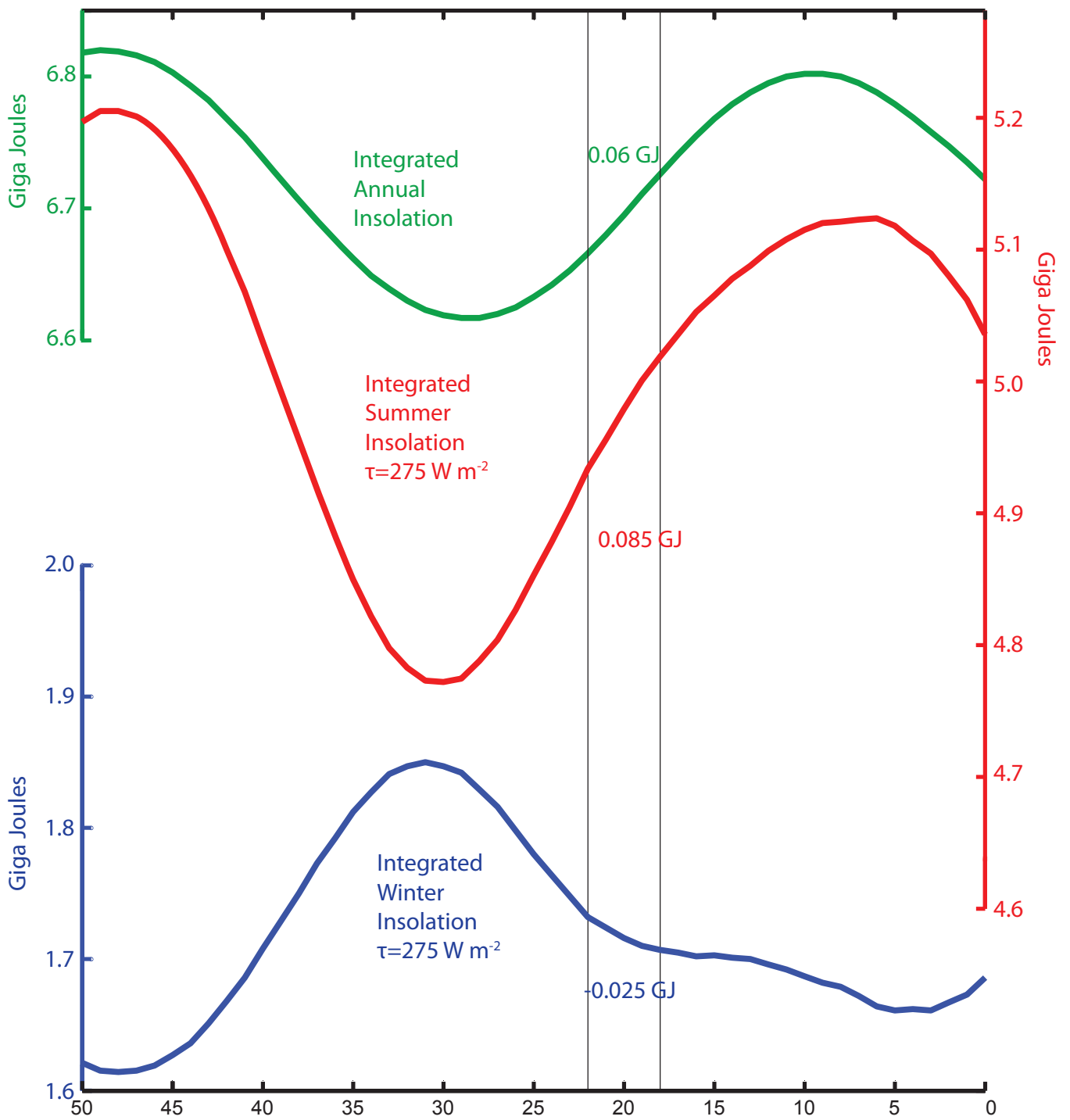
Figure S10. Integrated insolation.
Integrated insolation at 65°S from Huybers[71]. Values are the increase in insolation between 22 and 18 ka (black lines).

Chapter 6: *Accuracy and uncertainty of interpolation methods for Antarctic ice-core timescales: application to Byrd, Siple Dome and Law Dome ice cores*

In review at Climate of the Past

This paper uses the annually resolved timescale for WAIS Divide to assess the accuracy of different schemes for interpolating between depth-age tie points. We develop a non-linear inverse technique to find either the smoothest accumulation rate history or the smoothest annual layer thickness profile that matches depth-age tie points exactly. These two inverse interpolations perform substantially better than either linear and spline interpolations. Three coastal Antarctic ice-core timescales were created with near-linear interpolation. We show that linear interpolation has three major problems: 1) large age uncertainty between tie points; 2) large changes in the duration of climate events at tie points; and 3) a bias to older ages. We apply the smoothest annual-layer thickness interpolation to the three timescales and show that the method of interpolation affects certain climate interpretations, in particular the timing of the onset of deglacial warming.

The idea for smooth interpolation of ice-core timescales was from Ed and Twit. Using this idea, I developed a new inverse procedure to solve for the smoothest accumulation rate history as well as developed the smoothest annual layer thickness method. Kendrick Taylor helped create the WDC06A-7 timescale which I used as a reference timescale to illustrate the effectiveness of different interpolation techniques. I also applied the smooth interpolation method to 3 existing ice-core timescales to illustrate the importance of the interpolation in paleoclimate interpretations.

1 **Interpolation methods for Antarctic ice-core timescales: application to Byrd,**
2 **Siple Dome and Law Dome ice cores**
3

4 T.J. Fudge[1], Edwin D. Waddington[1], Howard Conway[1], Jessica M.D. Lundin[1], Kendrick Taylor[2]
5

6 [1]Department of Earth and Space Sciences, University of Washington, Seattle, WA
7 [2]Desert Research Institute, Nevada System of Higher Education, Reno, NV
8

9 **Abstract**
10 Antarctic ice cores have often been dated by matching distinctive features of atmospheric
11 methane to those detected in annually dated ice cores from Greenland. Establishing the timescale
12 between these tie-point ages requires interpolation. While the uncertainty at tie points is
13 relatively well described, uncertainty of the interpolation is not. Here we assess the accuracy of
14 three interpolation schemes using data from the WAIS Divide ice core in West Antarctica; we
15 compare the interpolation methods with the annually resolved timescale for the past 30 kyr.
16 Linear interpolation yields large age errors (up to 380 yr) between tie points, abrupt changes in
17 duration at tie points, and an age bias. Interpolation based on the smoothest accumulation rate
18 (ACCUM) or the smoothest annual-layer thickness (ALT) yield timescales that more closely
19 agree with the annually resolved timescale and do not have abrupt changes in duration at the tie
20 points. We use ALT to assess the uncertainty in existing timescales for the past 30 kyr from
21 Byrd, Siple Dome, and Law Dome. These ice-core timescales were developed with methods
22 similar to linear interpolation. Maximum age differences exceed 1000 yr for Byrd and Siple
23 Dome, and 500 yr for Law Dome. For the glacial-interglacial transition (21 to 12 kyr), the
24 existing timescales are, on average, older than ALT by 40 years for Byrd, 240 years for Siple
25 Dome, and 150 years for Law Dome. Because interpolation uncertainty is often not considered,
26 age uncertainties for ice-core records are often underestimated.
27

28 **Introduction**
29 Interpretation of paleoclimate records depends on accurate chronologies. Ice cores
30 provide exceptional records of past climate (Grootes et al., 1993; EPICA Members, 2006) and
31 are among the best-dated paleoclimate records (Meese et al., 1998; Svensson et al., 2008). In
32 Greenland, the ice-core timescales are based on identification of annual layers preserved in the
33 ice; the Greenland Ice Core Chronology (GICC05, Svensson et al., 2008) has identified layers to
34 60 kyr (thousands of years before 1950). In Antarctica, dating of ice cores has been challenging
35 because low accumulation at many sites hampers annual-layer identification. Thus, Antarctic
36 timescales are often derived by matching distinctive age markers detected and dated in
37 Greenland timescales. Abrupt variations of atmospheric methane are the most commonly used tie
38 points (Blunier et al., 1998) and some combination of approximately 11 events in the past 30 kyr
39 (Figure 1) have been used to transfer Greenland timescales to Antarctic ice cores. Other potential
40 markers such as volcanic ash, cosmogenic isotope anomalies (Raisbeck et al., 2007), and sulfate
41 peaks (Sigl et al., 2013; Svensson et al., 2013) either are more difficult to identify, are less
42 spatially extensive, or occur less frequently. The methane tie points allow the gases to be dated,
43 but there is an additional step to derive the ice timescale. For any given depth in an ice core, the
44 gas trapped in bubbles is younger than the ice because the gas is not trapped until 50 to 100 m
45 below the surface. The difference between the age of the ice and the age of the gas, termed Δage,
46 must be added to gas ages to derive the ice timescale.

47
48 The age uncertainty at the methane tie points is well described (e.g. Blunier et al. 1998; Blunier
49 et al., 2007; Pedro et al., 2011; Stenni et al., 2011), but uncertainty introduced by the
50 interpolation scheme is often given less attention. Two common approaches are used to
51 interpolate between methane tie points. In the first approach, variations of linear interpolation
52 were used to construct timescales for Taylor Dome (Steig et al., 1998), Byrd (Blunier and Brook,
53 2001), Siple Dome (Brook et al., 2005), and Law Dome (Pedro et al., 2011). In the second
54 approach, Bayesian statistical methods are applied to multiple ice cores simultaneously
55 (Lemieux-Dudon et al., 2010). This method starts with initial timescales derived from ice-flow
56 modeling driven by accumulation-rate histories based on the stable-isotope records. The initial
57 timescales are then adjusted to optimize the agreement among all timescales, within their
58 uncertainties. This method has been used to construct consistent timescales for EDML, EDC,
59 Vostok, and Talos Dome (Lemieux-Dudon et al., 2010; Stenni et al., 2011; Veres et al., 2013;
60 Bazin et al., 2013). Uncertainties are computed based on the uncertainties of tie points and
61 variances of the accumulation rate, thinning function, and lock-in depth used in the initial
62 timescale.
63
64 Assessing the interpolation uncertainty of previous Antarctic timescales is not straightforward
65 because there is no "true" timescale with which to compare. The new WAIS Divide timescale,
66 with annual resolution for the past 30 kyr, provides an opportunity to assess the interpolation
67 uncertainty; by constructing timescales for WAIS Divide assuming known tie-point ages, the
68 various interpolation methods can be compared to the "true" annually resolved timescale. We
69 focus on three interpolation methods: linear, smoothest accumulation rate (ACCUM), and
70 smoothest annual-layer thickness (ALT). ACCUM is based on the work of Waddington et al.
71 (2003) which showed that linear interpolations of depth-age between known tie points imply
72 artificial saw-tooth histories in accumulation-rate, even in the presence of steady-state ice flow.
73 In order to get a physically-based depth-age interpolation, they introduced an inverse procedure
74 that inferred a smooth accumulation-rate history such that the depth-age calculated with an ice-
75 flow model matched the tie points to an acceptable tolerance. Lundin (2012) and Lundin et al. (in
76 prep.) further developed the concept and show that for synthetic timescales with white noise
77 added to the tie points, interpolating with the smoothest accumulation rate can improve the age
78 estimates of tie points.
79
80 In this work, we use ACCUM and ALT in the limiting case where tie-point ages are assumed to
81 be known exactly. This allows the interpolation uncertainty to be isolated from the tie-point
82 uncertainty. We show that ACCUM and ALT agree with the WAIS Divide annual timescale
83 better than linear interpolation and then discuss the uncertainty of three existing timescales (Siple
84 Dome, Byrd, and Law Dome) that use near-linear interpolation.
85
86 **Methods**
87 We evaluate interpolation methods using the WDC06A-7 timescale for the WAIS Divide ice
88 core (WAIS Divide Project Members, 2013). The WDC06A-7 timescale is based primarily on
89 electrical measurements and is annually resolved to 29.6 kyr (2800 m depth of a total ice
90 thickness is ~3450 m). We use WDC06A-7 as the "true" timescale. We use eleven tie points
91 (Table 1) to evaluate three interpolation schemes by interpolating between these tie points and
92 comparing results with the "true' timescale. The tie points are at times of abrupt methane

93   variations except during the mid and late Holocene when they are evenly spaced (2, 4, and 6
94   kyr). An additional tie point older than the annual timescale (35.9 kyr) is included to constrain
95   the variations in annual-layer thickness at the older boundary.
96
97   The interpolation methods are:
98   1) Linear – yields constant annual-layer thicknesses between age markers.
99   2) ACCUM - uses a simple ice-flow model and an inverse method to find the smoothest
100   accumulation-rate history that matches the depth-age markers.
101   3) ALT - uses an inverse method to find the smoothest progression of annual-layer
102   thicknesses that fit the depth-age markers.
103   In all cases, the interpolations are forced to match the age of tie points nearly exactly.
104
105   We do not use the stable-isotope record as a guide for interpolation. At many Antarctic ice-core
106   sites, a relationship between stable-isotopes and accumulation rate is assumed based on the
107   saturation vapor pressure (e.g. Petit et al., 1999). This relationship is not well suited to West and
108   coastal Antarctica. For example in the modern climate, WAIS Divide is 2‰ more depleted in
109    $\delta^{18}O$ than Byrd despite a ~50% higher accumulation rate. At both Taylor Dome and Law Dome,
110   the Holocene accumulation rates show little resemblance to the stable-isotope records (Monnin et
111   al., 2004; van Ommen et al., 2004). These observations suggest that both spatial and temporal
112   relationships between stable isotopes and accumulation rate are complex.
113
114   Ice-flow models forced by accumulation rates inferred from stable isotopes do not exactly match
115   tie points (Ruth et al., 2007; Parrenin et al., 2007) and are commonly adjusted to better match the
116   depth of age markers (e.g. Dreyfus et al., 2007). The Bayesian statistical approach (Lemieux-
117   Dudon et al., 2010; Veres et al., 2013; Bazin et al., 2013) allows the thinning function to vary
118   within a tolerance to better reconcile the age of tie points with the modeled timescale. Because
119   there is no simple way to reproduce this methodology for a single core and allow only the
120   interpolation between tie-points to change, we do not apply it to WDC06A-7; instead, we
121   compare ALT with three different published timescales for EDML and discuss the consistency of
122   the interpolations in a later section.
123
124   ACCUM and ALT have not previously been used to derive timescales for ice cores. We choose
125   to find the smoothest histories because we want the inferred histories to have the minimum
126   structure required to fit the data. ACCUM minimizes the variability in the inferred accumulation
127   history while ALT minimizes layer-thickness variations, which are related to the accumulation
128   rate by the thinning function. Because the thinning function, which gives the cumulative amount
129   of thinning a layer has experienced, is smooth in time, this leads to both ACCUM and ALT
130   constraining the accumulation-rate variability. ACCUM requires an ice-flow model to estimate
131   the thinning function. Although we use a one-dimensional ice-flow model (Dansgaard and
132   Johnsen, 1969; WAIS Divide Project Members, 2013), a coupled thermo-mechanical model
133   could also be used. We assume that all inputs necessary for the ice-flow model except the
134   accumulation rate are known. The influence of the assumed ice-flow model inputs are discussed
135   in a following sub-section. Assumptions about model parameters and ice-flow history are not
136   needed when using ALT.
137

138 The underlying assumption that accumulation rate varies smoothly breaks down in situations of
139 abrupt changes as observed in Greenland at Dansgaard-Oeschger events (e.g. Alley et al., 1997).
140 Even relatively small changes such as the increase in accumulation rate evident in WDC06A-7
141 between 12.0 and 11.6 kyr are difficult to match without closely spaced tie points; this event is
142 discussed in more detail below.
143
144 *Smoothest Accumulation Rate and Annual-layer thickness Interpolations*
145 We use a standard inverse procedure (Aster et al., 2005) to minimize the data misfit and the
146 smoothness of either the annual-layer thickness or accumulation-rate history for a given trade-off
147 parameter v, and define a performance index:
148

$$I^2 = \left\|\frac{G(\boldsymbol{m})-\boldsymbol{d}}{\sigma}\right\|_2^2 + v^2\|\boldsymbol{Lm}\|_2^2 \tag{1}$$

149
150
151 where $\boldsymbol{m}$ is the parameter being solved for (either accumulation-rate history or annual-layer
152 thickness profile), $G(\boldsymbol{m})$ is a function that relates $\boldsymbol{m}$ to the depth-age scale, $\boldsymbol{d}$ are the depths of tie
153 points, σ is the standard deviation of the measurement error and assumed to be normally
154 distributed, and $\boldsymbol{L}$ is the matrix second derivative operator for calculating smoothness. Bold
155 capital letters denote matrices, bold lower case letters denote vectors, and $\| \: \|_2^2$ indicates an L2
156 norm (sum of squares, e.g. Aster et al., 2005). The uncertainty, σ, is a scalar because we assume
157 that each tie-point is equally well known.
158
159 The forward problem in this solution procedure, denoted as $G(\boldsymbol{m})$, can be any function that maps
160 either accumulation rate or annual-layer thickness to a depth-age relationship. In the case of
161 ACCUM, $\boldsymbol{m}$ is the set of accumulation rates at the specified calculation times. The forward
162 problem is a Dansgaard-Johnsen (1969) ice-flow model modified following Dahl-Jensen et al.
163 (2003) to account for basal melting and sliding. In addition to the accumulation rate, the ice-flow
164 model requires histories of basal melting, the fraction of surface motion from basal sliding, ice
165 thickness, and the kink-height which dictates the shape of the vertical velocity profile. We
166 choose this model because it has been applied widely to ice cores and is computationally
167 inexpensive, but any ice-flow model could be used. In the case of the smoothest annual-layer
168 thickness, the function $G(\boldsymbol{m})$ is simply an integration of the annual-layer thickness profile. The
169 ACCUM interpolation can be written as a linear inverse problem (Lundin et al., in prep.) which
170 allows the uniqueness of the solution to be proven. However, the linear method is also restricted
171 to sites where the ice sheet is frozen to the bed. By using a generalized non-linear solution
172 procedure, we can apply this technique to sites like WAIS Divide that have experienced basal
173 melting, with confidence that the solution is unique based on the linear formulation (see
174 Appendix A). Further, the solution technique can be extended to a range of problems that are not
175 linear such as finding the ice-thickness history that best matches the depth-age tie points given a
176 known accumulation-rate history (e.g. Price et al., 2007).
177
178 We find the best-fit models using a Gauss-Newton iterative inverse procedure (Aster et al., 2005,
179 Section 10.1; Ganse, 2013). This is a steepest descent solver that uses the linear relationship
180 between the model perturbations and the data residuals (Appendix A). We fit the known depth-
181 age tie points near exactly because this work is focused on the sensitivity of the timescales to the
182 interpolation method. The trade-off parameter, v, is chosen such that the maximum misfit in
183 depth at any depth-age tie point is less than the minimum annual-layer thickness in the derived

184 timescale – typically between 1 and 10 mm. We do not discuss the application using the
185 smoothness criteria to improve the age estimates of the depth-age tie points; this application is
186 discussed by Lundin et al. (in prep).
187
188
189 *Comparison of ACCUM with different ice-flow parameters*
190 We assess the importance of the ice-flow model inputs in the ACCUM method by comparing
191 timescales that assume very different inputs. We use WDC06A-7 to define tie points at the
192 approximate ages of methane ties (Table 1) and match these ages near exactly. In the first case
193 (flank), we use reasonable values for WAIS Divide: no thickness change, a Dansgaard-Johnsen
194 kink height of 20% of the ice thickness appropriate for flank flow, basal melt rate of 1 cm yr^{-1},
195 and sliding over the bed contributing 50% of the surface velocity. In the second case (divide), we
196 also use no thickness change, but we specify a Dansgaard-Johnsen kink height of 0.7 for divide
197 flow, and no basal melting or sliding (Raymond, 1983; Conway et al., 1999).
198
199 Inferred accumulation rates are shown in Figure 2a. The different ice-flow assumptions result in
200 inferred accumulation rates that differ by more than a factor of 4. The divide case has
201 unrealistically high accumulation rates in the glacial period. Figure 2b shows age differences
202 between the two models for ice at given depths. By construction, the age differences are zero at
203 the tie points. The age differences are also relatively small between the tie points, reaching a
204 maximum of 56 years in the middle of the 6200 year gap between the tie points at 17.8 and 24.0
205 kyr. The small age differences indicate that ACCUM is relatively insensitive to the prescribed
206 ice-flow parameters. Because the thickness of a layer is the product of the accumulation rate at
207 the age of the layer and the thinning function (Appendix B), changes in the thinning function can
208 be compensated by the accumulation-rate history. The insensitivity of ACCUM to the choice of
209 ice-flow parameters is useful when interpolating timescales.
210
211
212 **Results**
213 *Assessment of Interpolation Methods using WAIS Divide data*
214 The annually resolved WDC06A-7 provides the first opportunity to directly assess interpolation
215 methods with an ice core from a location with relatively smoothly varying accumulation. The
216 100-year running average of annual-layer thicknesses is shown in Figure 3. Significant
217 centennial variability is evident, but apart from the notable exception between 11.6 and 12 kyr,
218 there is no evidence of abrupt climate changes similar to Dansgaard-Oeschger events in the
219 Greenland ice-core records. Between 11.6 and 12.0 kyr the average annual-layer thickness
220 increases by ~40%, which is interpreted as a change in accumulation rate (WAIS Divide Project
221 Members, 2013). The increase occurs during the peak of Antarctic Isotope Maximum 0
222 (corresponding to the end of the Younger Dryas) when the stable-isotope values show little
223 change. Whether this accumulation increase is specific to WAIS Divide or extends across much
224 of Antarctica is unclear because of the lack of annually resolved timescales for other ice cores.
225 This event shows that even though the Antarctic climate varies relatively smoothly, events that
226 deviate from our expectations are possible.
227
228 The annual-layer thicknesses of the three interpolation methods are also shown in Figure 3. The
229 linear interpolation causes step changes in the inferred annual-layer thickness at each tie point.

230 At some tie points, the difference in annual-layer thickness on either side of the tie point is large;
231 the annual-layer thickness changes by nearly 100% from a 3 cm thickness for ages older than
232 17.8 kyr to a 6 cm thickness for ages younger. The other two interpolation methods yield
233 smoothly varying annual-layer thicknesses that match each other and the measured annual-layer
234 thicknesses reasonably well.
235
236 The differences in age between the annually resolved WDC06A-7 and the interpolations are
237 shown in Figure 4; the yellow shading shows the uncertainty of WDC06A-7 accumulated from
238 the nearest tie point. The uncertainty accumulates quasi-linearly because either too many or too
239 few years may have been systematically identified (see WAIS Divide Project Members, 2013 for
240 specifics of the WDC06A-7 timescale and associated uncertainties). The ALT and ACCUM
241 interpolations tend to have similar age differences from WDC06A-7. The linear interpolation,
242 however, tends to be older than WDC06A-7. Because constant layer thickness between tie points
243 is assumed with linear interpolation, layers are too thin on the younger side of the interval and
244 too many years are present. After the approximate midpoint, the layers are then too thick and too
245 few years are present. In contrast, in the interval between 24 and 28 kyr, the measured annual-
246 layer thicknesses increase with age and the linear interpolation places too few layers at younger
247 ages.
248
249 All interpolation methods do a poor job of matching WDC06A-7 between 8 and 12 kyr. This is
250 not surprising, since interpolation cannot accurately capture abrupt variations between tie points.
251 Interestingly, linear interpolation provides the best match to WDC06A-7 during this interval
252 because large annual-layer thicknesses near 12 kyr reverse the trend of decreasing layer
253 thickness with age. The other interpolation methods overestimate the age because they yield
254 smaller layer thicknesses at the older side of the interval.
255
256 In the interval from 15 to 18 kyr, layer thicknesses decrease rapidly with age on WDC06A-7 due
257 to the combination of layer thinning from ice-flow and the glacial-interglacial accumulation-rate
258 change. The linear interpolation has a particularly large age difference because of the large
259 changes in layer thickness during the interval. In the interval 18 to 24 kyr, the annual-layer
260 thickness varies much less. ALT and ACCUM yield layers that are too thick near 18 kyr, with
261 corresponding ages that are too young.
262
263 < Table 2 >
264
265 The mismatch between the linear interpolation and WDC06A-7 is ~374 years, with ages that are
266 outside the estimated uncertainty of WDC06A-7 most of the time (Table 2). Both ACCUM and
267 ALT are improvements: age differences between the two are less than 20 years except during the
268 interval 24 to 17.8 kyr. Interestingly, ALT is slightly better than ACCUM in each metric. The
269 maximum mismatch for ALT is 118 years compared to 151 years for ACCUM. ALT also yields
270 fewer ages that are outside the WDC06A-7 uncertainty. The two methods are expected to be
271 quite similar since the ACCUM interpolation produces a smooth annual-layer thickness. Reasons
272 why ALT and ACCUM might differ are discussed in Appendix B.
273
274 The slightly better performance of ALT suggests that the greater complexity of ACCUM is not
275 warranted; this may be particularly true for the deepest ice where the thinning function becomes

276 increasingly uncertain and difficult to predict with ice-flow models. ACCUM will likely improve
277 in cases where the ice physics or ice-flow histories are better known; using two or three
278 dimensional ice-flow models constrained by dated internal layers imaged by radar is a promising
279 approach (e.g. Waddington et al., 2007; Steen-Larsen et al., 2010). However, in the following we
280 will use ALT to assess existing ice-core timescales because it is simpler to apply.
281
282
283 *Age Uncertainty due to Interpolation*
284 Comparison of the interpolation methods provides a framework for estimating the interpolation
285 uncertainty for other Antarctic ice-core timescales. In general, the age difference between the
286 interpolation and WDC06A-7 increases farther away from a tie point (Figure 3). We use the age
287 differences to estimate the rate at which different interpolation methods accumulate age
288 uncertainty; for instance, if the age difference 500 years from the closest tie point is 50 years,
289 then the uncertainty has accumulated at a rate of 10 years per hundred years. We calculate the
290 rate of accumulating uncertainty (absolute value of the age difference divided by years from
291 closest tie point) for all of the ages between 2 and 29.6 kyr. We exclude the topmost interval
292 because the interpolated firn-density profile does not exactly match the actual density profile. We
293 also use a final tie-point older than annually resolved timescale (35.9 kyr) to help constrain the
294 variations in annual layer thickness We then find the cumulative fraction of ages for each rate of
295 accumulating uncertainty (Figure 5). The cumulative fractions can be used as rough estimates of
296 the 1-sigma and 2-sigma rates of accumulating uncertainty. We emphasize that these are not
297 formal statistical uncertainties because they are based on a single timescale; however, they
298 provide a rough estimate in the absence of other quantitative information about timescale
299 uncertainties away from tie points.
300
301 For ALT and ACCUM, the rate of accumulating age uncertainty is less than 4 years per hundred
302 67% of the time and less than 10 years per hundred 95% of the time (Figure 5). The maximum
303 rate of accumulating uncertainty is about 20 years per hundred and occurs at the abrupt
304 accumulation increase at ~12 kyr. When the annual-layer thickness is varying more rapidly, there
305 tend to be higher rates of accumulating uncertainty. Linear interpolation accumulates uncertainty
306 at a significantly greater rate than ACCUM and ALT. The rates of accumulating uncertainty for
307 the linear interpolation are less than 8 years per hundred years 67% of the time and less than 31
308 years per hundred years for 95% of the time. Linear interpolation accumulates uncertainty at a
309 rate greater than 50 years per hundred years approximately 3% of the time.
310
311
312 *Duration Uncertainty due to Interpolation*
313 For many analyses, it is important to know both the age and duration of a climate event. The
314 duration depends on the number of annual layers between the measured depths of the onset and
315 termination of the event. Interpolation tends to underestimate variability in duration because it
316 cannot capture high frequency variations in annual-layer thickness. Interpolation can also
317 artificially shorten or lengthen the duration of climate events, making them appear more or less
318 abrupt. The effect can be large for linear interpolation when the events occur at the beginning or
319 end of an interval during which the actual annual-layer thicknesses varied (e.g. 15 to 18 kyr at
320 WAIS Divide, Figure 3). An additional issue with linear interpolation is when a climate event
321 begins before a tie point and ends after. For instance, the annual-layer thicknesses increase from

322   3 cm for ages older than the 17.8 kyr tie point to 6 cm for ages younger (Figure 3). For equally
323   spaced measurements in depth, twice as much time is packed between measurements on the
324   older side of the tie point than between measurements on the younger side of the tie point.
325   Therefore, features just older than 17.8 kyr will have twice the duration as features just younger.
326   This may influence detection of times of significant change by artificially altering the rate of
327   change of a climate proxy.
328
329
330   *Age Bias due to Interpolation*
331   The choice of interpolation method can also bias the average age of the timescale. Understanding
332   the magnitude of potential bias is relevant for analyses of the phasing of climate proxies from
333   different ice cores, such as between a composite Antarctic temperature record from many cores
334   and a carbon dioxide record measured in a single core (e.g. Pedro et al., 2012). ACCUM and
335   ALT produce ages that are older than WDC06A-7 about as often as they are younger (Figure 4);
336   however, the linear interpolation is nearly always older (84% of the time). This occurs because
337   the layer thickness is predominantly decreasing with age due to thinning from ice flow. The
338   constant annual-layer thicknesses between tie points resulting from linear interpolation cause the
339   annual layers to be too thin near the younger tie point and therefore put too much time into the
340   younger half of the depth interval. The situation reverses in the older half of the interval, but
341   these layers are still too old at each depth, recovering the correct age only at the bottom of the
342   interval. Therefore, the linear interpolation is too old for the entire interval. For WDC06A-7, the
343   average bias is 55 years for the timescale as a whole (Table 2).
344
345   The bias due to interpolation tends to be larger for time periods that contain fewer tie points
346   because there are fewer opportunities for older and younger age differences to cancel out (Table
347   2). The bias is greatest for linear interpolation during periods with large variations in annual-
348   layer thicknesses. For instance, the increasing annual-layer thicknesses of the deglacial transition
349   (21 to 12 kyr) result in ages biased 200 years too old for linear interpolation. In contrast, the
350   ACCUM bias increases to three decades and the ALT bias is negligible (Table 2). The magnitude
351   of the linear interpolation bias is similar to the 0-400 year lead of Antarctic temperature to
352   carbon dioxide found by Pedro et al. (2012). Understanding the potential biases in the ice-core
353   timescales used in analyses like this is important to further refine phase relationships.
354
355
356   *Comparison of ALT with timescales for EDML*
357   We compare three published timescales for EDML with an interpolation using ALT. The three
358   timescales are: AICC2012 (Veres et al. 2013); LD2010 (Lemieux-Dudon et al. 2010); EDML1
359   (Parrenin et al., 2007). To derive the ALT timescale, we use the ice ages at times of distinctive
360   methane features from the AICC2012 timescale (Table 3) as well as a few tie points in the
361   Holocene. The annual-layer thickness profile from AICC2012 and ALT are shown in Figure 6A.
362   For most of the timescale, annual-layer thicknesses agree closely, and the age differences are less
363   than 100 years (Figure 6B). The largest difference occurs between 12.8 and 9.2 kyr, when ALT
364   does not produce thick annual layers around 11.5 kyr. The thick layers in the AICC2012 are
365   driven by high isotope values at the Antarctic Isotope Maximum 0 peak.
366
367   < Table 3>

368
369 Annual-layer thickness profiles from the EDML 1 and LD2010 timescales are also shown in
370 Figure 6A. These two timescales use the same tie points as AICC2012 for ages older than 12.8
371 kyr (ice age), but ages younger than 11.5 kyr (ice age) in AICC2012 are based on sulfur matches
372 with the North Greenland ice core (Veres et al., 2013). Overall, the variation in annual-layer
373 thickness between ALT and AICC2012 is about the same as among the three EDML timescales.
374 The largest difference occurs between 7.2 and 8 kyr when the annual-layer thicknesses for
375 LD2010 decrease 25% while the other interpolations show little change. Although the
376 smoothness requirement causes ALT to miss high-frequency structure in layer-thickness profiles,
377 it avoids creating large variations that may not be real.
378
379 Age differences between ALT and EDML1 and LD2010 are not shown because the age of the tie
380 points do not match those of AICC2012; thus an age comparison is not informative about the
381 interpolation method. The similarity of the annual-layer thickness profiles among the four
382 timescales suggests that both the Bayesian inverse and ALT methods produce robust timescales
383 for EDML.
384
385
386 **Application**
387 *Application to the Byrd, Siple Dome, and Law Dome ice-core timescales*
388 Comparison of interpolation methods with the annually resolved WDC06A-7 timescale indicates
389 that linear interpolation can lead to large age differences. ALT and ACCUM performed
390 substantially better. Here we assess three timescales that are based on near-linear interpolations:
391 Byrd, Siple Dome, and Law Dome. We use ALT because it does not require any assumptions
392 about ice flow. Ages of tie points for each timescale are derived from the original timescales
393 either directly from the stated tie points or indirectly from the abrupt variations in annual-layer
394 thickness (Table 4). We do not consider Taylor Dome because of the large uncertainty of the tie
395 points (Mulvaney et al., 2000). For Taylor Dome, improving only the interpolation is unlikely to
396 yield insight into the climate history.
397
398 Annual-layer thickness profiles are shown in Figure 7A, C, E for Byrd, Siple Dome, and Law
399 Dome respectively. All of the timescales have abrupt changes in annual-layer thickness at tie
400 points, similar to the linear interpolation of WAIS Divide presented in Figure 3, but also
401 structure due to the specifics of the timescale construction. The Byrd gas timescale was first
402 developed based on a Monte-Carlo method that maximized the correlation between methane
403 records (Blunier and Brook, 2001). The ice timescale was then derived by adding the delta-age,
404 calculated from accumulation and temperature estimates based on the stable-isotope values.
405 High-frequency variations in annual-layer thicknesses in the ice timescale result from time-
406 varying delta-age values. The Siple Dome gas timescale was derived by matching the methane
407 record to the Greenland methane composite record at distinct tie points then linearly
408 interpolating between the tie points (Brook et al., 2005). High frequency variations in annual-
409 layer thickness result of different delta-age values. The Law Dome timescale was developed
410 using a Dansgaard-Johnsen (1969) ice-flow model to calculate layer thinning between the tie
411 points (Pedro et al. 2011), which is almost equivalent to interpolating linearly between tie points
412 (see Fig. 7E).
413

414 We have re-interpolated the three timescales with ALT. While most of the tie points in the
415 original timescales were used, Byrd and Siple Dome required a few exceptions: we used only
416 one, instead of two, tie points at 24 kyr, 27.5 kyr and 29 kyr (Dansgaard-Oeschger events 2, 3
417 and 4) to avoid inferring large, unrealistic variations in layer thickness over short periods.
418
419 ALT annual-layer thickness profiles are shown in red in Figs. 7A, C, E. Age differences between
420 the original near-linear interpolations and ALT are shown in black. All three timescales show
421 significant age differences. The largest differences are in the Siple Dome timescale; ages shift by
422 as much as 1200 yr around 20 kyr, which is within the estimated 2000 yr uncertainty for the
423 timing of the abrupt isotope change ~22 kyr (Brook et al., 2005). For Byrd, age differences are
424 up to 1000 yr at about 24 kyr. At both Siple Dome and Byrd, changes in the timescales more
425 recent than 18 kyr are less than 200 years. The timescales have a tie point at the onset of the
426 deglacial methane rise (~18 kyr) such that the largest time interval between tie points is ~3000
427 years, which limits how much the timescales can diverge. At Law Dome, the timescale ends at
428 21 kyr. There is no tie point at the onset of the deglacial rise (~18 kyr), which results in a
429 relatively long span, 16.2 to 19.1 kyr, without a tie point during the onset of the glacial-
430 interglacial transition. The average annual-layer thickness decreases by a factor of 2 between the
431 16.2 and 19.2 kyr tie points, which results in a large age discrepancy of over 500 years centered
432 at 17.7 kyr. As shown with the WDC06A-7 timescale, linear or near-linear interpolation
433 performs poorly when the annual-layer thicknesses change significantly between tie points.
434
435 Stable-isotope records are shown in Figure 7B, D, F on the original (blue) and ALT (red)
436 timescales. For Byrd, the most significant change is that Antarctic Isotope Maximum 2 (~24 kyr)
437 becomes more compact and similar in character of the WAIS Divide and EDML records (EPICA
438 Members, 2006; WAIS Divide Project Members, 2013). Changes in the glacial-interglacial
439 transition part of the record are smaller, although ages during the Antarctic Cold Reversal are
440 shifted up to 150 years. For Siple Dome, the 3‰ $\delta^{18}O$ increase is shifted younger by 1200 years
441 from 21.8 to 20.6 kyr. As with Byrd, the changes during the glacial-interglacial transition are
442 smaller but up to 250 years at 17.5 kyr. For Law Dome, the largest shift is centered at 17.5 kyr,
443 which is the onset of deglacial warming. The deglacial transition at Law Dome is examined in
444 more detail below.
445
446 Age differences between the near-linear interpolation and ALT indicate that linear interpolation
447 consistently yields older ages during the deglacial transition. Except for a few short periods, the
448 ALT timescales are younger between 21 and 12 kyr. The bias towards older ages using a linear
449 interpolation occurs because annual layers are too thin on the younger side of an interval during
450 times of decreasing (in age) accumulation rates. On average, the linear timescales are too old by
451 40 years for Byrd, 240 years for Siple Dome, and 150 years for Law Dome.
452
453 We cannot verify whether the ages produced by ALT are more accurate than the original
454 timescales but the ALT timescales are valid alternative timescales. The large differences in the
455 timescales due to the chosen interpolation method highlight the increased uncertainty in the
456 timescale away from the tie points. Caution is needed when interpreting climate changes based
457 on interpolated timescales.
458
459 *Example: Glacial-Interglacial Transition at Law Dome*

The deglacial warming at Law Dome is marked by a rapid increase of 3‰ δ^{18}O in ~500 years. The timing of the onset was determined to be 17.84±0.32 kyr (Pedro et al., 2011) on the original timescale (blue in Figure 8); the blue vertical line marks the onset and the blue shading shows the stated uncertainty. Figure 8 also shows the same stable-isotope record on the ALT timescale. The onset of deglacial warming is shifted 550 years younger to 17.29 kyr. The large age difference occurs because this climate feature occurs nearly midway between tie points and the annual-layer thickness changes by a factor of 2 throughout the interval.

For this climate feature, the uncertainty of the linear interpolation exceeds the stated uncertainty of the Δage and correlation uncertainties at the tie points. Both the timing of the climate feature and stated uncertainty should be revised. Using the rates of accumulating uncertainty described above, the uncertainty with a linear interpolation is 31 years per hundred (Figure 5), which yields a total uncertainty of 830 years which is the 320 year stated uncertainty plus an interpolation uncertainty of 510 (0.31×1640) years from the closest tie point. In the ALT timescale, the onset of deglacial warming begins at 17.29 kyr and the total uncertainty would be 430 years, the 320 yr stated uncertainty and 110 (0.1×1100) years interpolation uncertainty. The distance to the closest tie point changes with the interpolation method which affects the magnitude of the interpolation uncertainty. This reinforces that the uncertainties are estimates and should not be interpreted as a precise quantification of the total age uncertainty.

A second effect is that the duration of events is different among the interpolation schemes. This is illustrated by the circled data in Figure 8; the duration of the cooling beginning at 16.6 kyr on the linear timescale is nearly twice as long as the cooling on the ALT timescale. Statistical tests identifying times of significant change will be affected by these timescale issues (e.g. Pedro et al., 2011; WAIS Divide Project Members, 2013).

Conclusion
Three methods for interpolating between age markers were tested using the annually resolved timescale for the WAIS Divide ice core (WDC06A-7). Linear interpolation results in unrealistic variations in annual-layer thicknesses at tie points, causing both large age errors and abrupt apparent variations in the duration of climate events. In addition, the linear interpolation resulted in a bias to older ages. The mismatch improved using interpolations based on either the smoothest annual-layer thickness (ALT) or smoothest accumulation-rate history (ACCUM). ALT performed slightly better than ACCUM but both give sufficiently similar results such that the choice of which to use will depend on the application. If only a timescale is desired, ALT is simpler to implement, but if accumulation-rate estimates are desired, for instance to help constrain the delta-age, then ACCUM is required. The rate of accumulating uncertainty between tie points using ALT was 10 years per hundred years, compared to 31 years per hundred years for linear interpolation.

The existing Byrd, Siple Dome, and Law Dome timescales were based on near-linear interpolation. Re-interpolation of these timescales using ALT and similar tie points produced timescales that were on average younger during the glacial-interglacial transition. For Siple Dome, the abrupt 3‰ increase in δ^{18}O at ~22 kyr (Taylor et al., 2004) was shifted 1200 years younger; while the timing of this event has significant uncertainty due to the accuracy of the

506 methane tie points, the large shift in age due to interpolation indicates that caution should be
507 exercised when using the Siple Dome record in analyses of the onset of Antarctic deglacial
508 warming. At ages between tie points, the interpolation uncertainty can exceed uncertainty at the
509 tie points. For Law Dome, the timing of the onset of deglacial warming is shifted by 540 years
510 indicating that the interpolation uncertainty is nearly double the stated 320 years which was
511 determined from the tie point uncertainty (Pedro et al., 2011). Uncertainty in interpolation is
512 often omitted in analyses; it should be considered when determining the timing and duration of
513 climate features in Antarctic ice-core records.
514
515

516 **Appendix A**
517 *Inverse Solution Procedure*
518 We use a Gauss-Newton iterative procedure (Aster et al., 2005, Section 10.1; Ganse, 2013) to
519 find the model that optimizes the performance index in equation 1. This is a steepest descent
520 (gradient) solver that uses the linear relationship between the model perturbations and the data
521 residuals:

522 $$\Delta \boldsymbol{m} = (\boldsymbol{J}^T\boldsymbol{J} + v^2\boldsymbol{L}^T\boldsymbol{L})^{-1}\left(-\boldsymbol{J}^T\left(\frac{G(\boldsymbol{m}^k)-\boldsymbol{d}}{\sigma}\right) - v^2\boldsymbol{L}^T\boldsymbol{L}\boldsymbol{m}^k\right) \qquad (A1)$$

523 where
524 $J = \frac{\partial G(m)}{\partial m_j}$ is evaluated numerically using a forward difference scheme and k is the iteration
525 number.
526

527 A challenge when using non-linear gradient techniques is that a local rather than a global
528 minimum of the performance index may be identified. Lundin et al. (in prep.) showed that there
529 is a unique solution for a linear formulation of some interpolation problems. For the non-linear
530 technique, we test for the existence of multiple minima using a multistart test (Aster et al., 2005;
531 Section 9.4) to identify if the solution depends upon the initial assumption. Tests of a wide range
532 of initial values did not reveal other solutions. Another potential limitation of this solution
533 technique is that the function evaluation – the forward model – must have sufficient numerical
534 accuracy to calculate the derivatives. Tests showed the numerical accuracy was sufficient.
535

536 One implementation challenge is that the initial update to the model (accumulation rate) can
537 result in negative accumulation rates. If negative accumulation rates persist, the forward model
538 does not produce a depth-age relationship, and the solution procedure fails. This is avoided by
539 initiating the model with reasonable accumulation rates based on the modern accumulation rate
540 at the site. Reducing the size of model perturbations at each iteration step, resulting in longer
541 convergence times, also solves this problem.
542
543

544 **Appendix B**
545 *Comparison of ACCUM and ALT*
546 The thickness of an annual layer of age A, $\lambda(A)$, is related to its thickness when it was deposited
547 (the accumulation rate at that time), $\dot{b}(A)$, by the thinning function, $\Lambda(A)$
548 $$\lambda(A) = \Lambda(A)\dot{b}(A) \qquad (A2)$$
549 ACCUM minimizes the second derivative of the accumulation rate:

550 $$\frac{\partial^2 \dot{b}(A)}{\partial A^2}$$ (A3)

551 ALT minimizes the second derivative of the annual-layer thickness:

552 $$\frac{\partial^2 \lambda(A)}{\partial A^2} = \frac{\partial^2 \Lambda(A)}{\partial A^2}\dot{b}(A) + 2\frac{\partial \Lambda(A)}{\partial A}\frac{\partial \dot{b}(A)}{\partial A} + \Lambda(A)\frac{\partial^2 \dot{b}(A)}{\partial A^2}$$ (A4)

553

554 Figure A1 shows relative values for the three terms on the right hand side of Eq. (A4) evaluated
555 for ACCUM as a function of age on the WDC06A-7 timescale. ALT does not use a thinning
556 function or an accumulation history so the relative contributions from the three terms cannot be
557 evaluated for ALT. The third term, which includes the second derivative of the accumulation
558 rate, accounts for 70% of the curvature of λ(A) and explains why ALT and ACCUM yield
559 similar, but not identical, interpolations. The second derivative of the accumulation rate is
560 multiplied by the thinning function; because the thinning function is unity at the surface, ALT
561 emphasizes minimizing the curvature of the younger accumulation rates relative to ACCUM.
562
563 The first and second terms both account for 15% of the total. The first term is the second
564 derivative of the thinning function weighted by the accumulation rate. Hence ALT will minimize
565 the thinning function with added emphasis when the accumulation rate is higher, such as in the
566 mid-Holocene for WAIS Divide. The second derivative of the thinning function is also indirectly
567 controlled by variations in accumulation rate because a major cause of variations in the thinning
568 function is the change in accumulation rate. The second term, with the two first derivatives, has a
569 similar structure to the first term. The largest age difference between ALT and ACCUM is in the
570 18 to 24 kyr interval. Interestingly, this interval has near zero values for both the first and second
571 terms making it difficult to explain why the ALT and ACCUM differ during this period. The
572 difference is likely related to weighting of the second derivative of the accumulation rate by the
573 thinning function in the first term which deemphasizes the smoothness constraint during this
574 period in ALT.
575
576 It is not clear that ALT has a predictive advantage to ACCUM, or whether the slightly better
577 performance at WAIS Divide is due to chance. There is no obvious reason why minimizing the
578 curvature of the thinning function would lead to improved predictive capability. While this is an
579 area that could be further explored, the small differences between the ALT and ACCUM method
580 indicate that there will be little improvement in the final timescale. The choice of whether to use
581 ALT or ACCUM will most likely depend on the application. If only a timescale is desired, ALT
582 is simpler to implement. If accumulation rate estimates are desired, for instance to help constrain
583 the delta-age, then ACCUM is required.
584
585

591 **References**
592 Alley, R.B., and 11 others: Visual-stratigraphic dating of the GISP2 ice core: Basis,
593   reproducibility, and application. *Journal of Geophysical Research-Oceans*, 102(C12): 26367-
594   26381, 1997.
595 Aster, R., Borchers, B., and Thurber, C.: Parameter Estimation and Inverse Problems. Elsevier
596   Academic Press. 2005.
597 Bazin, L. and 21 others: An optimized multi-proxy, multi-site Antarctic ice and gas orbital
598   chronology (AICC2012): 120-800 ka, Clim. Past, 9, 1715-1731, 2013.
599 Blunier, T. and Brook, E.J.: Timing of millennial-scale climate change in Antarctica and
600   Greenland during the last glacial period. *Science*, 291(5501): 109-112, 2001.
601 Blunier, T., Chappellaz, J., Schwander, J., Dallenbach, A., Stauffer, B., Stocker, T.F., Raynaud,
602   D., Jouzel, J., Clausen, H.B., Hammer, C.U., and Johnsen, S.J.: Asynchrony of Antarctic and
603   Greenland climate change during the last glacial period. *Nature*, 394(6695): 739-743, 1998.
604 Blunier, T., Spahni, R., Barnola, J.M., Chappellaz, J., Loulergue, L., and Schwander, J.:
605   Synchronization of ice core records via atmospheric gases. *Climate of the Past*, 3(2): 325-
606   330, 2007.
607 Brook, E.J., White, J.W.C., Schilla, A.S.M., Bender, M.L., Barnett, B., Severinghaus, J.P.,
608   Taylor, K.C., Alley, R.B., and Steig, E.J.: Timing of millennial-scale climate change at Siple
609   Dome, West Antarctica, during the last glacial period. *Quaternary Science Reviews*, 24(12-
610   13): 1333-1343, 2005.
611 Conway, H., Hall, B. L., Denton, G.H., Gades, A.M., and Waddington, E.D.: Past and future
612   grounding-line retreat of the West Antarctic Ice Sheet, Science, 286, 280-283, 1999.
613 Dahl-Jensen, D., Gundestrup, N., Gogineni, S.P., and Miller, H.: Basal melt at NorthGRIP
614   modeled from borehole, ice-core and radio-echo sounder observations. *Annals of Glaciology,
615   Vol 37*, 37: 207-212, 2003.
616 Dansgaard, W. and Johnsen, S.J.: A flow model and a time scale for the ice core from Camp
617   Century, Greenland. *Journal of Glaciology*, 8(53): 215-223, 1969.
618 Dreyfus, G.B., Parrenin, F., Lemieux-Dudon, B., Durand, G., Masson-Delmotte, V., Jouzel, J.,
619   Barnola, J.M., Panno, L., Spahni, R., Tisserand, A., Siegenthaler, U., and Leuenberger, M.:
620   Anomalous flow below 2700 m in the EPICA Dome C ice core detected using delta O-18 of
621   atmospheric oxygen measurements. *Climate of the Past*, 3(2): 341-353, 2007.
622 EPICA Members: One-to-one coupling of glacial climate variability in Greenland and
623   Antarctica. *Nature*, 444(7116): 195-198, 2006.
624 Ganse, A. 2013. Helpful tips on inverse theory. http://staff.washington.edu/aganse/invresources/.
625 Grootes, P.M., Stuiver, M., White, J.W.C., Johnsen, S. and Jouzel, J.: Comparison of oxygen-
626   isotope records from the GISP2 and GRIP Greenland ice cores. *Nature*, 366(6455): 552-554,
627   1993.
628 Lemieux-Dudon, B., Blayo, E., Petit, J.R., Waelbroeck, C., Svensson, A., Ritz, C., Barnola, J.M.,
629   Narcisi, B.M., and Parrenin, F.: Consistent dating for Antarctic and Greenland ice cores.
630   *Quaternary Science Reviews*, 29(1-2): 8-20, 2010.
631 Lundin, J. (2012). *Self-consistent modeling of ice-sheet evolution and paleoclimate.* PhD thesis.
632   University of Washington.
633   https://digital.lib.washington.edu/researchworks/handle/1773/20276
634 Lundin, J.M.D., Waddington, E.D., Conway, H., Adams, L., Fudge, T.J., and Brook, E.J.: Ice-
635   core depth-age relationships from sparse data using inverse methods. In preparation for
636   Journal of Glaciology.

637   Meese, D.A., Gow, A.J., Alley, R.B., Zielinski, G.A., Grootes, P.M., Ram, M., Taylor, K.C.,
638   Mayewski, P.A., and Bolzan, J.F.: The Greenland Ice Sheet Project 2 depth-age scale:
639   Methods and results. *Journal of Geophysical Research-Oceans*, 102(C12): 26411-26423,
640   1997.
641   Monnin, E., and 12 others: Evidence for substantial accumulation rate variability in Antarctica
642   during the Holocene, through synchronizations of CO_2 in the Taylor Dome, Dome C and
643   DML ice cores. *Earth and Planetary Science Letters*, 224, 45-54, 2004.
644   Mulvaney, R., Rothlisberger, R., Wolff, E.W., Sommer, S., Schwander, J., Hutteli, M.A. and
645   Jouzel, J.: The transition from the last glacial period in inland and near-coastal Antarctica.
646   *Geophysical Research Letters*, 27(17): 2673-2676, 2000.
647   Parrenin, F., and 27 others: The EDC3 chronology for the EPICA dome C ice core. *Climate of*
648   *the Past*, 3(3): 485-497, 2007.
649   Pedro, J.B., Rasmussen, S.O., and van Ommen, T.D.: Tightened constraints on the time-lag
650   between Antarctic temperature and CO2 during the last deglaciation. *Climate of the Past*,
651   8(4): 1213-1221, 2012.
652   Pedro, J.B., van Ommen, T.D., Rasmussen, S.O., Morgan, V.I., Chappellaz, J., Moy, A.D.,
653   Masson-Delmotte, V. and Delmotte, M.: The last deglaciation: timing the bipolar seesaw.
654   *Climate of the Past*, 7(2): 671-683, 2011.
655   Petit, J.R., and 18 others: Climate and atmospheric history of the past 420,000 years from the
656   Vostok ice core, Antarctica. *Nature*, 399, 429-436, 1999.
657   Price, S.F., Conway, H., and Waddington, E.D.: Evidence for late pleistocene thinning of Siple
658   Dome, West Antarctica. *Journal of Geophysical Research-Earth Surface*, 112(F3), 2007.
659   Raisbeck, G.M., Yiou, F., Jouzel, J. and Stocker, T.F.: Direct north-south synchronization of
660   abrupt climate change record in ice cores using Beryllium 10. *Climate of the Past*, 3(3): 541-
661   547, 2007.
662   Raymond, C.F., Deformation in the vicinity of ice divides, *J. Glaciol.*, 29(103), 357-373, 1983.
663   Ruth, U., and 19 others: "EDML1": a chronology for the EPICA deep ice core from Dronning
664   Maud Land, Antarctica, over the last 150 000 years. *Climate of the Past*, 3(3): 475-484,
665   2007.
666   Sigl, M., and 11 others: A new bipolar ice core record of volcanism from WAIS Divide and
667   NEEM and implications for climate forcing of the last 2000 years. *Journal of Geophysical*
668   *Research-Atmospheres*, 118(3): 1151-1169, 2013.
669   Steen-Larsen, H.C., Waddington, E.D., and Koutnik, M.R.: Formulating an inverse problem to
670   infer the accumulation-rate pattern from deep internal layering in an ice sheet using a Monte
671   Carlo approach. *Journal of Glaciology*, 56(196): 318-332, 2010.
672   Steig, E.J., Brook, E.J., White, J.W.C., Sucher, C.M., Bender, M.L., Lehman, S.J., Morse, D.L.,
673   Waddington, E.D., and Clow, G.D.: Synchronous climate changes in Antarctica and the
674   North Atlantic. *Science*, 282(5386): 92-95, 1998.
675   Stenni, B., and 39 others: Expression of the bipolar see-saw in Antarctic climate records during
676   the last deglaciation. *Nature Geoscience*, 4(1): 46-49, 2011.
677   Svensson, A., and 14 others: A 60 000 year Greenland stratigraphic ice core chronology. *Climate*
678   *of the Past*, 4(1): 47-57, 2008.
679   Svensson, A., and 25 others: Direct linking of Greenland and Antarctic ice cores at the Toba
680   eruption (74 ka BP). *Climate of the Past*, 9(2): 749-766, 2013.
681   Taylor, K. C., and 13 others: Abrupt climate change around 22 ka on the Siple Coast of
682   Antarctica. *Quaternary Science Reviews*, 23, 7-15, 2004.

683 van Ommen, T.D., Morgan, V., and Curran, M.A.J.: Deglacial and Holocene changes in
684   accumulation at Law Dome, East Antarctica. *Annals of Glaciology,* **39**, 359-365, 2004.
685 Veres, D. and 15 others: The Antarctic ice core chronology (AICC2012): an optimized multi-
686   parameter and multi-site dating approach for the last 120 thousand years, *Climate of the Past*,
687   9, 1733-1748, 2013.
688 Waddington, E.D., Brook, E., Morse, D.L., Conway, H., Barnett, B., and Taylor, K.C.:
689   Interpolation of sparse depth-age data in ice cores, and inference of accumulation-rate history:
690   an inverse approach. *7th International Symposium on Antarctic Glaciology (ISAG 7),* Milano
691   August 25-29, 2003.
692 Waddington, E.D., Neumann, T.A., Koutnik, M.R., Marhsall, H.-P., and D.L. Morse: Inference
693   of accumulation-rate patterns from deep layers in glaciers and ice sheets. *Journal of*
694   *Glaciology*, 53(183), 694-712, 2007.
695 WAIS Divide Project Members: Onset of deglacial warming in West Antarctica driven by local
696   orbital forcing, *Nature*, 500(7463), 440-444, 2013.
697

698 Figure 1: Commonly used methane tie points between 8 kyr and 30 kyr. Italicized match points
699 indicate less certain correlations. Greenland Composite Methane on GICC05 and EDML
700 Methane on timescale of Lemieux-Dudon et al. (2010).

701 Figure 2: Accumulation rate (top) inferred with the ACCUM method with ice flow parameters
702 for either a flank or divide site. The age difference (bottom) between the two interpolations.

703 Figure 3: 100-year running average of annual-layer thicknesses for the WDC06A-7 compared
704 with inferred annual-layer thickness for the different interpolations. Black vertical dashed lines
705 are tie points. Inset in upper left shows details of between 29.6 and 17 kyr.
706
707 Figure 4: Age differences between the interpolation methods and the WDC06A-7 timescale.
708 Yellow shading is the accumulated uncertainty of WDC06A-7 from the closest tie point (WAIS
709 Divide Project Members, 2013).
710
711 Figure 5: We define the rate of accumulating uncertainty as the absolute value of the age
712 difference between an interpolation and the WDC06A-7 timescale at each WDC06A-7 age
713 divided by the age difference from the nearest tie point. The cumulative fraction is the fraction of
714 the total data set for which the rate of accumulating uncertainty is below the threshold value on
715 the x-axis; this is similar to a cumulative distribution function. The horizontal lines indicate 0.66
716 (1-sigma) and 0.95 (2-sigma) levels.
717
718 Figure 6: A) Annual-layer thicknesses for three EDML timescales - AICC2012 (Veres et al.,
719 2013), LD2010 (Lemieux-Dudon et al., 2010), and EDML1 (Ruth et al., 2007) - and the ALT
720 interpolation based on ice ages from AICC2012. B) Age differences between AICC2012 and
721 ALT interpolation. Age differences between other timescales are not shown because only the
722 AICC2012 and ALT use the same ages for tie points. Dashed vertical lines are tie-point ages.
723
724 Figure 7: Annual-layer thicknesses of original timescales (blue) and ALT interpolation (red) in
725 A,C, and E. Age differences are shown in black. The stable-isotope records on the original (blue)
726 and ALT (red) timescales in B,D, and F. The stable-isotope records on the ALT timescales are
727 shifted down by 1‰.
728
729 Figure 8: Detail of Law Dome δ^{18}O record on the Pedro et al. (2011) timescale (blue) and on
730 ALT timescale (red and shifted down by 1‰). Black vertical dashed line is the depth-age tie
731 point. Blue vertical line and shading is the timing and uncertainty of the onset of deglacial
732 warming defined by Pedro et al. (2011). The red vertical line marks the timing of the onset of
733 deglacial warming with ALT. The blue horizontal bar is increased uncertainty by adding an
734 interpolation uncertainty appropriate for linear interpolation. The red horizontal bar is the total
735 uncertainty for the ALT timescale. See text for description of uncertainty calculations. The two
736 circled areas show the different durations of climate events that can result just from using a
737 different interpolation method. The duration of the cooling with ALT is half its duration with
738 linear interpolation.
739
740 Figure A1: The three terms from the right side of Eq. (A4) evaluated for the ACCUM
741 interpolation of WAIS Divide WDC06A-7.

Table 1: Assumed depth-age tie points used for WAIS Divide

Age (ka)	2	4	6	8.2	11.8	13	14	17.8	24	27.6	29.6	35.9
Depth (m)	481.84	916.52	1281.63	1587.90	1973.34	2082.71	2243.88	2422.60	2612.57	2730.02	2798.95	2959.00

Table 2: Interpolation Assessment for WDC06A-7

	Linear	ACCUM	ALT
Largest Age Difference (years)	374	151	118
Outside of WDC06A-7 Uncertainty*	60%	33%	25%
Age Bias (years)	-55	9	0
Deglacial Age Bias (years)	-181	30	1

* This is the percentage of interpolation ages that differ from the
   WDC06A-7 ages by more than the WDC06A-7 uncertainty at that age

Table 3: Depth-age tie points for EDML

Depth	223.72	352.06	463.51	568.94	724.06	768.88	830.09	917.56	1048.8	1153.51	1173.19	1224.53
Gas Age	2	4	6	8.2	11.7	12.8	14.7	17.4	23	28	29	32
Ice Age	2.9	4.9	7	9.2	12.8	14.1	15.8	18.8	24.5	29.4	30.5	33.5

Table 4: Depth-age tie points

Byrd	Depth	453.01	624.93	821.19	1045.54	1111.74	1193.65	1270.37	1522.8	1593.91
	Ice Age	4	6	8.3	11.6	15	18	25	29.5	33

Siple Dome	Depth	339.28	433.5	507.51	621.42	647.06	673.15	708.08	734.09	756.22	762.78	786.38
	Ice Age	4	6	8.3	11.9	12.1	15	18.3	24	27.8	28.8	32.6

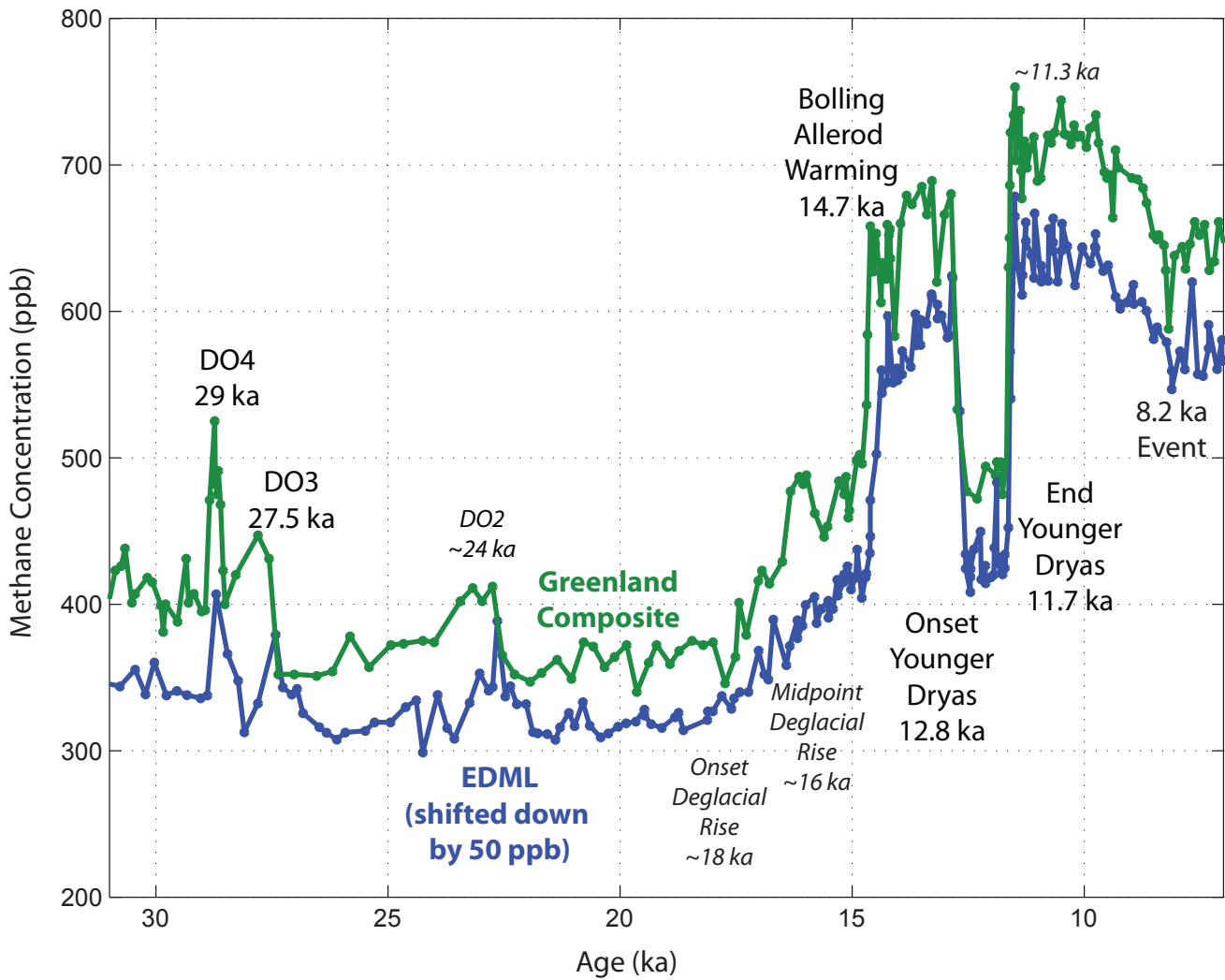| Law Dome	Depth	8	9	11.8	12.7	12.8	16.2	19.5	12	23
	Ice Age	1099.682	1106.04	1121.593	1124.423	1128.876	1131.081	1133.498	1134.273	1134.674

Figure 1: Commonly used methane tie points between 8 kyr and 30 kyr. Italicized match points indicate less certain correlations. Greenland Composite Methane on GICC05 and EDML Methane on timescale of Lemieux-Dudon et al. (2010).
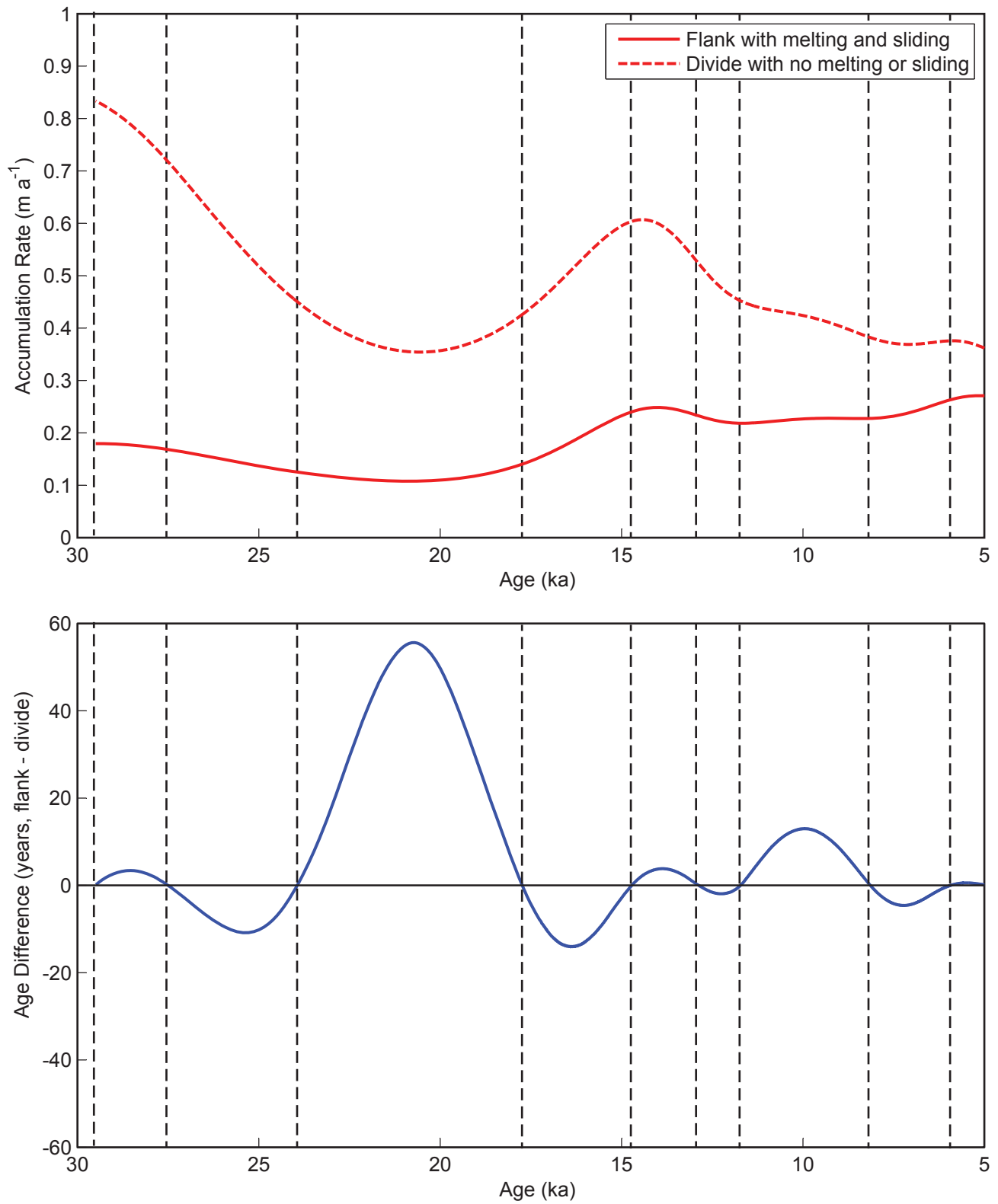
Figure 2: Accumulation rate (top) inferred with the ACCUM method with ice flow parameters for either a flank or divide site. The age difference (bottom) between the two interpolations.
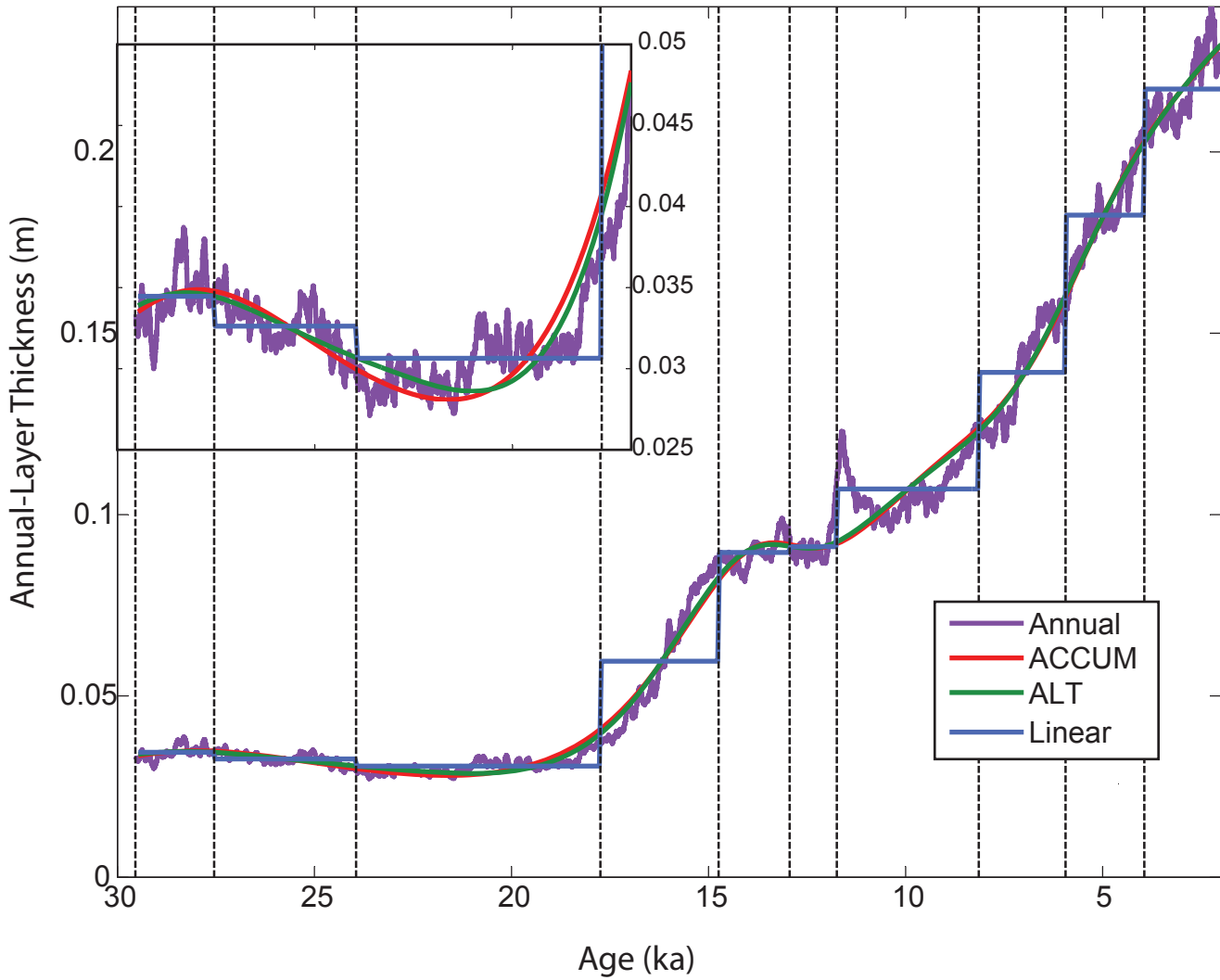
Figure 3: 100-year running average of annual-layer thicknesses for the WDC06A-7 compared with inferred annual-layer thickness for the different interpolations. Black vertical dashed lines are tie points. Inset in upper left shows details of between 29.6 and 17 kyr.
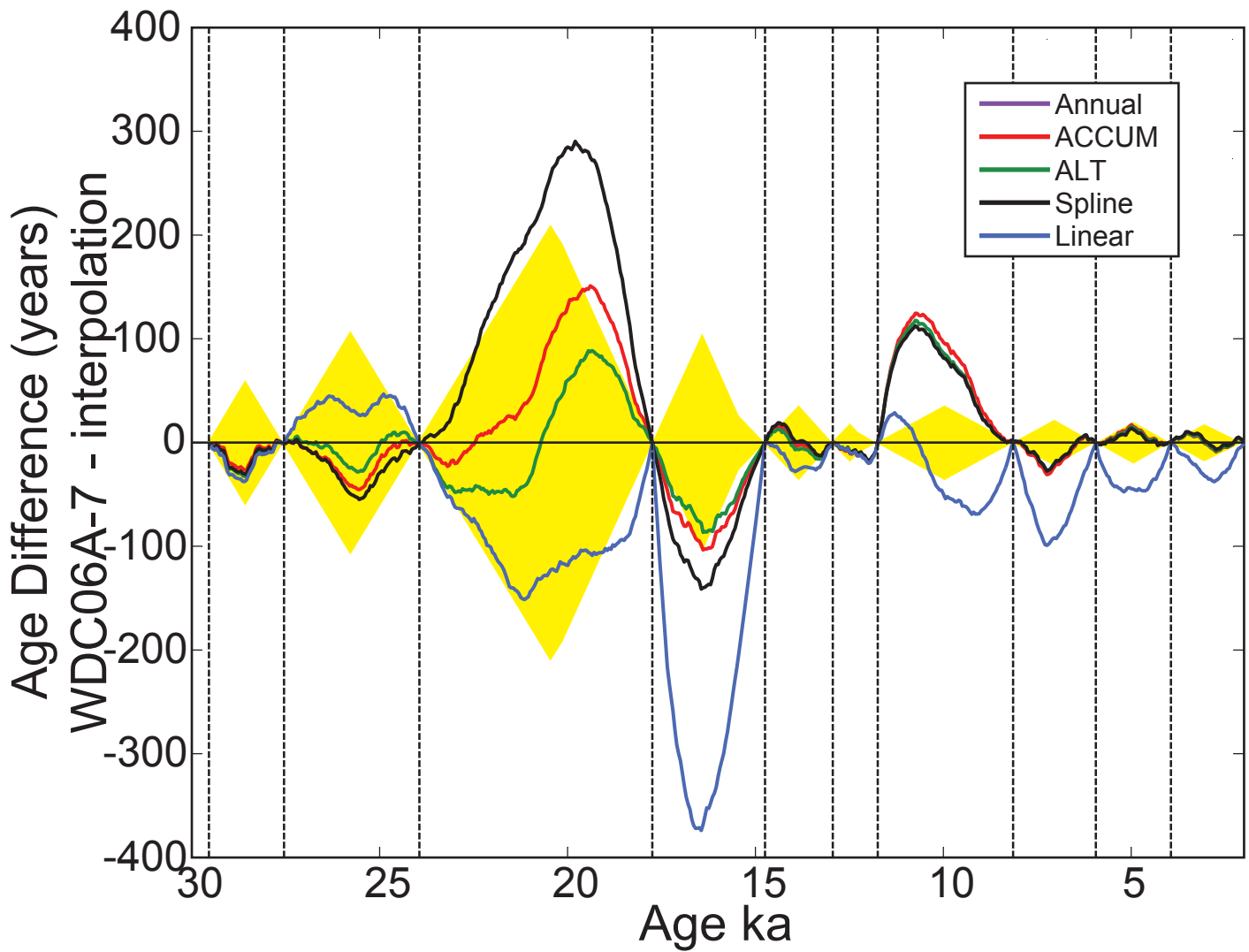
Figure 4: Age differences between the interpolation methods and the WDC06A-7 timescale. Yellow shading is the accumulated uncertainty of WDC06A-7 from the closest tie point (WAIS Divide Project Members, 2013).
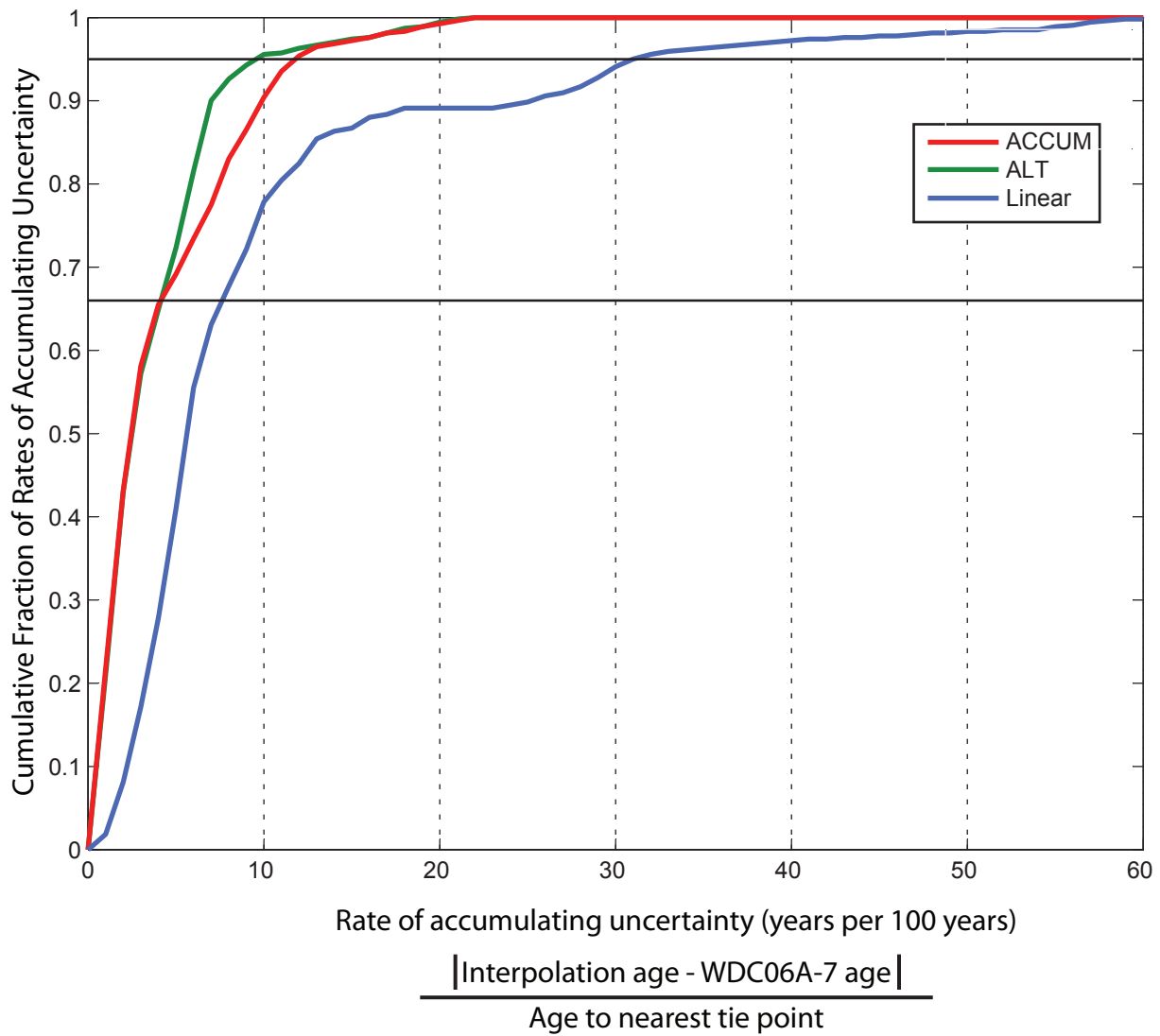
Figure 5: We define the rate of accumulating uncertainty as the absolute value of the age difference between an interpolation and the WDC06A-7 timescale at each WDC06A-7 age divided by the age difference from the nearest tie point. The cumulative fraction is the fraction of the total data set for which the rate of accumulating uncertainty is below the threshold value on the x-axis; this is similar to a cumulative distribution function. The horizontal lines indicate 0.66 (1-sigma) and 0.95 (2-sigma)
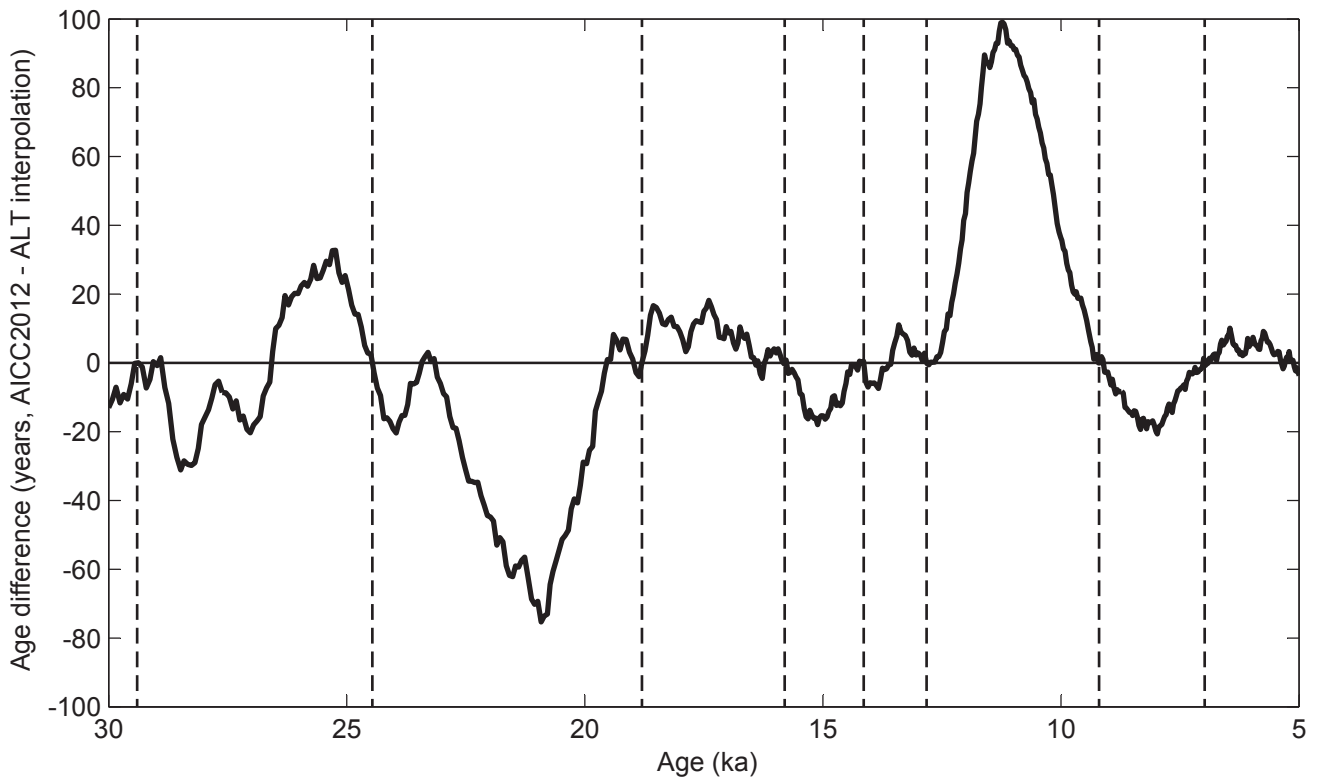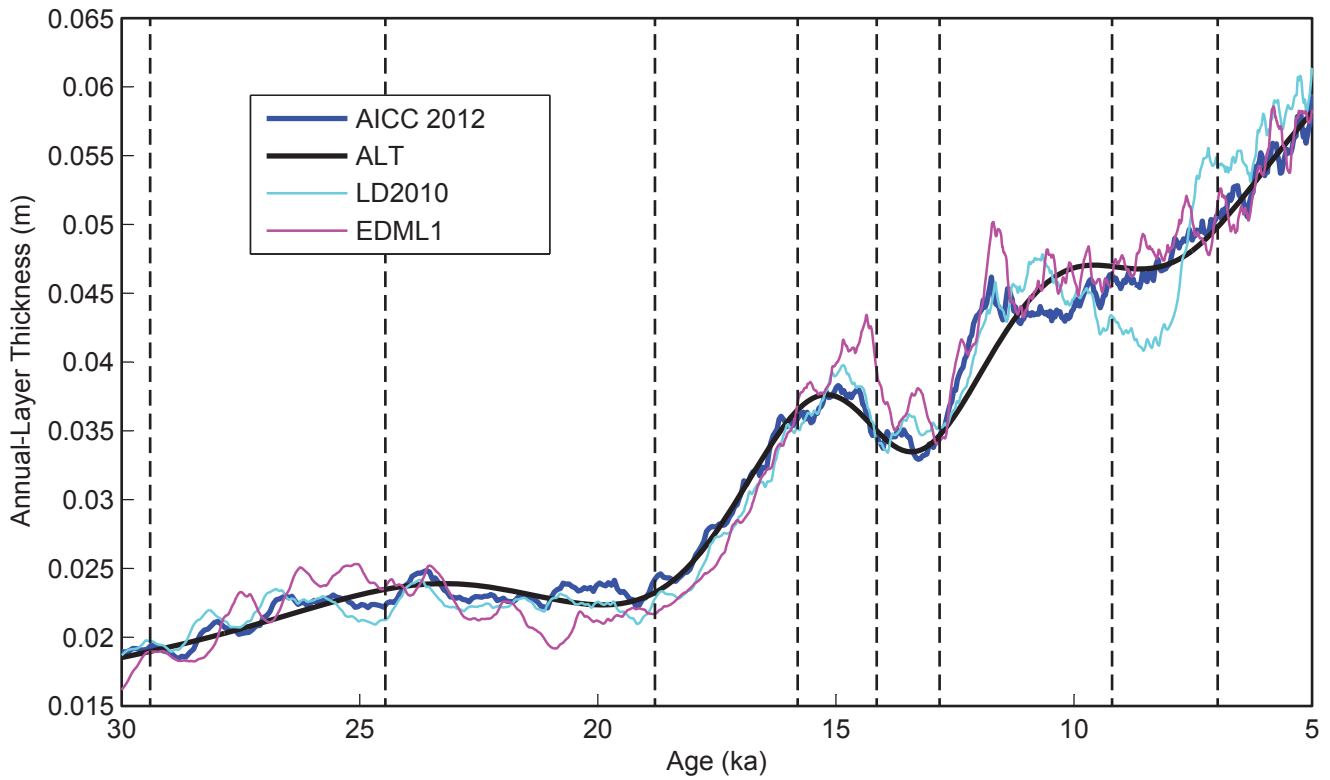
Figure 6: A) Annual-layer thicknesses for three EDML timescales - AICC2012 (Veres et al., 2013), LD2010 (Lemieux-Dudon et al., 2010), and EDML1 (Ruth et al., 2007) - and the ALT interpolation based on ice ages from AICC2012. B) Age differences between AICC2012 and ALT interpolation. Age differences between other timescales are not shown because only the AICC2012 and ALT use the same ages for tie points. Dashed vertical lines are tie-point ages.
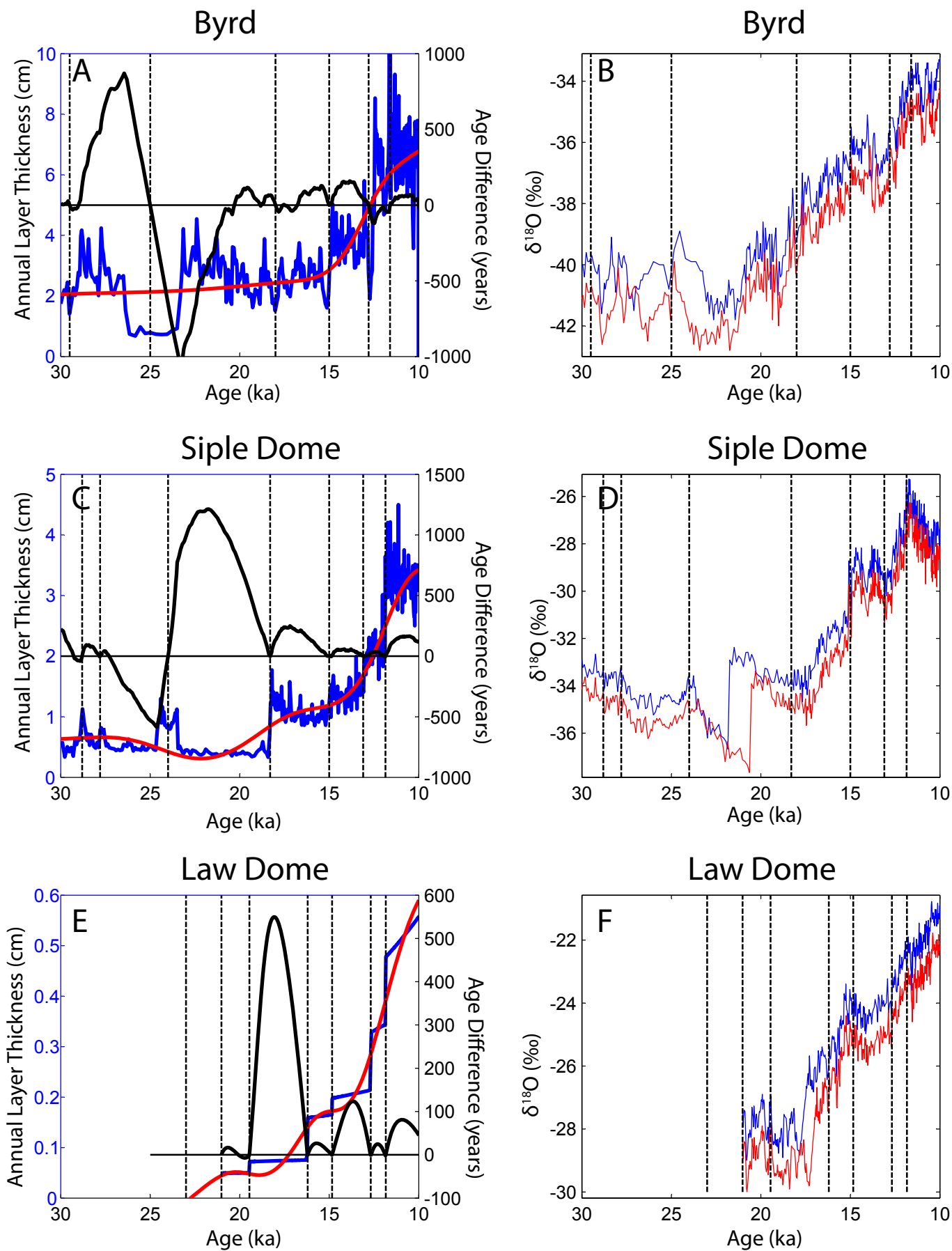
Figure 7: Annual-layer thicknesses of original timescales (blue) and ALT interpolation (red) in A,C, and E. Age differences are shown in black. The stable-isotope records on the original (blue) and ALT (red) timescales in B,D, and F. The stable-isotope records on the ALT timescales are shifted down by 1‰.
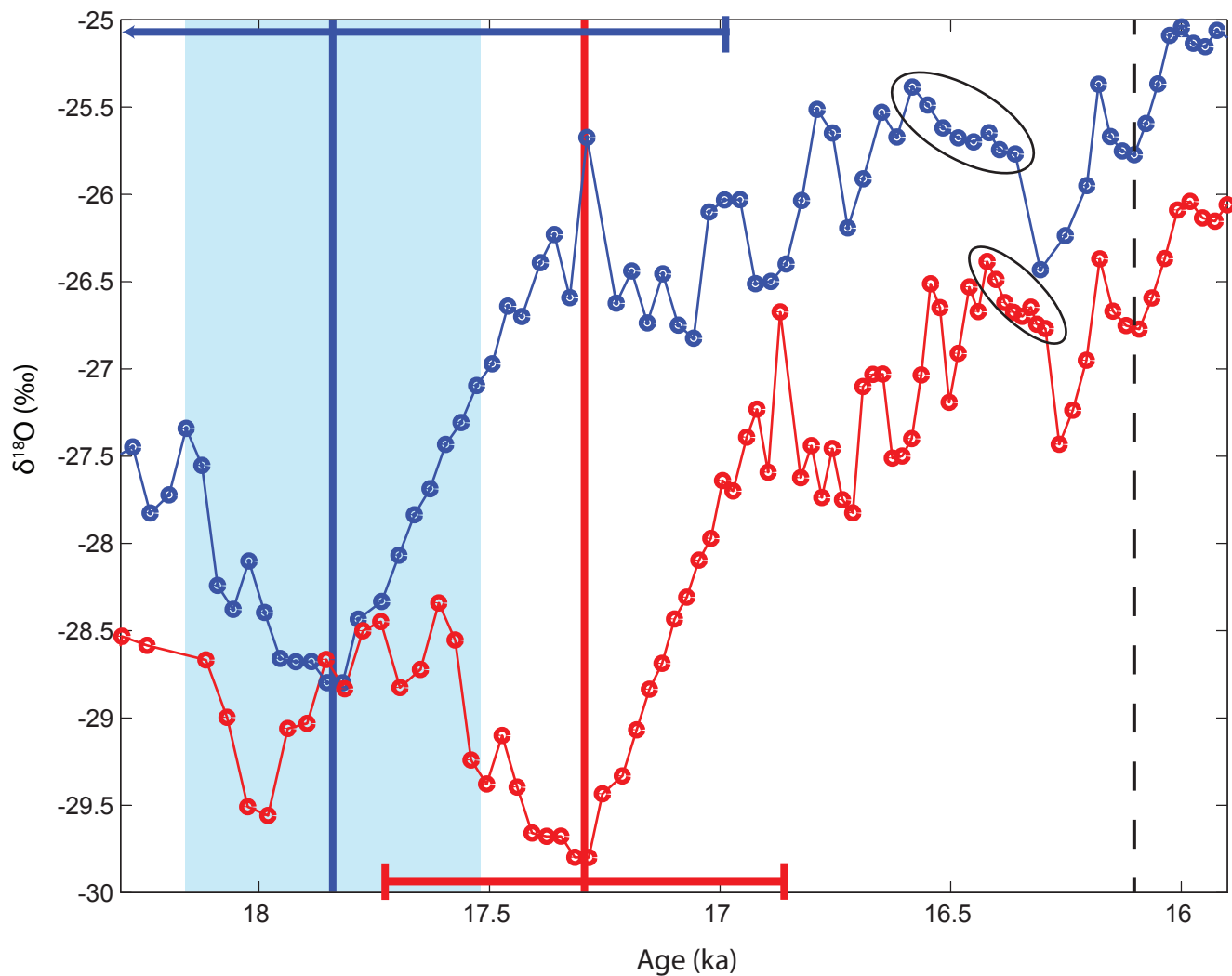
Figure 8: Detail of Law Dome δ^{18}O record on the Pedro et al. (2011) timescale (blue) and on ALT timescale (red and shifted down by 1‰). Black vertical dashed line is the depth-age tie point. Blue vertical line and shading is the timing and uncertainty of the onset of deglacial warming defined by Pedro et al. (2011). The red vertical line marks the timing of the onset of deglacial warming with ALT. The blue horizontal bar is increased uncertainty by adding an interpolation uncertainty appropriate for linear interpolation. The red horizontal bar is the total uncertainty for the ALT timescale. See text for description of uncertainty calculations. The two circled areas show the different durations of climate events that can result just from using a different interpolation method. The duration of the cooling with ALT is half its duration with linear interpolation.
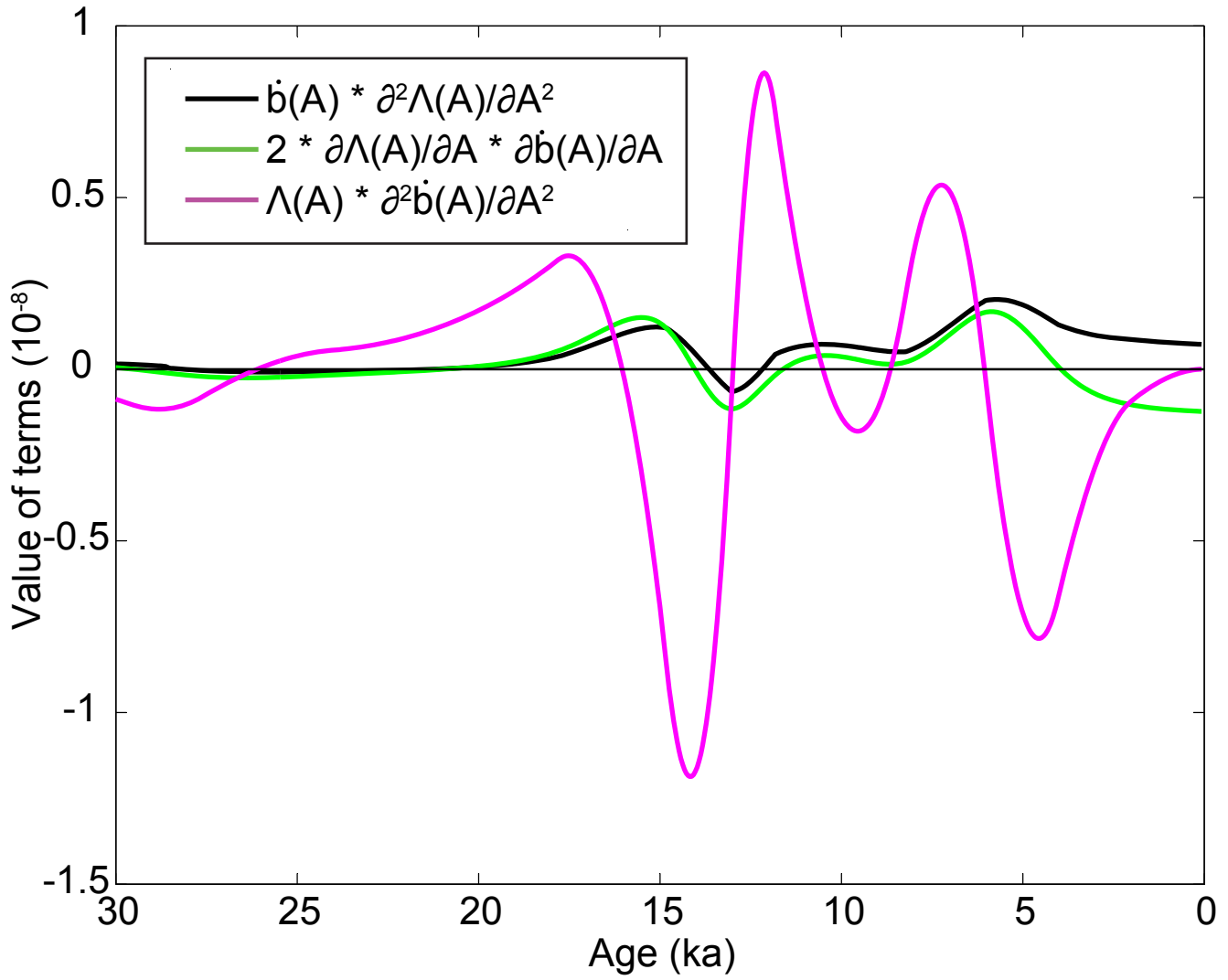
Figure A1: The three terms from the right side of Eq. (A4) evaluated for the ACCUM interpolation of WAIS Divide WDC06A-7.

Chapter 7: Future Research

This dissertation described a variety of ways of obtaining information about past ice-sheet and climate conditions. The optical properties of firn, internal layers of Thwaites Glacier, ice-core records from WAIS Divide, and interpolated timescales for coastal Antarctic ice cores are linked through a variety of themes. First, the physical properties of ice determine the different wavelengths of electromagnetic radiation to best investigate the interior structure of the ice sheet. Second, annual cycles recognizable in the ice sheet form the basis for timescales and inferred accumulation rates. Third, the topic of uncertainty features prominently in each chapter. Fourth, past variations in ice flow create challenges and opportunities in both placing modern observations in context and interpreting past climate change. The papers span a broad range of research questions but all contribute to opening many potential research avenues. This chapter is organized into three broad directions of future research. Each section discusses both ongoing work and future opportunities.

Electrical Measurements
The electrical measurements of the WAIS Divide ice core have many potential uses beyond annual layer identification. An immediate objective is to understand the loss of annual layering below 2800 m. The amplitude of the annual signal continues to decrease after 2800 m, such that by 3200 m it is absent. The variance of the AC and DC data, a measurement of the amplitude of the annual signal, is greatest during the LGM and correlates well with the dust concentration in the ice. The loss of amplitude below 2800 m is partly explained by the decrease in dust concentration, but the amplitude reduces even more than the early Holocene. This suggests that there is an additional process reducing the amplitude of the annual signal. It is unclear if this process is diffusive in nature, or whether it might indicate cm-scale mixing of layers due to ice flow. What is intriguing about the reduction in amplitude is it begins to occur where there is a change in ice fabric as measured by thin sections, sonic logging, and laser dust logging. Additionally, a common feature of ECM records was abrupt changes in the amplitude of quasi-annual variations that occurred predominantly between 2700 and 3100 m. The results were compared with physical properties at a 30 cm section at 2968 m depth. The grain size had regular layering of coarse and fine grains and showed no major differences in the region of low-amplitude in the ECM. These events will be investigated more as chemical measurements become available.

With the DC-ECM, we measured multiple tracks at different positions on the face of the ice core yielding a two-dimensional picture of the ice core. The multi-track images suggest cm-scale irregularities in layering, but are difficult to interpret because the noise level on individual tracks is relatively high. The cause of this noise is likely surface irregularities created when planing the ice surface with a mechanical planer. Attempts to plane the ice by hand with a microtome blade were disastrous, leaving me quite happy with the relatively minor ridges from the mechanical planer. It may be possible to reduce the impact of the grooves by using a slightly larger electrode. We used a smaller electrode to gain greater spatial precision in measurements to optimize the chances of resolving thin annual layers near the bed. Different electrode dimensions will be tested before the South Pole intermediate depth core is measured. Since the annual signal in the electrical conductance at South Pole is not as distinct as at WAIS Divide, it may be preferable to optimize the electrode setup for multi-track rather than annual layers.

The above discussion should not imply that there is no possibility to use the WAIS Divide multi-track data. I have collaborated with the University of Maine to investigate irregular layers observed with the multi-track measurements. Maine is developing a laser ablation system that can measure chemical

species at sub-mm spacing. Two pieces of WAIS Divide ice with irregular layers were sent to them. The laser ablation system had initial difficulties. After several tries, the laser ablation data produced roughly similar results for two tracks spaced 1 cm apart; however, while the two tracks were broadly similar, they were not at a level of precision necessary to test the irregular multi-track layering. Continued method development and more detailed measurements will allow many new analysis avenues in the future.

WAIS Divide Climate
Developing the annually resolved timescale for the WAIS Divide ice core provided the opportunity to collaborate with Eric Steig's group and lead the initial deglacial climate interpretation. The broad themes were discussed in Chapter 4, but many details remain for more specific analyses. An obvious target of specific study is the rapid accumulation increase between 12 and 11.6 ka. This was unexpected in Antarctica for two reasons: 1) the climate is thought to vary slowly due to buffering from the Southern Ocean and 2) the stable-isotope records did not show a significant change during the accumulation increase. The timing of the accumulation increase is intriguing. The relative age precision between the methane jump and the accumulation increase is about 100 years. Therefore, the onset of the accumulation increase can be confidently placed before the methane jump, but how closely the methane jump corresponds to the end of the accumulation increase is both a question of dating and of defining the end of the accumulation increase. Regardless of the exact timing, there are a variety of important questions about this event. First, is the event unique to central West Antarctica or is it more widespread? This is difficult to assess because no other Antarctic ice core has a timescale able to resolve such accumulation variations. Second, what does such an accumulation increase indicate about global climate? And why is a similar accumulation increase not observed in relation to the methane jump at the Bolling-Allerod warming? The rapid accumulation rate increase at WAIS Divide asks many tantalizingly questions that will require more observations and modeling to answer.

There are also many questions about the timing of abrupt climate change that can be addressed with the WAIS Divide records. Many of these efforts will be led by colleagues, such as the gas timescale for the deglaciation. A major question has been the timing of the onset of the deglacial carbon dioxide increase. There is considerable uncertainty on the timing of this event because the gas record must be tied to Greenland age scales. The carbon dioxide record from Dome C has an age uncertainty of at least 700 years at the onset of the deglaciation. The WAIS Divide record allows the gas records to be dated in two independent ways: 1) using the annual timescale and calculating the gas-age ice-age difference and 2) matching the methane records to Greenland records and using the gas timescale developed by annual layer counting and a calculation of the gas-age ice-age difference for the Greenland cores. The difference between two ways of dating the WAIS Divide gas records reaches only 200 years at 19 ka. The close agreement is strong evidence for robust absolute ages of the ice core timescales. Comparisons between ice-core records and other paleoclimate records are often challenging because the other records use different methods for dating (^{14}C or U/Th). This leads to large uncertainties in the ages relative to each other. The better understanding of the accuracy of the ice-core timescales will allow more precise assessment of the phasing of climate change from a wide variety of paleoclimate archives.

Other ice cores
This work with the WAIS Divide ice core has also opened up possibilities with other ice cores. A New Zealand led group has successfully drilled to bedrock at Roosevelt Island. I have been involved in this project by modeling the depth-age scales as well as giving advice on making ECM measurements. The depth-age scale for Roosevelt Island promises to yield valuable information about past ice thickness in the Eastern Ross Sea. The inverse method I developed to interpolate timescales was the first step in

building a model to infer past ice-thickness change of coastal domes. A key advantage of the non-linear solution method is that ice thickness change can also be solved for, either if the accumulation is already known (such as from bubble number density) or in conjunction with inferring the accumulation rate. The ice-core processing stopped at ~5000 years so we will have to wait another year to see what secrets the Roosevelt Island depth-age scale holds.

An intermediate core at South Pole is the next major US ice coring projecting. I will be involved in the drilling of the core as a postdoc with Eric Steig. One of the primary goals of the South Pole Ice Core is a record of trace atmospheric gases that are best preserved in the cold but relatively high accumulation setting at South Pole. Eric Saltzman and Murat Aydin will be responsible for this record. Ed and I have worked with Eric and Murat on measurements from other ice cores because they need temperature histories for the gas samples' movement through the ice sheet. The South Pole core provides an opportunity to continue this work particularly for the deeper section where the temperature history will have influenced the gas records more. There is also a need to characterize the conditions upstream of the core site because South Pole is not located at an ice divide. The modern ice flow velocity is 10 m a^{-1} indicating that ice 10,000 years old originated ~100 km upstream. There will also be an opportunity to measure the electrical properties of the ice core. Measurements I made last winter on South Pole ice from ~180 m suggests that there is not much of an annual signal in Holocene ice at South Pole in electrical conductance. However, there are four reasons to make ECM measurements: 1) the ECM measurements are an independent record needed to validate the depth registration of the continuous melt system used to analyze many chemical species; 2) the annual signal is likely more prominent in the glacial ice when the dust concentration is higher; 3) the ECM can recognized distinct volcanic events to match with other records allowing an initial timescale to be developed; and 4) multi-track measurements will help determine if there are any stratigraphic disturbances in the core due to past streaming ice flow.

There are also opportunities to dictate where future ice cores will be drilled. Hercules Dome is one potential target. Before drilling at Hercules Dome, a detailed site survey is necessary to determine the site characteristics. In particular, it is unclear if there is a Raymond bump or if the site is a caldera –polar opposite settings. Drilling deep at Hercules Dome would leave the intermediate-depth drill free for drilling coastal domes. My first interest is to drill the other inter-ice-stream ridges of the Siple Coast to understand the deglacial history of the Ross ice sheet. This fits into the IPICS 40ka array objective. The Siple Dome record presents enigmas of a ~6 degree temperature increase in a century and thinning stopping by the early Holocene. Explaining and corroborating these records will yield great insight into how rapidly the West Antarctic ice sheet can disintegrate. There is also the possibility of drilling many other coastal domes. Sulzberger Bay, to the East of Roosevelt Island, has a plethora of domes and continuing farther East there are many locations up the Antarctic Peninsula. Drilling these sites would provide detailed records of climate variability for the past 2000 years, another IPICS objectives and may also yield LGM records in the deep ice.

Appendix A: *Metadata for the WDC06A-7 Timescale*

Timescale WDC06A-7 is described in WAIS Divide Project Members, 2013, "Onset of deglacial warming in West Antarctica driven by local orbital forcing", Nature

Types of Data used in the timescale
- 0-579 m: continuous chemistry with electrical measurements in areas of uncertainty. Depth interval 570-2800 m is based on variety of electrical measurements:
- 579-1350 m: dielectric profiling (DEP) measurements made in the field
- 1350-1940 m: Alternating Current Electrical Conductivity Measurement (AC-ECM) made at the National Ice Core Lab (NICL)
-1940-2020 m: Combination of AC- and DC-ECM and continuous chemistry, primarily black carbon, sulfur, and sodium.
- 2020-2800 m: AC-ECM and Direct Current (DC) ECM made at NICL (started at section 1955)
- 2910-3330 m: $d^{18}O$(ice) from field shavings.

Notes on Timescale from 0-579 m:
The depth-age scale for the upper 579 m of the WDC06A ice core is based on a broad range of continuous, high-depth-resolution elemental and chemical measurements with additional high-resolution (e.g., electrical properties) measurements used only when the chemical measurements were missing or ambiguous. An independent timescale using AC-ECM was in agreement within 1% of the timescale determined with the chemistry measurements and we use 1% for the estimated uncertainty. Annual picks mark summer peaks (nominally January 1). See Sigl et al., 2013, "A new bi[polar ice core record of volcanism from WAIS Divide and NEEM and implications for climate forcing of the last 2000 years," JGR for details.

Notes on the Timescale from 579-2800m
Estimated Uncertainty:
We provide qualitative estimates of the uncertainty in the annual layer interpretation for the following intervals based on the subjective quality of the annual signal. The interpretation uses insights from a comparison of 80 m of ECM and continuous chemistry data from 1940 to 2020 m. Increase in dust during has a tendency to split peaks and add non-annual variations, so the interpretation favors counting two small peaks as 1 year rather than as 2 years.

1) 0 to 580 m (present to 2.3 ka)
   - interpretation from continuous chemistry with 1% estimated uncertainty (McConnell and others)
1) 580 to 1960 m (2.3 to 11.6 ka): ± 2%
   - comparison with brittle ice chemistry show difference of 1%, so a 2% total uncertainty is assumed (Cole-Dai and Ferris)
2) 1960 to 2300 m (11.6 to 15.5 ka): ± 4%
   - comparison with continuous-flow chemistry for 1940 to 2020 show difference of 2.4%, so a 4% total uncertainty is assumed
3) 2300 to 2500 m (15.5 to 20 ka): ± 8%, except for depths in 4
   - annual signal in these depths is difficult to discern with apparent non-annual decreases due to dust. Uncertainty from previous period is doubled
4) 2421.75 to 2427.25 m (Old Faithful Volcanic Peak): ± 10%

- layers are interpolated using 5-m average annual layer thickness from above and below section
5) 2500 to 2800 m (20 to 30 ka): ± 4%
        - layers are much more regular than during the transition. Uncertainty is estimated to be the
        same as in interval 2.

Multi-track DC-ECM processing
The DC-ECM data is an average of multiple tracks along the same core but at different horizontal
positions across the core. The 7 tracks were averaged after the high and low value at each
measurement position was excluded. For 2750-2800, there was concern that the greater layer dips
would adversely influence the stacking. To correct for the lay dips the tracks were first aligned by
calculating the layer inclination from the correlation of the two outside tracks and shifting each track up
or down by the appropriate distance. Then the tracks were stacked in the same way as for 1955-2750.

Alignment of AC and DC data
The DC and AC data were often not properly aligned because the inclination of the layers resulted in mm
scale depth offsets. To align the DC-ECM and AC-ECM, the AC depths were shifted to the position of
maximum correlation with the DC data.

Interpretation of Annual Layers
Annual layers were initially identified with an automatic layer picker (McGwire et al., 2011) in both up-
and down- core directions. Above 1955 m, only the DEP or AC-ECM data was used; where the picks from
both directions agreed with 20% of the average annual layer thickness, the pick was accepted. Below
1955 m, both the AC and DC ECM data was used; where three of the four picks agreed within 20% of the
average annual layer thickness, the pick was accepted. For all depths below 579m, all picks where
reviewed manually by T.J. Fudge. Ken Taylor has reviewed the depth interval 579-900 and the top 5
meters of every 50 m section below 2000 m, with interpretation differences of ~0.5%. This timescale is
only based on T.J. Fudge's interpretation. Annual picks are at peaks in electrical conductivity thought to
correspond to summer. For 1940 to 2020, the ECM and continuous chemistry records were picked by
both Michael Sigl and T.J. Fudge, and a consensus timescale was agreed upon by them.

Data Adjustments
Different normalization techniques were used for different segments of the data:
The DEP data for depths 570-1350 m are available as normalized and un-normalized. The normalized
data was obtained by subtracting the mean value of each meter and then dividing by the average of the
absolute value of the difference. This corrected for meter-to meter differences in ice temperature when
it was measured, and electrode contact issues. This method has the disadvantage of reducing the
amplitude of annual layers near volcanic peaks.

The AC-ECM data for depths 1350-1950 m were not adjusted.

The AC- and DC-ECM for depths 1950-2800 m were normalized and adjusted. Unnormalized values are
also available.
    Normalization: The data were normalized by subtracted the mean conductivity of the section, then
    dividing by 3 times the standard deviation. The mean and standard deviations were calculated from
    a subset of the data to prevent volcanic signals from obscuring the annual signal after the data was
    normalized. The data 9 cm to either side of the peak value and the lowest 5% were excluded from
    the mean and standard deviation calculations. This exclusion was done to reduce the effect of
    volcanic peaks or dust lows on the amplitude of the annual signal.

Adjustment: The normalized data were then fitted with a cubic smoothing spline (Matlab script CFSMTHSPL.m which is based on CSAPS.m). The purpose of the smoothing spline was to correct lower values that commonly occurred at the ends of cores because of the position of the core tray on the ECM tracks. Only splines with a stiff spline parameter (typically 0.5) were applied. The spline curved never had more than two inflections points, so the wavelengths of the spline were much longer the annual layer signal in the data.

Determing the end of the Annual Layer Interpretation
It is difficult to determine where to stop interpreting annual layers. By ~3100 meters, the annual signal was gone. *Note that this does not mean decadal or longer timescale stratigraphy has been disturbed* We have stopped interpreting layers at 2800 m even though an annual layer signal appears to be present in much of the interval from 2800-3100 m because we are not sure that all annual layers are still being preserved.

The annual layer interpretation was stopped at 2800 m for three primary reasons:
1) The autopicking algorithm could no longer find a dominant annual layer thickness with the Fast Fourier Transform (FFT) tracing technique used above.
2) Sections of data looked like the layering had been "smeared". Inspection of the multi-track EC-ECM images also suggests irregular layering in locations.
3) The annual layer thicknesses inferred from an isotope match between the Byrd and WAIS Divide ice cores suggest more annual layers than were found in manual picks of selected intervals.

We are currently working on techniques for confidently identifying annual layers in the 2800-3100 m interval and it may be possible to extend the annual layer count by approximately 10,000 years.

Contributors to this timescale:
T.J. Fudge, Kendrick Taylor, Ken McGwire, Joe McConnell, Michael Sigl, Ross Edwards, Howard Conway, Edwin Waddington, James White, Bruce Vaughn, Jeff Severinghaus, and Todd Sowers